HZDR-045

ANALYSIS AND SIMULATION OF PHOTON SCATTERING AND NEUTRON CAPTURE GAMMA SPECTRA

Georg Alexander Schramm

Wissenschaftlich-Technische Berichte
HZDR-045 · ISSN 2191-8708

WISSENSCHAFTLICH-
TECHNISCHE BERICHTE

HZDR
HELMHOLTZ
ZENTRUM DRESDEN
ROSSENDORF

Wissenschaftlich-Technische Berichte
HZDR-045

Georg Alexander Schramm

ANALYSIS AND SIMULATION OF PHOTON SCATTERING AND NEUTRON CAPTURE GAMMA SPECTRA

HZDR

HELMHOLTZ
ZENTRUM DRESDEN
ROSSENDORF

Druckausgabe: ISSN 2191-8708

Elektronische Ausgabe: ISSN 2191-8716

Die elektronische Ausgabe erscheint unter Creative Commons License (CC BY-NC-ND):

Qucosa: http://fzd.qucosa.de/startseite/

Die vorliegende Arbeit wurde als Diplomarbeit am Institut für Kern- und Teilchenphysik der Technischen Universität Dresden sowie als Wissenschaftlich-Technischer Bericht des Helmholtz-Zentrum Dresden-Rossendorf mit der Berichtsnummer **HZDR-045** veröffentlicht.

2014

Herausgegeben vom

Helmholtz-Zentrum Dresden - Rossendorf

Bautzner Landstr. 400

01328 Dresden

Germany

Analysis and Simulation of Photon Scattering and Neutron Capture Gamma Spectra

Diplomarbeit zur Erlangung des akademischen Grades
Diplom-Physiker

vorgelegt von

Georg Alexander Schramm

geboren am 08.04.1987 in Görlitz

Institut für Kern- und Teilchenphysik
Fachrichtung Physik
Fakultät Mathematik und Naturwissenschaften
der Technischen Universität Dresden
2011

1. Gutachter: Prof. Dr. Thomas Cowan

2. Gutachter: Prof. Dr. Kai Zuber

Datum des Einreichens der Arbeit: 31.03.2011

Kurzfassung

Im Rahmen dieser Arbeit wurden zwei Zwillingsexperimente, bestehend aus Neutroneneinfang und Photonenstreuung an den Nachbarisotopen ^{77}Se / ^{78}Se und ^{195}Pt / ^{196}Pt, analysiert, um qualitative und quantitative Informationen über die Photonenstärkefunktion und Niveaudichte in den jeweiligen Compoundkernen zu gewinnen. Für die Analyse und Simulation der beiden Experimenttypen wurde eine neue Monte Carlo Simulation entwickelt, die einen effizienten und schnellen, extrem statistischen Ansatz zur Beschreibung von Kernabregungen unter der Aussendung von Gammastrahlung verwendet. Darüberhinaus wurde der Einfluss von Fluktuationen in Übergangsbreiten der Photonenstreuung untersucht und quantifiziert. Es konnte gezeigt werden, dass diese eine Erhöhung von elastischen Streuprozessen zur Folge haben. Die Datenanalyse beider Zwillingsexperimente zeigt nicht-lorentzförmige extra $E1$ Photonenstärke unterhalb der Neutronenseparationsenergie.

Abstract

Within this thesis two twin experiments consisting of neutron capture and photon scattering on the neighbour isotopes ^{77}Se / ^{78}Se and ^{195}Pt / ^{196}Pt have been analysed to gain qualitative and quantitative information about the photon strength function and level density in the respective compound nuclei. For the analysis and simulation of both experimental types a new Monte Carlo simulation using a fast and efficient, extreme statistical treatment of radiative nuclear deexcitations, was developed. Furthermore the influence of fluctuations of transition widths on photon scattering were investigated and quantified. It could be shown that those lead to an enhancement of elastic scattering processes. The data analysis of both twin experiments reveals non-Lorentzian extra E1 photon strength below the neutron separation energy.

cartoon from: http://www.random.org/analysis/dilbert.jpg, 19th February 2011

Contents

1 Motivation and Introduction **7**

2 Theoretical Background **9**
2.1 Neutron Capture Gamma Spectra 9
2.2 Photon Scattering 14
2.3 Gamma Ray Transitions in Nuclei 18
2.4 Nuclear Level Densities 19
2.4.1 The Total Level Density 20
2.4.2 The Spin Distribution of States 22
2.5 Photon Strength Functions 24
2.5.1 E1 Strength Functions 25
2.5.2 M1 Strength Functions 27
2.6 The Statistical Fluctuation Factor 28

3 Experimental Setups **33**
3.1 The Neutron Capture Setup 33
3.2 The Photon Scattering Facility 35

4 Data Analysis **37**
4.1 Simulation of Nuclear Radiative Deexcitations 37
4.2 Analysis of Neutron Capture Experiments 42
4.2.1 Analysis of Neutron Capture on Selenium-77 42
4.2.2 Analysis of Neutron Capture on Platinum-195 49
4.3 Analysis of Photon Scattering Experiments 54
4.3.1 Analysis of Photon Scattering from Selenium-78 54
4.3.2 Analysis of Photon Scattering from Platinum-196 65

5 Results, Discussion and Outlook **71**
5.1 Selenium 71
5.2 Platinum 72
5.3 Discussion and Outlook 74

A Figures and Tables **I**

List of Figures **IX**

List of Tables **XI**

Bibliography **XVII**

Chapter 1
Motivation and Introduction

One of the challenges of mankind is the generation of electrical energy. About 15% of the total energy and one third of the electrical energy consumed in the European Union comes from nuclear power plants [EU, 2007] which have the advantage of a very low emittance of green house gases. For several EU states the use of nuclear power is one of the ways to lower their emittance of CO_2 and to reach their climate goals. However, nuclear energy has the disadvantage of producing radioactive waste. Regardless of whether the use of nuclear energy will be increased or be stopped in a few years, the nuclear waste which has been already produced has to be handled. Without any reprocessing, some parts of the waste have to be stored safely for a very long time ($\approx 10^5$ years) which would be a burden and hard task for many future generations. The challenge for the sustainable use of nuclear energy has to be the reduction in the amount of nuclear waste that will be left for final storage and simultaneously the reduction of the final storage time.
A possible solution for this challenge is the transmutation of radioactive waste which is the conversion of long-lived isotopes into shorter-lived ones via nuclear reactions. For example, the long-lived actinides ^{239}Pu and ^{242}Pu produced via unwanted successive neutron capture on ^{238}U in a commercial pressurised-water power reactor, can be fissioned into shorter-lived fission products using fast neutrons. The partitioning and fission of plutonium, the chemical element which contributes the biggest part of the radiotoxicity of nuclear waste after 100 years, could reduce the final storage time by a factor of ten to approximately 10^4 years.
The MYRRHA project [Abderrahim et al., 2001] aims at building the first subcritical accelerator driven system (ADS) that will be used for transmutation. For an efficient transmutation process, facilities like MYRRHA have to be simulated in advance. For these complicated calculations nuclear data such as cross sections for fission, neutron scattering and capture or photonuclear reactions are needed for many isotopes. On the one hand, these quantities can be measured directly for stable or long-lived isotopes. On the other hand, it is impossible to measure them for short-lived ones raising the need of theoretical models for calculations of these quantities.
Two of these quantities that are of special interest are the photon strength function and the nuclear level density which directly enter in statistical model calculations, e.g. for neutron capture. This thesis deals with the analysis and comparison of two twin experiments, consisting of neutron capture and photon scattering, for measuring the photon strength function up to the neutron separation energy. The neutron capture experiments were performed on the isotopes ^{77}Se and ^{195}Pt in October 2009

at the 10 MW_{th} research reactor of the Hungarian Academy of Sciences in Budapest. Complementary, the second part of the twin experiments, photon scattering experiments on ^{78}Se and ^{196}Pt, took place at Helmholtz-Zentrum Dresden-Rossendorf in 2009 and 2010. The isotope pairs of selenium and platinum have been chosen to assure that s-wave neutron capture and photon scattering from the neighbour isotope lead to excited compound nuclei with equal spin and parity. The analysis and comparison of the gamma ray spectra resulting from deexcitations of excited states in the compound nuclei in both cases reveals qualitative and quantitative information about the photon strength function and the level density which can be compared to predictions of different models. By combining two different nuclear reactions systematic uncertainties in both types of measurements will be examined and the influence on the deduced photon strength function and nuclear level density can be estimated. For the analysis of both experiments, a new Monte Carlo simulation code using a fast and efficient statistical treatment for radiative deexcitations of nuclei was developed. The experiments in this thesis were supported by the EURATOM FP 6 project EFNUDAT and the BMBF project TRAKULA 02NUK13A.

Chapter 2
Theoretical Background

This chapter provides an overview about all quantities needed for a theoretical description of the measured neutron capture and photon scattering gamma ray spectra. At first, in sections (2.1) and (2.2), the origin and a statistical calculation method of the measured spectra are presented. Subsequently, in sections (2.4) and (2.5), the two most important quantities for a statistical description of both spectra, the nuclear level density and photon strength function, are discussed. Section (2.6) is a brief introduction into the influence of fluctuations in transitions widths on photon scattering.

2.1 Neutron Capture Gamma Spectra

The first part of the performed twin experiments deals with the analysis of cold neutron capture gamma ray spectra. This process can be described in two steps and is schematically illustrated in figures (2.1) and (2.2).
In the first step a neutron is captured by a target nucleus (A,Z) leading to an excited compound nucleus $(A+1,Z)$. The excitation energy is equal to the incident kinetic energy of the neutron T_n plus the neutron separation energy S_n and minus the recoil energy E_R of the compound nucleus. Since cold neutrons with a kinetic energy of around 1 meV and heavy target nuclei were used, T_n and E_R are negligible. Possible spins J of the excited compound nucleus after s-wave neutron capture are $\left|J_\mathrm{T} - \frac{1}{2}\right|$ and $J_\mathrm{T} + \frac{1}{2}$ where J_T is the ground state spin of the target nucleus. The parity Π of the compound nucleus after s-wave neutron capture is given by $\Pi_\mathrm{n} \cdot \Pi_\mathrm{T}$, where Π_n is the parity of the neutron $(+1)$ and Π_T is the ground state parity of the target nucleus. Since both measured target nuclei (^{77}Se and ^{195}Pt) have $\frac{1}{2}^-$ ground states, 0^- and 1^- resonances can be excited. Due to the small incident neutron energy, only the first state above the neutron threshold in the compound nucleus, which is

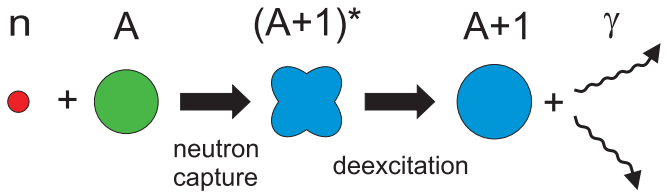

Figure 2.1: Scheme of neutron capture as a two step process. First an excited compound nucleus is created. Subsequently it deexcites via the emission of gamma rays.

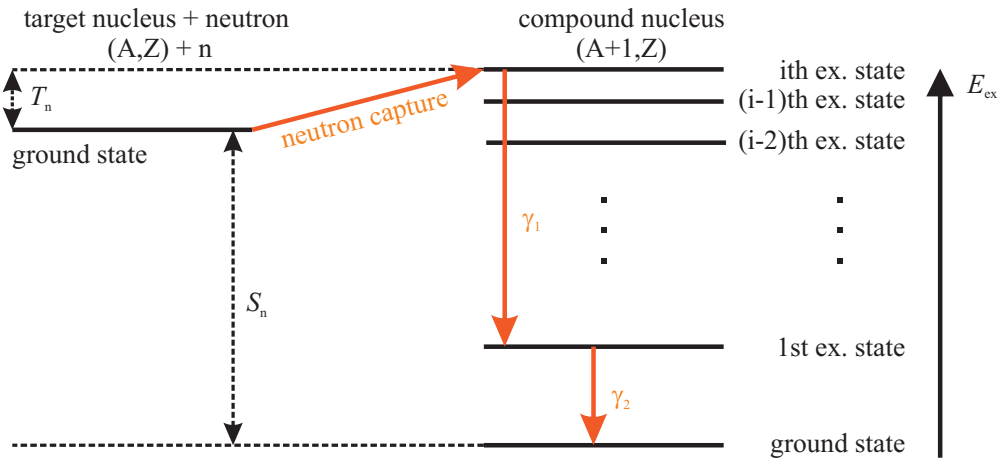

Figure 2.2: Energy scheme of neutron capture. An excited compound nucleus $(A+1, Z)$ is created after neutron capture on a target nucleus (A, Z). Neglecting the recoil energy, the excitation energy is the sum of the neutron kinetic energy T_n and the neutron separation energy of the compound nucleus. Subsequently to the excitation, the compound nucleus deexcites back to the ground state via the emission of gamma rays. In this figure, only a few excited states are shown, e.g. for ^{78}Se the number of excited states up to the neutron separation energy S_n is more than 100000.

according to [Mughabghab, 2006] a 1^- state, is excited.
Subsequently in the second step, the excited 1^- state of the compound nucleus deexcites via emission of gamma radiation back to the ground state. In most cases, the deexcitation does not go directly to the ground state. Instead it happens via the population of intermediate states leading to the emission of several gamma rays. An energy spectrum of these emitted gamma quanta for the reaction ^{77}Se(n,γ) is shown in figure (2.3). In this spectrum many peaks up to the neutron separation energy of ^{78}Se ($S_n = 10498\,\text{keV}$) are visible. For further understanding of the spectral shape it is reasonable to divide the spectrum into three parts.

1. Low-energy region ($0 \ldots \approx 2300\,\text{keV}$): The spectrum in this region is dominated by strong gamma peaks resulting from transitions between the first low lying excited states in the compound nucleus. These states are populated during cascade deexcitations of the initially excited state.

2. Intermediate (continuum) region ($3000\,\text{keV} \ldots \approx 7500\,\text{keV}$): Gamma peaks in this region are mainly primary, secondary and third order transitions during a cascade deexcitation.

3. High-energy region ($7500\,\text{keV} \ldots \approx 10500\,\text{keV}$): Gamma peaks in this region are primary gamma transitions of the initially excited state in the compound nucleus to the first low lying excited states.

In addition to the strong peaks, a continuum containing many weak transitions is visible in the measured spectrum. Due to the finite energy resolution of the detector, natural and induced nuclear background and and low statistics, these weak

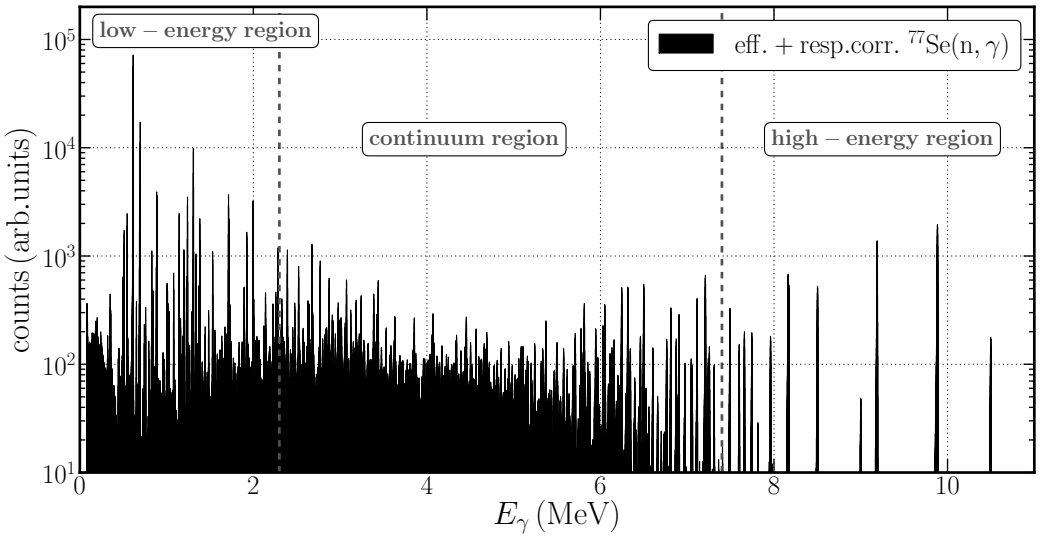

Figure 2.3: Measured ^{77}Se(n,γ) spectrum corrected for detector response and efficiency. The neutron separation energy of ^{78}Se is 10498 keV [Farhan and Singh, 2009].

transitions are not resolvable. In order to theoretically describe capture gamma ray spectra, one would have to know all excited states of the compound nucleus and all transition widths between these states. Due to the complexity of the nuclear many body system, this is impossible at the moment. Only few excited states and transition widths all lying in the low-energy region are known in intermediate and heavy nuclei from nuclear spectroscopy. Hence a statistical treatment for the analysis of neutron capture gamma ray spectra must be used. Instead of trying to calculate the real transition width Γ_{if} between an initial state i at energy E_i and a final one f at energy E_f, it is reasonable to express this quantity by an average transition widths $\langle\Gamma_{if}\rangle$ which can be calculated via [Bartholomew et al., 1973]:

$$\langle\Gamma_{if}\rangle = \frac{f_{XL}(E_\gamma)\cdot E_\gamma^{2L+1}}{\varrho(E_i)} \tag{2.1}$$

Where $E_\gamma \approx E_i - E_f$ is the transition energy, $f_{XL}(E_\gamma)$ is the photon strength function for a transition of multipolarity XL discussed in section (2.5) and $\varrho(E_i)$ is the level density in the compound nucleus at the initial energy discussed in section (2.4). The averaging in equation (2.1) is done over several final states in an energy interval around E_f. The transition width Γ_{if} between distinct states can be expressed by the average value value via:

$$\Gamma_{if} = y_{if}\cdot\langle\Gamma_{if}\rangle \tag{2.2}$$

Where y_{if} is a statistical distribution factor which describes the fluctuations of the transition widths Γ_{if}. According to [Porter and Thomas, 1956] and the predictions of Random Matrix Theory [Guhr et al., 1998] which is based on the assumption of a Gaussian distribution of the transition amplitudes, y_{if} follows the Porter-Thomas distribution which is a reduced chi-square distribution with one degree of freedom. The probability density function of this distribution with mean unity is given by:

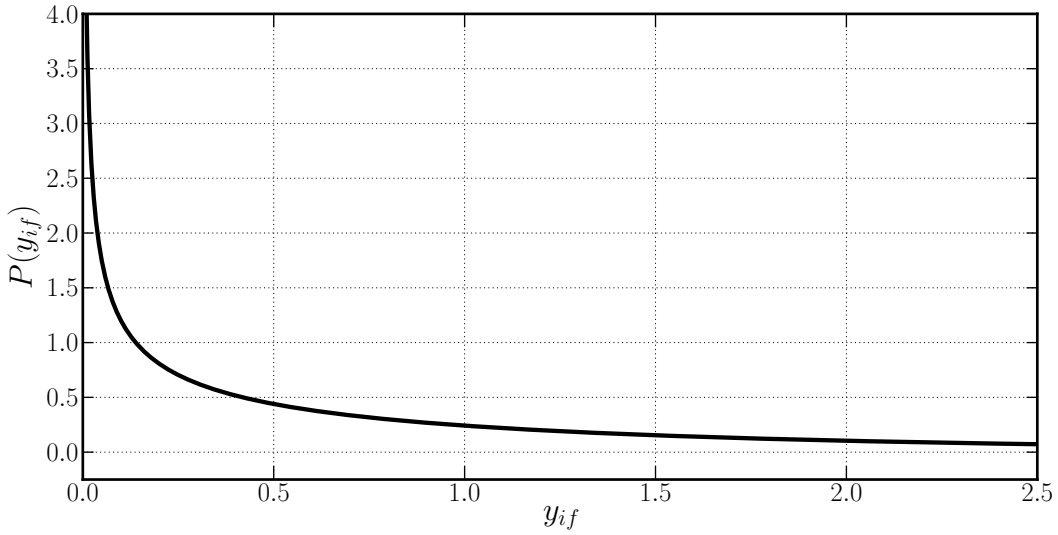

Figure 2.4: Probability density function of the Porter-Thomas distribution which is equal to a chi-square distribution with one degree freedom.

$$P(y_{if})dy_{if} = \frac{\mathrm{e}^{-y_{if}/2}}{\sqrt{2\pi y_{if}}}\, dy_{if} \tag{2.3}$$

and shown in figure (2.4). This very asymmetrical distribution leads to strong fluctuations of the transition widths.
However, the value of y_{if} for a single distinct transition is unknown which makes it impossible to predict the widths of single distinct transitions. Instead, it is reasonable to analyse a rebinned capture gamma ray spectrum with a bigger bin width in a statistical sense. Choosing the bin width big enough, it can be assured that the yield in one bin results from transitions to several different final states. The yield Y_{bin} for transitions starting at one distinct state (for example the state excited after neutron capture) and ending in an energy bin $\left[E_f - \frac{\Delta}{2}, E_f + \frac{\Delta}{2}\right]$ is proportional to the sum of all transition widths ending at final states in that bin divided by the total radiative width of the initial state $\Gamma_{i,\mathrm{tot}}$:

$$Y_{\mathrm{bin}} \propto \sum_{f',E_{f'}\in\mathrm{bin}} \frac{\Gamma_{if'}}{\Gamma_{i,\mathrm{tot}}} = \sum_{f',E_{f'}\in\mathrm{bin}} \frac{y_{if'}\,\langle\Gamma_{if'}\rangle}{\Gamma_{i,\mathrm{tot}}} \tag{2.4}$$

If on the one hand the energy bin is big enough to assure that there are many possible final states in the bin and on the other hand small enough that the level density, the photon strength function and the transition energy do not vary too much over the bin, it is justified to write [Bartholomew et al., 1973]:

$$Y_{\mathrm{bin}} \propto \frac{\langle\Gamma_{if}\rangle}{\Gamma_{i,\mathrm{tot}}} \sum_{f',E_{f'}\in\mathrm{bin}} y_{if'} \approx N_f \cdot \frac{\langle\Gamma_{if}\rangle}{\Gamma_{i,\mathrm{tot}}} \approx \varrho(E_f)\cdot\Delta E \cdot \frac{f_{XL}(E_\gamma)\cdot E_\gamma^{2L+1}}{\Gamma_{i,\mathrm{tot}}\cdot\varrho(E_i)} \tag{2.5}$$

The sum over the Porter-Thomas distributed $y_{if'}$ in equation (2.5) can be replaced by the number of final states in the bin N_f times the mean of the distribution

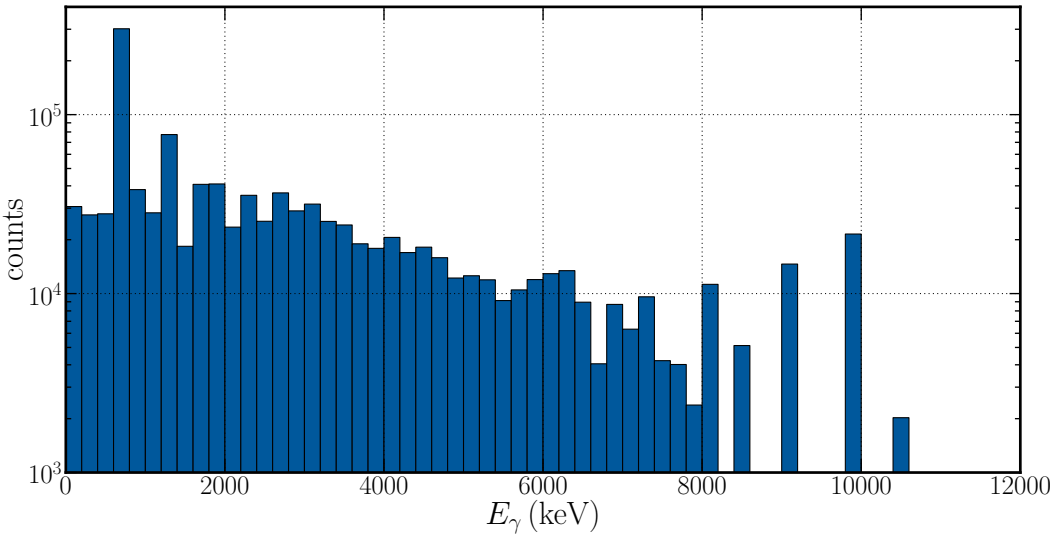

Figure 2.5: Rebinned experimental capture gamma ray spectrum (binwidth 200 keV) of the reaction ^{77}Se(n,γ)

which is one. It has to be pointed out again, that this step is only justified if there are enough reachable final states in the energy bin. Regarding equation (2.5) and noticing that $\varrho(E_i)$ and $\Gamma_{i,\mathrm{tot}}$ are constants for a fixed initial state, it is obvious that two quantities influence the yield of measured gamma rays following neutron capture:

1. The level density of the final states $\varrho(E_f)$

2. The photon strength function $f_{XL}(E_\gamma)$

Figure (2.5) shows a rebinned capture gamma spectrum of the reaction ^{77}Se(n,γ). It is important to check which bins of the rebinned spectrum fulfill the conditions for the validity of equation (2.5). The bins in the low-energy region (up to 2300 keV) do not. They are dominated by transitions between distinct low lying excited states. For example, the bin $600 - 800$ keV is dominated by the 613 keV transition from the first excited state to the ground state. Neither do the energy bins in the high-energy region (above 7500 keV). Their content results from transitions with strongly fluctuating transition widths to distinct low lying states. However the bins in the intermediate region (2300 keV ... 7500 keV) do fulfill the requirements. The gamma yield in each bin in this continuum region can result from many different transitions which assures that fluctuations are averaged out.
Hence it is reasonable to try to understand the influence of the photon strength function and the level density on the shape of continuum region of the capture gamma ray spectrum using equation (2.5). For this purpose a simulation describing radiative cascade deexcitations of excited nuclei has been developed which is discussed in detail in section (4.1).

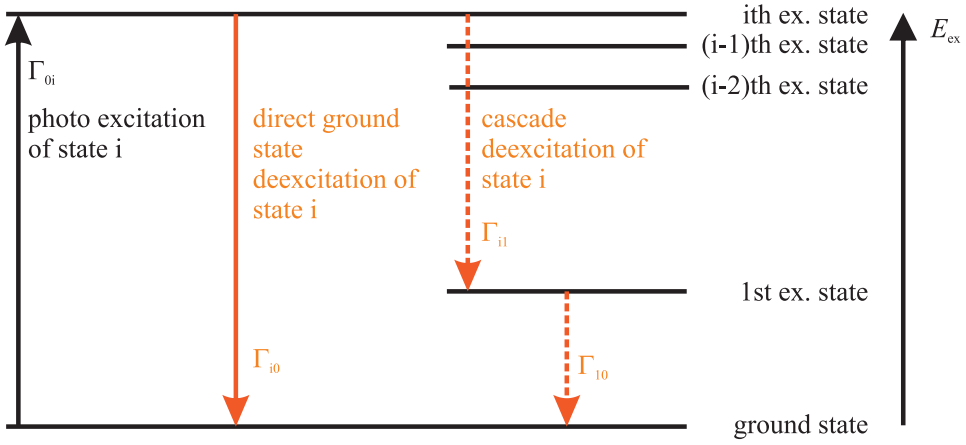

Figure 2.6: Scheme of photon scattering. A state i is excited via the absorption of a real photon. Subsequently the excited state deexcites directly or in a cascade back to the ground state via the emission of gamma rays.

2.2 Photon Scattering

The second part of the performed twin experiments is the determination of the average photon absorption cross section and the related photon strength function from photon scattering experiments. Similar to neutron capture, this process can be visualized in two steps - excitation and deexcitation. In contrast to neutron capture, in photon scattering the nucleus is excited via absorption of a real photon. Electric dipole excitations from ground states of even-even nuclei, like ^{78}Se and ^{196}Pt, lead to excited 1^- states. Thus, spin and parity of the initially excited state in the compound nucleus are equal to the ones in the neutron capture experiments on ^{77}Se and ^{195}Pt. Subsequently to the excitation, the nucleus deexcites back to the ground state, either directly (elastic scattering) or via a cascade (inelastic scattering) leading to the emission of one or several gamma rays. A scheme of photon scattering is shown in figure (2.6). In contrast to neutron capture not only one state is excited. Due to the use of bremsstrahlung for the photoexcitation, preferentially 1^- states between the ground state and the endpoint energy of the bremsstrahlung spectrum can be excited. In addition, magnetic dipole excitations that leas to excited 1^+ are possible, as well. However, as discussed in section (2.5.2), the strength of these excitations is much weaker compared to the electric ones.

At high excitation energies ($E_{ex} \approx S_n$) the mean spacing of 1^- states ($\approx 100\,\text{eV}$) is very small compared to the resolution of the used high purity germanium (HPGe) detectors ($\approx 10\,\text{keV}$). That means, it is not possible to resolve gamma transitions of all high lying states. Moreover, due to the mentioned fluctuations of the transition widths, many unresolvable weak transitions are measured, which create a continuum region in the measured deexcitation spectrum. A raw experimental spectrum from the ^{78}Se(γ,γ) experiment is shown in figure (2.7). Many peaks are visible that result from strong transitions in the deexcitation process. It is not clear whether these are direct ground state or cascade transitions. Furthermore the spectrum contains a continuum region of unresolved weak transitions. The strong peaks at 4443 keV,

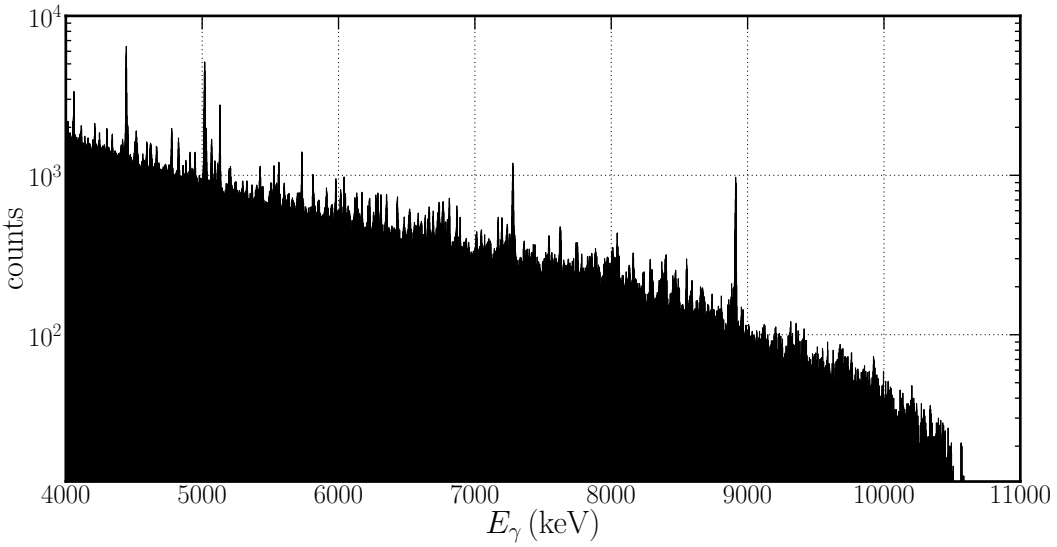

Figure 2.7: Uncorrected measured ^{78}Se(γ,γ) spectrum. Many peaks from strong transition in the deexcitation process are visible. Furthermore the spectrum contains a continuum region of unresolved weak transition. The strong peaks at 4443 keV, 5017 keV, 7279 keV and 8912 keV are transitions of ^{11}B used for the bremsstrahlung fluence determination.

5017 keV, 7279 keV and 8912 keV are transitions of ^{11}B combined with the target and used for the bremsstrahlung fluence determination.

In order to understand the measured spectrum, one has to start with a description of the photoabsorption process into single states and their subsequent deexcitation. The cross section for photoabsorption from the ground state with spin I_0 into a single resonance i with spin I_i is given by [Axel, 1968]:

$$\sigma_{\mathrm{abs},i}(E) = 4\, g'(I_i)\pi \left(\frac{\hbar c}{E}\right)^2 \frac{\Gamma_{\gamma,0i}\Gamma_{i,\mathrm{tot}}}{(E-E_i)^2 + \frac{1}{4}\Gamma_{i,\mathrm{tot}}^2} \tag{2.6}$$

Here, $\Gamma_{\gamma,0i}$ is the partial width for a radiative transition between the i-th excited state and the ground state, $\Gamma_{i,\mathrm{tot}}$ is the total width of the i-th state - E_i is the excitation energy of i and $g'(I_i) = (2I_i+1)/[2\cdot(2I_0+1)]$ is a spin statistical factor including the possible orientations of the z-component of the spins of the nuclear states and the photon.
Integrating over all energies and assuming that $\Gamma_i \ll E_i$ yields:

$$\int_0^\infty \sigma_{\mathrm{abs},i}(E)dE = \left(\frac{\pi\hbar c}{E}\right)^2 2\, g'(I_i)\Gamma_{\gamma,0i} \tag{2.7}$$

Averaging $\sigma_{\mathrm{abs},i}$ over all resonances with spin I_i in an interval $\left[E-\frac{\Delta E}{2}, E+\frac{\Delta E}{2}\right]$ leads to:

$$\langle\sigma_{\mathrm{abs}}(E)\rangle_{I_i} = \frac{1}{\Delta E}\sum_{E_i\in\mathrm{interval}}\int_0^\infty \sigma_{\mathrm{abs},i}(E)dE = \left(\frac{\pi\hbar c}{E}\right)^2 2\,g'(I_i)\,\langle\Gamma_{\gamma,0i}\rangle\,\varrho(E,I_i) \quad (2.8)$$

Here, $\varrho(E,I_i)$ is the density of spin I_i states in the averaging interval. It has to be emphasised that $\langle\sigma_{\mathrm{abs}}(E)\rangle_{I_i}$ is the average cross section for photoabsorption in states with a fixed spin I_i. Considering dipole excitations, absorption into states with spins $I = |I_0 - 1|, \ldots, I_0 + 1$ is in general possible. [Brink, 1955] has shown, that the average dipole absorption cross section $\langle\sigma_{\mathrm{abs}}(E)\rangle$ into states with all possible spins is related to the absorption cross section into states with a fixed spin by:

$$\langle\sigma_{\mathrm{abs}}(E)\rangle = \frac{3}{2\,g'(I_i)}\,\langle\sigma_{\mathrm{abs}}(E)\rangle_{I_i} = 3\left(\frac{\pi\hbar c}{E}\right)^2\langle\Gamma_{\gamma,0i}\rangle\,\varrho(E) \quad (2.9)$$

By replacing $\langle\Gamma_{\gamma,0i}\rangle$ with equation (2.1), one obtains the relation between the averaged dipole absorption cross section and the dipole strength function:

$$\langle\sigma_{\mathrm{abs}}(E)\rangle = 3(\pi\hbar c)^2\,E\,f_1(E) \quad (2.10)$$

Considering a typical photon scattering experiment where a suitably thin target with negligible photon attenuation with an areal density $\frac{dN_{\mathrm{T}}}{dA}(x,y)$ (number of target atoms per unit area perpendicular to the beam at the position (x,y)) is irradiated with a spectral bremsstrahlung fluence $\frac{d^2N_\gamma}{dA\,dE}(x,y,E)$ (number of photons per unit energy and unit area at the position (x,y) with energy E), the number of absorbed photons $Y_{\mathrm{abs}}(E,\Delta E)$ in an energy bin ΔE around E is given by:

$$Y_{\mathrm{abs}}(E,\Delta E) = \int_{E-\frac{\Delta E}{2}}^{E+\frac{\Delta E}{2}}\langle\sigma_{\mathrm{abs}}(E')\rangle\int_{\mathrm{tar.}}\frac{dN_{\mathrm{T}}}{dA}(x,y)\cdot\frac{d^2N_\gamma}{dA\,dE'}(x,y,E')\,dA\,dE' \quad (2.11)$$

If the photon beam is bigger than the target and constant across the target area, one obtains:

$$Y_{\mathrm{abs}}(E,\Delta E) = \int_{E-\frac{\Delta E}{2}}^{E+\frac{\Delta E}{2}}\langle\sigma_{\mathrm{abs}}(E')\rangle\,\frac{d^2N_\gamma}{dA\,dE'}(E')\int_{\mathrm{tar.}}\frac{dN_{\mathrm{T}}}{dA}(x,y)\,dA\,dE' \quad (2.12)$$

$$Y_{\mathrm{abs}}(E,\Delta E) = N_{\mathrm{T}}\int_{E-\frac{\Delta E}{2}}^{E+\frac{\Delta E}{2}}\langle\sigma_{\mathrm{abs}}(E')\rangle\,\frac{d^2N_\gamma}{dA\,dE'}(E')\,dE' \quad (2.13)$$

Assuming that the energy bin is small and that the spectral fluence $\Phi_E \equiv \frac{d^2N_\gamma}{dA\,dE}$ and $\langle\sigma_{\mathrm{abs}}(E)\rangle$ are constant over the bin, one obtains:

$$Y_{\mathrm{abs}}(E,\Delta E) = N_{\mathrm{T}}\cdot\Phi_E(E)\cdot\langle\sigma_{\mathrm{abs}}(E)\rangle\cdot\Delta E \quad (2.14)$$

In principle one could obtain the average photoabsorption cross section by measuring the number of absorbed photons per energy bin. However, due to the dominant atomic reactions and the relatively weakness of nuclear interactions, this is difficult in an experiment. Instead the technique of photon scattering is used [Kneissl et al., 1996]. In this experimental method the number of photons emitted in the deexcitation process following photoexcitation is measured. Of special interest is the process of elastic photon scattering which is a two step process consisting of photoabsorption into an excited state i and radiative deexcitation of this state back to the ground state. The cross section of this process is given by the cross section for photoabsorption from the ground state with spin I_0 into an excited state i with spin I_i times the ground state branching ratio $\Gamma_{\gamma,i0}/\Gamma_{i,\mathrm{tot}}$ of i.

$$\sigma_{\mathrm{scat},i}(E) = \sigma_{\mathrm{abs},i}(E) \cdot \frac{\Gamma_{\gamma,0i}}{\Gamma_{i,\mathrm{tot}}} \tag{2.15}$$

Integrating over the energy and averaging over an energy bin and all possible spins yields:

$$\langle \sigma_{\mathrm{scat}}(E) \rangle = 3 \left(\frac{\pi \hbar c}{E} \right)^2 \left\langle \Gamma_{\gamma,0i} \frac{\Gamma_{\gamma,0i}}{\Gamma_{i,\mathrm{tot}}} \right\rangle \varrho(E) \tag{2.16}$$

In analogy to equation (2.14) the number of elastically scattered photons on resonances in an interval $\left[E - \frac{\Delta E}{2}, E + \frac{\Delta E}{2}\right]$ is given by:

$$Y_{\mathrm{scat}}(E, \Delta E) = N_A \cdot \Phi_E(E) \cdot \langle \sigma_{\mathrm{scat}}(E) \rangle \cdot \Delta E \tag{2.17}$$

In order to extract the averaged photoabsorption cross section $\langle \sigma_{\mathrm{abs}}(E) \rangle$ from a photon scattering experiment, it has to be expressed in terms of the average elastic scattering cross section $\langle \sigma_{\mathrm{scat}}(E) \rangle$ which can be measured in the experiment. This is only possible by transforming the average of the product of transition widths into a product of average transition widths. It has to be strongly emphasized that these two quantities are not equal. Formally it is reasonable to define [Bartholomew et al., 1973]:

$$\left\langle \Gamma_{\gamma,0i} \frac{\Gamma_{\gamma,i0}}{\Gamma_{i,\mathrm{tot}}} \right\rangle = S \cdot \frac{\langle \Gamma_{\gamma,0i} \rangle \langle \Gamma_{\gamma,0i} \rangle}{\langle \Gamma_{i,\mathrm{tot}} \rangle} \tag{2.18}$$

The factor S is called statistical fluctuation factor and is discussed in detail in section (2.6). With the help of equation (2.9), (2.16) and (2.18), it is possible to calculate the average absorption cross section from the average elastic scattering cross section.

$$\langle \sigma_{\mathrm{abs}}(E) \rangle = \langle \sigma_{\mathrm{scat}}(E) \rangle \Big/ \left(S \cdot \frac{\langle \Gamma_{\gamma,0i} \rangle}{\langle \Gamma_{i,\mathrm{tot}} \rangle} \right) = \frac{Y_{\mathrm{scat}}(E, \Delta E)}{N_{\mathrm{T}} \cdot \Phi_E(E) \cdot \Delta E} \Big/ \left(S \cdot \frac{\langle \Gamma_{\gamma,0i} \rangle}{\langle \Gamma_{i,\mathrm{tot}} \rangle} \right) \tag{2.19}$$

That means the statistical fluctuation factor S and the average ground state branching ratio $\frac{\langle \Gamma_{\gamma,0i} \rangle}{\langle \Gamma_{i,\mathrm{tot}} \rangle}$ have to be calculated in order to extract the average photoabsorption cross section from a photon scattering experiment.

The complete analysis of a photon scattering experiment is more complicated due to several reasons:

- The response function of the used gamma ray detector
- The existence of non-nuclear scattered photons (atomic background)
- The existence of inelastically scattered photons (deexcitation happens via a cascade instead directly to the ground state)

All these effects have to be corrected in the following steps:

1. Deconvolution of the measured spectrum for the detector response
2. Simulation and subtraction of non-nuclear scattered events
3. Simulation and subtraction of inelastically scattered events
4. Calculation of $\langle\sigma_{\mathrm{scat}}(E)\rangle$ from the number of elastically scattered events, $\Phi_E(E)$ and N_{T}
5. Simulation of the statistical fluctuation factor and the average branching ratio and calculation of $\langle\sigma_{\mathrm{abs}}(E)\rangle$ from $\langle\sigma_{\mathrm{scat}}(E)\rangle$

It has to mentioned, that the corrections for inelastically scattered events, the average branching ratio and the statistical fluctuation factor themselves depend on the level density and the strength function. In order to achieve self-consistent results an iterative analysis must be used.

2.3 Gamma Ray Transitions in Nuclei

For understanding measured gamma ray spectra in neutron capture (n,γ) and photon scattering experiments (γ,γ), it is crucial to describe the properties of radiative transitions in nuclei. If a state i with energy E_i, spin J_i and parity Π_i is excited, it will deexcite after some time to a lower lying state f at E_f with spin J_f and parity Π_f. Considering the conservation of energy and momentum one obtains:

$$E_i - E_f = E_\gamma \left(1 + \frac{E_\gamma}{2Mc^2}\right) \tag{2.20}$$

Here, M is the mass of the recoil atom and E_γ the energy of the emitted photon. Obviously, the energy difference between the states is not completely emitted as gamma ray energy. A small fraction is converted into recoil energy of the nucleus which leads to the second term in the parenthesis of equation (2.20). E.g., for a gamma transition energy of 8.92 MeV the recoil energy is approximately 3.6 keV for ^{11}B and 0.5 keV for ^{78}Se.
Since a gamma quantum is an electromagnetic wave, it can be further characterized by its angular momentum l and parity Π. Conventionally, a gamma transition is described by its multipole order L. Moreover, there are two different types of transitions: electric E and magnetic M ones. The parity of both types are given by:

	$E1$	$M1$	$E2$
multipole order L		1 (dipole)	2 (quadrupole)
transition parity Π	-1	$+1$	$+1$
spin of final state J_f	$\lvert J_i - 1\rvert \leq J_f \leq J_i + 1$		$\lvert J_i - 2\rvert \leq J_f \leq J_i + 2$
parity of final state Π_f	$-\Pi_i$	Π_i	Π_i
forbidden transitions		$0 \rightarrow 0$	$0 \rightarrow 0$, $0 \rightarrow 1$, $\frac{1}{2} \rightarrow \frac{1}{2}$

Table 2.1: Characteristics of radiative $E1$, $M1$ and $E2$ transitions from a state λ to a state i.

$$\Pi = \begin{cases} (-1)^L & \text{for electric transitions} \\ (-1)^{L+1} & \text{for magnetic transitions} \end{cases} \tag{2.21}$$

Usually a radiative transition is labeled with the two letters XL, where X stands for electric E or magnetic M transition and L is the multipole order. Together, XL is called multipolarity. Table (2.1) summarizes the most important characteristics of $E1$, $M1$ and $E2$ transitions.
It should be taken into account that an excited state can deexcite to any lower lying one, as long as the selection rules, given in table (2.1), are fulfilled. In general, the transition width decreases with increasing multipole order and electric transitions are stronger than magnetic ones.

2.4 Nuclear Level Densities

The nuclear level density ϱ is one of the most crucial elements for statistical calculations of nuclear properties and reactions. It plays an important role at intermediate and high excitation energies where information about discrete levels is not available or incomplete.
The level density depends on the excitation energy E, the spin J and the parity Π of states in nuclei. It is defined as the number of levels N with a certain spin and parity in an energy interval $I = \left[E - \frac{\Delta E}{2}, E - \frac{\Delta E}{2}\right]$ around E divided by ΔE.

$$\varrho\left(E, J, \Pi\right) = \frac{1}{\Delta E} \sum_{i, E_i \in I} N\left(E_i, J, \Pi\right) \tag{2.22}$$

The sum in equation (2.22) runs over all states i in the interval I. With ΔE approaching zero, the level density is given by:

$$\varrho\left(E, J, \Pi\right) = \frac{d}{dE} N(E, J, \Pi) \tag{2.23}$$

The total level density ϱ^{tot} is obtained by summing ϱ over all spins and parities.

$$\varrho^{\text{tot}}\left(E\right) = \sum_{J} \sum_{\Pi} \varrho\left(E, J, \Pi\right) \tag{2.24}$$

Usually, a factorized form is used to calculate the level density for a certain spin and parity ϱ from the total level density ϱ^{tot}.

$$\varrho\left(E, J, \Pi\right) = P\left(E, J, \Pi\right) f\left(E, J\right) \varrho^{\mathrm{tot}}\left(E\right) \tag{2.25}$$

Here, $P\left(E, J, \Pi\right)$ is the parity distribution factor and $f\left(E, J\right)$ is the spin distribution factor, discussed in section (2.4.2). If the excitation energy is not too small ($E >$ few MeV), an equal distribution of levels with positive and negative parity is assumed, which means $P = \frac{1}{2}$.

2.4.1 The Total Level Density

Experimental information about the level density of nuclei is derived at energies around and below the neutron separation energy S_{n} from neutron resonances and from nuclear spectroscopy in the low-energy region. At some energy the spectroscopic information ceases and one has to interpolate the level density up to S_{n}. For the description of the total nuclear level density ϱ^{tot} different models exist. The most widespread macroscopic ones are the Back-Shifted Fermi Gas Model (BFM) and the Constant Temperature Model (CTM).

In the **Back-Shifted Fermi Gas Model** [Huizenga and Moretto, 1972] the nucleus is treated as a system of non-interacting fermions. In statistical mechanics the total level density can be calculated via inverse Laplace transform of the grand partition function of a system. For a system of non-interacting fermions one obtains:

$$\varrho^{\mathrm{tot}}_{\mathrm{BFM}}\left(E\right) = \frac{1}{\sqrt{2\pi}\sigma} \frac{\sqrt{\pi}}{12} \frac{\mathrm{e}^{2\sqrt{aU}}}{a^{1/4} U^{5/4}} \tag{2.26}$$

In equation (2.26) a is the level density parameter, U is the back-shifted energy ($E - \Delta$), and σ is the spin cut-off factor which is discussed in subsection (2.4.2). The level density parameter a is given by:

$$a = \pi^2 \frac{g(E_f)}{6} \tag{2.27}$$

where $g(E_f)$ is the single particle level density at the Fermi energy.

[Ignatyuk et al., 1975] have shown that a is energy dependent and related to shell effects.

$$a(E) = \tilde{a}\left(1 + \delta W \frac{1 - \mathrm{e}^{-\gamma U}}{U}\right) \tag{2.28}$$

Here, δW is the shell effect and γ is a damping parameter. The two parameters $\tilde{a}$ and Δ of the BFM are obtained by fits to the distribution of states at low energies known from spectroscopy and states close to the neutron separation energy known from neutron capture experiments. Compilations of values for 310 nuclei and a global systematic are given in [Koning et al., 2008] and [Egidy and Bucurescu, 2009].

If the back shift energy Δ is positive, a singularity at $E = \Delta$ in equation (2.26) appears ($\varrho^{\mathrm{tot}}_{\mathrm{BFM}}(\Delta) \to \infty$). This singularity can be avoided by using the approach given in [Grossjean and Feldmeier, 1985]:

$$\tilde{\varrho}^{\mathrm{tot}}_{\mathrm{BFM}}(E) = \left[\frac{1}{\varrho^{\mathrm{tot}}_{\mathrm{BFM}}(E)} + \frac{1}{\varrho_0(E)}\right]^{-1} \tag{2.29}$$

where $\varrho_0(E)$ is given by:

$$\varrho_0(E) = \frac{a}{12\sigma} \mathrm{e}^{aU+1} \tag{2.30}$$

The **Constant Temperature Model** [Gilbert and Cameron, 1965] is based on the observation that the cumulative number of all states is proportional to an exponential function in the low energy region.

$$N(E) = \mathrm{e}^{(E-E_0)/T} \tag{2.31}$$

According to equation (2.23) the Constant Temperature total level density is given by:

$$\varrho^{\mathrm{tot}}_{\mathrm{CTM}}(E) = \frac{1}{T} \mathrm{e}^{(E-E_0)/T} \tag{2.32}$$

Here, T is the nuclear temperature and E_0 is a back-shift energy. Systems at a phase change like melting ice are known to have a constant temperature, when energy is transferred to them. In a nucleus, this phase change can be interpreted as breakups of proton and neutron pairs leading to many new degrees of freedom.

As in the case of the BFM, the parameters of the CTM are obtained from fits to experimental known states. Assuming a temperature T, it is possible to calculate the value of E_0 from the known mean s-wave neutron capture resonance spacings D_0 given in [Mughabghab, 2006].

$$D_0 = \left[\varrho(S_{\mathrm{n}}, J_{\mathrm{T}} + \frac{1}{2}, \Pi_{\mathrm{T}}) + \varrho(S_{\mathrm{n}}, J_{\mathrm{T}} - \frac{1}{2}, \Pi_{\mathrm{T}})\right]^{-1} \tag{2.33}$$

where J_{T} and Π_{T} are spin and parity of the target nucleus.

For the nucleus ^{78}Se, the CTM and BFM total level density and the calculated cumulative number of levels are shown in figure (2.8). It is visible that both models match at the neutron separation energy ($S_n = 10.5\,\mathrm{MeV}$), because they are fixed at this point. In the low energy region it is possible to compare the experimentally known cumulative number of levels to the theoretical predicted one. One sees that there is a good agreement between the experimental number and the CTM whereas the BFM yields a poorer agreement in the low-energy region. At excitation energies above 4 MeV, the experimental level schemes becomes incomplete and thus deviates from both models. This is due to the fact that at these excitation energies the mean spacing between excited states becomes smaller than energy resolution of the best gamma ray detectors.

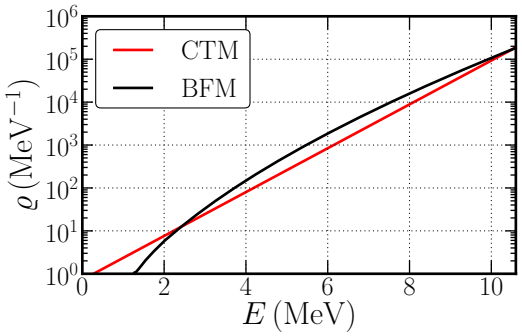

(a) Comparison of CTM and BFM total level density. Both models are fixed at the neutron separation energy (S_n = 10.5 MeV)

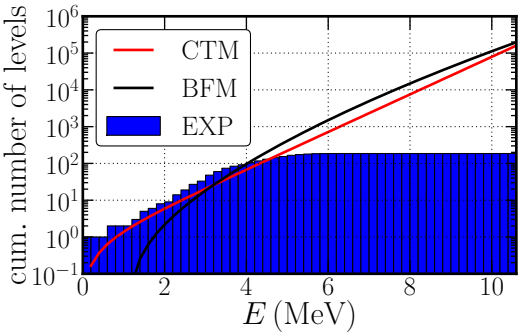

(b) Comparison of the cumulative number of levels from spectroscopy (EXP) and BFM and CTM prediction. The CTM gives a better agreement in the low energy region. At energies above 4 MeV the number of experimental levels is incomplete.

Figure 2.8: Total level density for ^{78}Se. For the Constant Temperature Model a temperature $T = 850\,\mathrm{keV}$ [Koning et al., 2008] and a back shift energy $E_0 = 413\,\mathrm{keV}$ was used. For the Back-Shifted Fermi Gas Model (BFM) a level density parameter $a(S_\mathrm{n}) = 10.74\,\mathrm{MeV}^{-1}$ and a back shift $\Delta = 1.27\,\mathrm{MeV}$ was taken. The experimental number of cumulative levels is taken from [RIP, 2011].

Recently it has been shown in [Schmidt and Jurado, 2011], [Voinov et al., 2009] and [Guttormsen et al., 2003] that the CTM describes the dynamics of different nuclear reactions, like energy transfer between fission fragments or particle evaporation spectra better than the BFM. The three articles state that the CTM gives good agreement with experimental data up to excitation energies of $10 \ldots 20\,\mathrm{MeV}$. Due to this fact, the CTM will be used as the standard model for the total level density in the further analysis.

2.4.2 The Spin Distribution of States

The spin distribution of excited states is described by the spin distribution factor f. It was calculated by [Ericson, 1960] as:

$$f(J,\sigma) = \mathrm{e}^{-J^2/2\sigma^2} - \mathrm{e}^{-(J+1)^2/2\sigma^2} \tag{2.34}$$

Where J is the spin of the state and σ is the spin cut-off parameter. The spin distribution factor $f(J,\sigma)$ is shown for different spin cut-off parameters σ in figure (2.9). It is visible that with increasing σ the distribution gets broader and the maximum of the distribution moves to higher spins.
Obviously, equation (2.34) crucially depends on the spin cut-off parameter σ. [Ericson, 1960] derived a theoretical model for the energy dependences of the spin cut-off parameter σ given by:

$$\sigma^2 = gt\langle m^2 \rangle \tag{2.35}$$

Where g is the density of single particle states, t is the temperature given by $\sqrt{U/a}$, a is the level density parameter and U the back shifted energy. $\langle m^2 \rangle$ is the expectation value of the square of the spin projection on the z or symmetry axis for single particle states.
In the article about global and local level density models [Koning et al., 2008] a combined way to express the energy dependence of σ is used.
In the low energy region ($E < E_\mathrm{d}$) σ is given by a constant σ_d obtained from the spins of experimental known states.

$$\sigma_\mathrm{d}^2 = \frac{\sum_{i=N_\mathrm{L}}^{N_\mathrm{U}} J_i(J_i+1)(2J_i+1)}{3\sum_{i=N_\mathrm{L}}^{N_\mathrm{U}} (2J_i+1)} \tag{2.36}$$

The sums in equation (2.36) run over all levels from a lower state N_L at energy E_L to an upper state N_U at energy E_U. The energy E_d up to which the constant value σ_d is used is given by:

$$E_\mathrm{d} = \frac{1}{2}\left(E_\mathrm{U} - E_\mathrm{L}\right) \tag{2.37}$$

Above the neutron separation energy, σ is calculated under the assumption of a rigid rotor to:

$$\sigma^2 = 0.01389 A^{5/3} \frac{\sqrt{aU}}{\tilde{a}\,\mathrm{MeV}} \tag{2.38}$$

Where U is the back shifted energy, a is the energy dependent level density parameter given in equation (2.28) and $\tilde{a}$ is the asymptotic value of a.

In the intermediate energy region ($E_\mathrm{d} \leq E < S_\mathrm{n}$) the value of σ^2 is interpolated linearly between the values of σ_d^2 at E_d and σ^2 at S_n from equation (2.38).
In the three energy regions, the energy dependence of σ is given by:

$$\sigma^2_\mathrm{Koning} = \begin{cases} \sigma_\mathrm{d}^2 & \text{, for } E < E_\mathrm{d} \\ \sigma_\mathrm{d}^2 + \dfrac{E - E_\mathrm{d}}{S_\mathrm{n} - E_\mathrm{d}}\left(\sigma^2(S_\mathrm{n}) - \sigma_\mathrm{d}^2\right) & \text{, for } E_\mathrm{d} \leq E < S_\mathrm{n} \\ 0.01389 A^{5/3} \dfrac{\sqrt{aU}}{\tilde{a}\,\mathrm{MeV}} & \text{, for } E \geq S_\mathrm{n} \end{cases} \tag{2.39}$$

The spin distribution and spin cut-off factor are of great importance in the treatment of level densities. As mentioned, the total level density is deduced from s-wave neutron resonances. These resonances reveal only the distribution of states with certain spins. Thus an assumption for the spin distribution at the neutron threshold is crucial for the fit of the total level density. For the sake of consistency, the level density and spin cut-off parameters are taken from [Koning et al., 2008] in the further analysis.

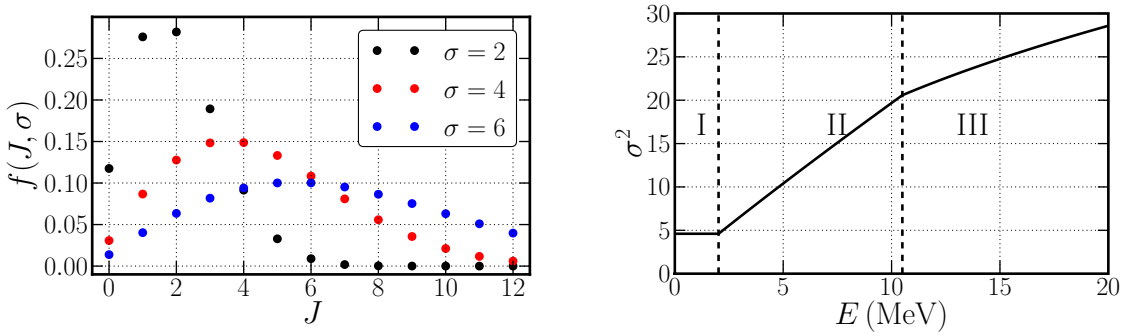

(a) The spin distribution factor $f(J)$ for different spin cut-off parameters σ.

(b) The Koning model for σ. In the low-energy region I σ^2 is constant. In region II σ^2 is proportional to E and in the high-energy region III it is proportional to $\sqrt{E-\Delta}$.

Figure 2.9: The spin distribution factor f and spin cut-off factor σ^2 for ^{78}Se

2.5 Photon Strength Functions

Photon strength functions play an important role in the statistical treatment of radiative processes in nuclei. [Bartholomew et al., 1973] defined the gamma ray (photon) strength function f as follows:
"The gamma-ray strength function ... is the distribution, as a function of γ-ray energy, of the average reduced width for transitions of a particular multipole type. ... Regions where it is appropriate to discuss level densities instead of single levels are also regions where it is useful to think in terms of γ-ray strength functions instead of individual radiation widths."
In the treatment of photon strength functions one has to distinguish between a strength function for photoexcitation (the nucleus is excited from a lower level l at E_l to a higher one h at E_h) and a strength function for photodeexcitation (the nucleus deexcites from a higher level h at E_h to a lower one l at E_l). These two functions are labeled with $\overrightarrow{f}$ for excitation and $\overleftarrow{f}$ for deexcitation.

The strength function for photo excitation is given by [Bartholomew et al., 1973]:

$$\overrightarrow{f}^{J}_{ifXL}(E_\gamma) = \frac{\langle\Gamma\rangle^{J}_{\gamma ifXL}\ \varrho(E_f, J)}{E_\gamma^{2L+1}} \tag{2.40}$$

In equation (2.40) $E_\gamma = E_f - E_i$ is the gamma-ray energy. The initial state i is fixed whereas the final one f is variable. All other symbols in equation (2.40) are explained in table (2.2).
The strength function for photodeexcitation of a state i' with spin J to a lower state f' is defined by:

$$\overleftarrow{f}^{J}_{i'f'XL}(E_\gamma) = \frac{\langle\Gamma\rangle^{J}_{\gamma i'f'XL}\ \varrho(E_{i'}, J)}{E_\gamma^{2L+1}} \tag{2.41}$$

symbol	definition
$\varrho(E, J)$	density of states with spin J at excitation energy E
$\langle\Gamma\rangle^{J}_{\gamma i f XL}$	average radiative width for transitions between state i of spin J and state f
XL	transition multipolarity ($E1$, $M1$, $E2$ ...)
E_γ	gamma transition energy

Table 2.2: Symbols for gamma-ray strength functions

The difference between the last two equations is that in (2.40) the low lying state i is fixed whereas in (2.41) the high lying one i' is fixed. Apart from that, both definitions are identical.

The **Axel-Brink hypothesis** [Brink, 1955] states that the photon strength function does not depend on the properties (energy, spin, etc.) of the initial state which means it is only a function of the transition energy $f = f(E_\gamma)$. Assuming this hypothesis, $\overrightarrow{f}$ and $\overleftarrow{f}$ are identical.
In the next subsection, models for strength functions of the most relevant transition types ($E1$ and $M1$) for the description of neutron capture gamma and photon scattering spectra are presented.

2.5.1 E1 Strength Functions

Most of the knowledge about $E1$ strength functions comes from measurements of photonuclear reactions ((γ,xn) $x = 1, 2, \ldots$). Assuming that above the neutron threshold these are the dominant interaction channels of photons, the measured cross sections can be converted into a photon strength function. All (γ,n) cross sections show a broad maximum in the energy region of $10 \ldots 20\,\mathrm{MeV}$. The character of this maximum was found to be $E1$ and called "Isovector Giant Dipole Resonance' (GDR). In the article [Goldhaber and Teller, 1948], the GDR is treated as a collective vibration of all protons against all neutrons in the nucleus. This concept was refined in [Steinwedel et al., 1950] as a interpenetrating motion of an incompressible proton and neutron fluid under the condition of a constant total nucleon density and a constant nuclear radius. For spherical nuclei the GDR is a broad one-humped maximum. In contrast, for well deformed nuclei a two-humped shape is apparent, which was explained with the existence of two collective oscillations - one along each deformation axis. In the past, the photo neutron data were described by two Lorentzians for well deformed nuclei and with one Lorentzian for spherical ones with a fixed width (Standard Lorentzian Model SLO [Axel, 1962]) or with an energy dependent width (Enhanced Generalised Lorentzian Model EGLO [Kopecky et al., 1993]). Extrapolations of these fits to low energies are at the moment the standard description for $E1$ strength functions below the neutron separation energy.
Since it is known that triaxial nuclei exist, [Junghans et al., 2008] suggested a new parametrization of the GDR average absorption cross section and the related $E1$

strength function with three Lorentzians (TLO) taking into account the existence of three oscillations along three different axis. The centroid energies E_k ($k = 1, 2, 3$) of the three Lorentzians are proportional to the length of the semi-axis and thus determined by the mass number A, the quadrupole deformation β and the triaxiality parameter γ.

$$E_k = \frac{E_0}{\mathrm{e}^{\sqrt{5/4\pi}\beta\cos\left(\gamma - \frac{2}{3}k\pi\right)}} \tag{2.42}$$

Where the energy E_0 is given in the Finite Range Droplet Model (FRDM) and a function of A and of the parameters of the liquid droplet. Results of hydrodynamical calculations can be used to compute the width of each Lorentzian:

$$\Gamma_k = 1.99\,\mathrm{MeV} \cdot \left(\frac{E_k}{10\,\mathrm{MeV}}\right)^{1.6} \tag{2.43}$$

Obviously, the widths Γ_k depend only on the centroid energy E_k. Adding up all three Lorentzian contributions, one obtains the average photoabsorption cross section:

$$\langle\sigma_{\gamma,\mathrm{abs}}\rangle\,(E_\gamma) = \frac{1.02 \cdot 11.9 \cdot ZN}{3\pi A} \sum_{k=1}^{3} \frac{E_\gamma^2 \Gamma_k}{(E_k^2 - E_\gamma^2)^2 + E_\gamma^2 \Gamma_k^2}\,\mathrm{MeVfm}^2 \tag{2.44}$$

The fraction in front of the sum guarantees that the Thomas-Reiche-Kuhn (TRK) sum rule is fulfilled. The latter one gives a value for the non-relativistic frequency-weighted integrated total absorption strength of a quantum system which interacts by velocity-independent forces only. The TRK sum rule has been tested thoroughly in nuclear, atomic, and mesoscopic systems. The electric dipole strength function f_{E1} can be calculated from the average photoabsorption cross section using equation (2.10).
It has to be emphasised that the TLO model is a global prediction with a smooth dependence of Γ on A whereas SLO and EGLO are fits to (γ,n) cross sections separately for each nucleus leading to a irregular dependence of the GDR width Γ on A.

In order to test $E1$ strength function models, they have to be compared with experimental data. In particular, the related average photoabsorption cross section can be compared to measured photonuclear cross sections. Two of these comparisons are shown in figure (2.10). For the two considered nuclei ^{78}Se and ^{196}Pt, the three Lorentzian model fits well to the experimental data in the region between the neutron threshold and the GDR maximum. Above the GDR maximum the theoretical prediction deviates from the experimental data, because other channels such as (γ,2n) contribute to $\langle\sigma_{\gamma,\mathrm{abs}}\rangle$.

The performed neutron capture and photon scattering experiments provide information about the strength function below the neutron separation energy, where the only contribution to photoabsorption is inelastic and elastic photon scattering. The gained experimental data from the performed neutron capture and photon scattering experiments can answer the question whether an extrapolation of the GDR down to

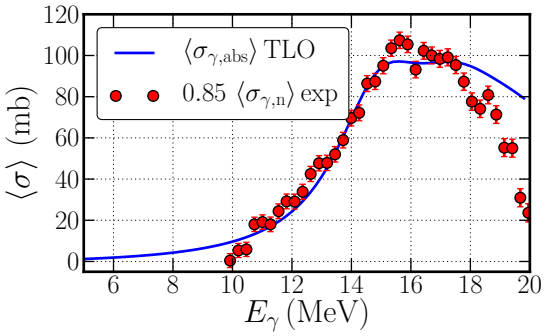

(a) Cross sections for ^{78}Se ($\beta = 0.271$,$\gamma = 27.1°$). The experimental data are taken from [Carlos et al., 1976].

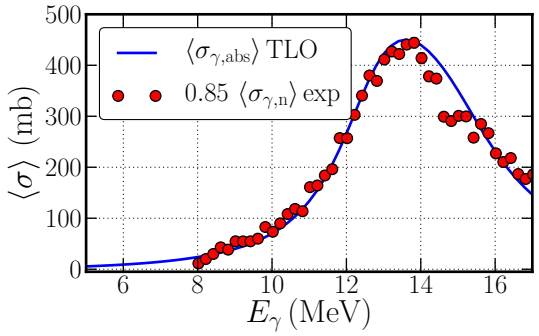

(b) Cross sections for ^{196}Pt ($\beta = 0.13$,$\gamma = 31.9°$). The experimental data are taken from [Goryachev and Zalesnyi, 1978].

Figure 2.10: Comparison of the calculated average photoabsorption cross section $\langle\sigma_{\gamma,\mathrm{abs}}\rangle$ from the TLO model (blue line) and experimental photo neutron cross sections $\langle\sigma_{\gamma,\mathrm{n}}\rangle$ (red circles). The Carlos data are scaled with 0.85 because it was found that the normalisation of the Saclay group was incorrect [Berman et al., 1987]. The assumption is made that the bremsstrahlung data measured by Goryachev and corrected by Varlamov also depends on the Saclay normalisation and thus have to be scaled, as well.

energies below S_n (which is the standard method at the moment for statistical calculations) is justified or whether the shape of the strength deviates from a Lorentzian. This is important, e.g. for the calculation of the total radiative width Γ_tot which is given by [Bartholomew et al., 1973]:

$$\Gamma^J_{\gamma,\mathrm{tot}} = \int_0^{S_\mathrm{n}} E_\gamma^3 f_{E1+M1} \frac{\sum_{I=|J-1|}^{J+1} f\left(I, \sigma\left(S_\mathrm{n} - E_\gamma\right)\right)}{f\left(J, \sigma\left(S_\mathrm{n}\right)\right)} \frac{\varrho^\mathrm{tot}(S_\mathrm{n} - E_\gamma)}{\varrho^\mathrm{tot}(S_\mathrm{n})} dE_\gamma \tag{2.45}$$

In many articles, the ratio of the spin distribution factors $f(J)$ at the final and initial state is approximated by 3 which only holds if $f(J)$ is a linear function of J in the region $|J-1|, \ldots, J+1$. It is visible in figure (2.9) that this assumption is not valid for all J and σ.
An enhanced strength below S_n would result in an increased total radiative width which for example directly influences the neutron capture cross section. With increasing total radiative width the ratio of captured to scattered neutron increases as well. As mentioned in the introduction, this ratio is important for simulations of neutron spectra in transmutation facilities.

2.5.2 M1 Strength Functions

It is shown in [Heyde et al., 2010] that the magnetic strength distribution below the neutron separation energy has three contributions. These are the orbital or scissors mode, the isoscalar and the isovector spin flip mode. A first attempt to convert and parametrise the given reduced matrix elements $B(M1)$ into a M1 strength function

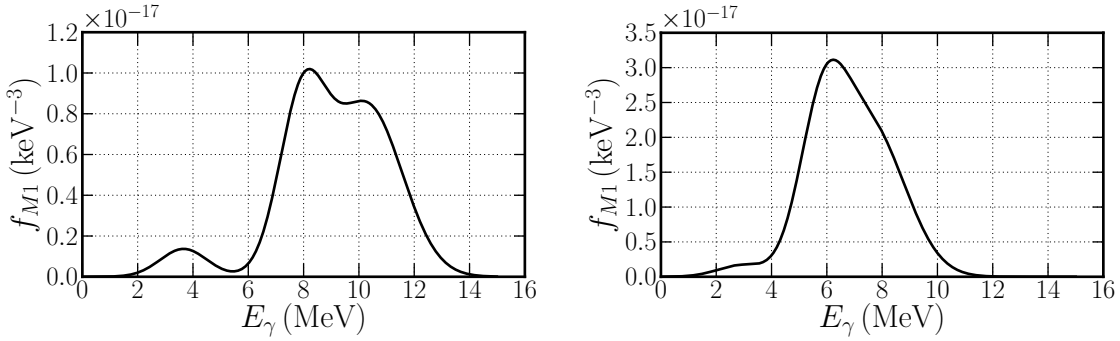

(a) ^{78}Se (b) ^{196}Pt

Figure 2.11: $M1$ strength functions according to the parametrisation (2.46). The orbital mode in ^{78}Se is very prominent due to the large quadrupole deformation ($\beta = 0.271$)

M1 mode	amplitude A_k	central energy E_k	standard deviation σ_k
orbital	$\frac{(Z\beta)^2}{62}\,\mathrm{GeV}^{-3}$	$0.21 E_{\mathrm{GDR}}$	0.85 MeV
isoscalar spinflip	$\frac{A}{9.3}\,\mathrm{GeV}^{-3}$	$34\,A^{-1/3}$ MeV	0.85 MeV
isovectorial spinflip	$\frac{A}{9.3}\,\mathrm{GeV}^{-3}$	$44\,A^{-1/3}$ MeV	1.27 MeV

Table 2.3: Parameters used for the M1 strength function parametrization

was done by Prof. Grosse[1]. For the three contributions Gaussians are used instead of Lorentzians.

$$f_{M1} = \sum_{k=1}^{3} A_k \mathrm{e}^{\frac{-(E-E_k)^2}{2\sigma_k^2}} \tag{2.46}$$

Here, the amplitudes A_k, central energies E_k and standard deviations σ_k are given in table (2.3). Figure (2.11) shows the $M1$ strength distribution for ^{78}Se and ^{196}Pt according to equation (2.46). Compared to the $M1$ strength, the $E1$ strength at the maximum of the $M1$ strength is 5 times greater.

2.6 The Statistical Fluctuation Factor

At high excitation energies nuclear physics measurements often face the complication of spacing between excited states being smaller than the detector resolution. Thus it is only possible to measure average quantities. [Lynn, 1968] and [Axel et al., 1970] have shown that fluctuations in the transition widths lead to an enhancement of elastic transitions in neutron scattering and (γ,p) measurements. As derived in

[1] private communication, 2010

section (2.2), the same effect occurs in photon scattering where the average elastic scattering cross section is enhanced by a factor S compared to the product average photoabsorption cross section and average ground state branching ratio.

$$\langle \sigma_{\mathrm{scat}}(E) \rangle = \langle \sigma_{\mathrm{abs}}(E) \rangle \cdot \frac{\langle \Gamma_{\gamma,0i} \rangle}{\langle \Gamma_{i,\mathrm{tot}} \rangle} \cdot S$$

In general the influence of fluctuations on elastic photon scattering between the ground state 0 and an excited state i can be defined as [Bartholomew et al., 1973]:

$$S = \left\langle \Gamma_{0i} \frac{\Gamma_{i0}}{\Gamma_{i,\mathrm{tot}}} \right\rangle \Bigg/ \left(\frac{\langle \Gamma_{0i} \rangle \langle \Gamma_{i0} \rangle}{\langle \Gamma_{i,\mathrm{tot}} \rangle} \right) \tag{2.47}$$

The averaging is done over several excited states i in an energy bin $\left[E_i - \frac{\Delta}{2}, E_i + \frac{\Delta}{2}\right]$. As will be shown later on, it is reasonable to express S as a function of the ratio of average inelastic to elastic transition width $R = \sum_{j>0} \langle \Gamma_{ij} \rangle / \langle \Gamma_{i0} \rangle$. The latter is determined by the level density (the number of possible deexcitation channels) and the photon strength function (the probability of the single channels). If there is only one possible channel (deexcitation back to the ground state), S is unity. On the other hand, if there are many possible open channels (transitions to lower excited states), the total radiative width $\Gamma_{i,\mathrm{tot}}$ is the sum of many single transition widths and thus according to the central limit theorem it should not fluctuate strongly. Therefore it is justified to write:

$$\left\langle \Gamma_{0i} \frac{\Gamma_{i0}}{\Gamma_{i,\mathrm{tot}}} \right\rangle = \frac{1}{N \langle \Gamma_{i,\mathrm{tot}} \rangle} \sum_{i,E_i \in \mathrm{bin}} \Gamma_{0i} \Gamma_{i0} = \frac{\langle \Gamma_{0i} \rangle^2}{N \langle \Gamma_{i,\mathrm{tot}} \rangle} \sum_{i,E_i \in \mathrm{bin}} y_{0i}^2 = \frac{\langle \Gamma_{0i} \rangle^2}{\langle \Gamma_{i,\mathrm{tot}} \rangle} \langle y_{0i}^2 \rangle \tag{2.48}$$

Equation (2.48) shows that for a non fluctuating total radiative width the enhancement is given by $\langle y_{0i}^2 \rangle$ which is the mean of the squared fluctuation distribution of the single transition widths. Assuming a reduced chi-square distribution with ν degrees of freedom for the y_{ij}, one obtains:

$$S(\Gamma_{i,\mathrm{tot}} \approx \langle \Gamma_{i,\mathrm{tot}} \rangle) = 1 + \frac{2}{\nu} \tag{2.49}$$

For the analysis of photon scattering experiments, S has to be calculated in the energy range $0...S_{\mathrm{n}}$. In this energy region the approximation $\Gamma_{i,\mathrm{tot}} \approx \langle \Gamma_{i,\mathrm{tot}} \rangle$ does not hold and thus S has to be simulated numerically. For this purpose a numerical simulation has been developed which operates in the following way which is visualised in figure (2.12):

1. This simulation code generates a nuclear mock level scheme, with N_{tot} states up to an energy $E + \frac{\Delta}{2}$ according to the nuclear level density. Given that photon scattering is dominated by $E1$ excitations and 0^+ target nuclei are used, only 0^+, 1^- and 2^+ levels are distributed because only those states can be populated in a two step $E1$ excitation and deexcitation process.

2. All average transition widths $\langle \Gamma_{ij} \rangle$ between all states are calculated using equation (2.1).

3. Each average transition width is multiplied with a random variable y_{if} drawn from a reduced chi-square distribution with ν degrees of freedom.

4. The two quantities $\left\langle \frac{\Gamma_{0i}\Gamma_{0i}}{\Gamma_{i,\mathrm{tot}}} \right\rangle$ and $\frac{\langle\Gamma_{0i}\rangle\langle\Gamma_{0i}\rangle}{\langle\Gamma_{i,\mathrm{tot}}\rangle}$ are calculated, where the averaging is done over all 1^- states i in the bin $\left[E - \frac{\Delta}{2}, E + \frac{\Delta}{2}\right]$. By division of these last two quantities, the statistical fluctuation factor S is obtained for elastic ground state transitions for one mock level scheme.

The simulation algorithm is executed several times each time with a new mock random scheme of excited states and new fluctuations of the transition widths. In the end the mean value for S deduced from all mock state schemes is taken.

Figure (2.13) shows simulated values of S for different excitation energies for ^{78}Se. For the calculation a TLO $E1$ strength function with $\beta = 0.271$ and $\gamma = 27.1°$ was used. The states in the mock level scheme were distributed according to a Constant Temperature level density with $E_0 = 413\,\mathrm{keV}$ and three different temperatures ($T = 800\,\mathrm{keV}, 850\,\mathrm{keV}, 950\,\mathrm{keV}$). The spins of the states were assigned according to the spin-cutoff factor given in [Koning et al., 2008]. The averaging was performed over 200 keV bins and the fluctuations of the single transition widths y_{ij} were drawn from a chi-square distribution with one degree of freedom (Porter-Thomas distribution). In the low-energy region ($E_\gamma \lesssim 3000\,\mathrm{keV}$), where on average there are one or less states in the averaging bin, S is one. With increasing excitation energies, S increases as well, until it reaches the limiting value of 3 at high excitation energies for the assumed Porter-Thomas distribution. For energies above 10.5 MeV S could not be simulated because the exponentially increasing number of excited states caused computer memory problems. It is visible in figure (2.13) that for a given excitation energy, S increases with increasing level density (equivalent to an increasing T when D_0 is fixed).
Figure (2.14) shows simulated fluctuation factors S as a function of the ratio of average inelastic and elastic transition width R for different level densities and $E1$ strength functions. Obviously in regions where R is greater than 3, S is independent of strength function and level density. Furthermore it is visible, that S approaches 3 when R approaches infinity which corresponds to very high excitation energies. However, at excitation energies above the particle threshold, other reaction channels are open and thus the total width $\Gamma_{i,\mathrm{tot}}$ contains also partial particle widths which influence S [Axel et al., 1970].

In summary, it could be shown that when dealing with fluctuating transition widths, an enhancement of elastic transitions occurs. Applied to photon scattering this means that the observed yield of direct ground state transitions is enhanced by a factor S compared to the product of average ground state branching ratio $B_0 = \langle\Gamma_{i0}\rangle / \langle\Gamma_{i,\mathrm{tot}}\rangle$ times the absorbed yield. This can be realised by taking into account that in photon scattering due to fluctuations not all states in an energy bin are excited equally. Thus, the average ground state branching ratio B_0, which is an uniformly averaged value of all single branching ratios gives an incorrect estimate for the yield of direct ground state transitions of excited states in photon scattering experiments.

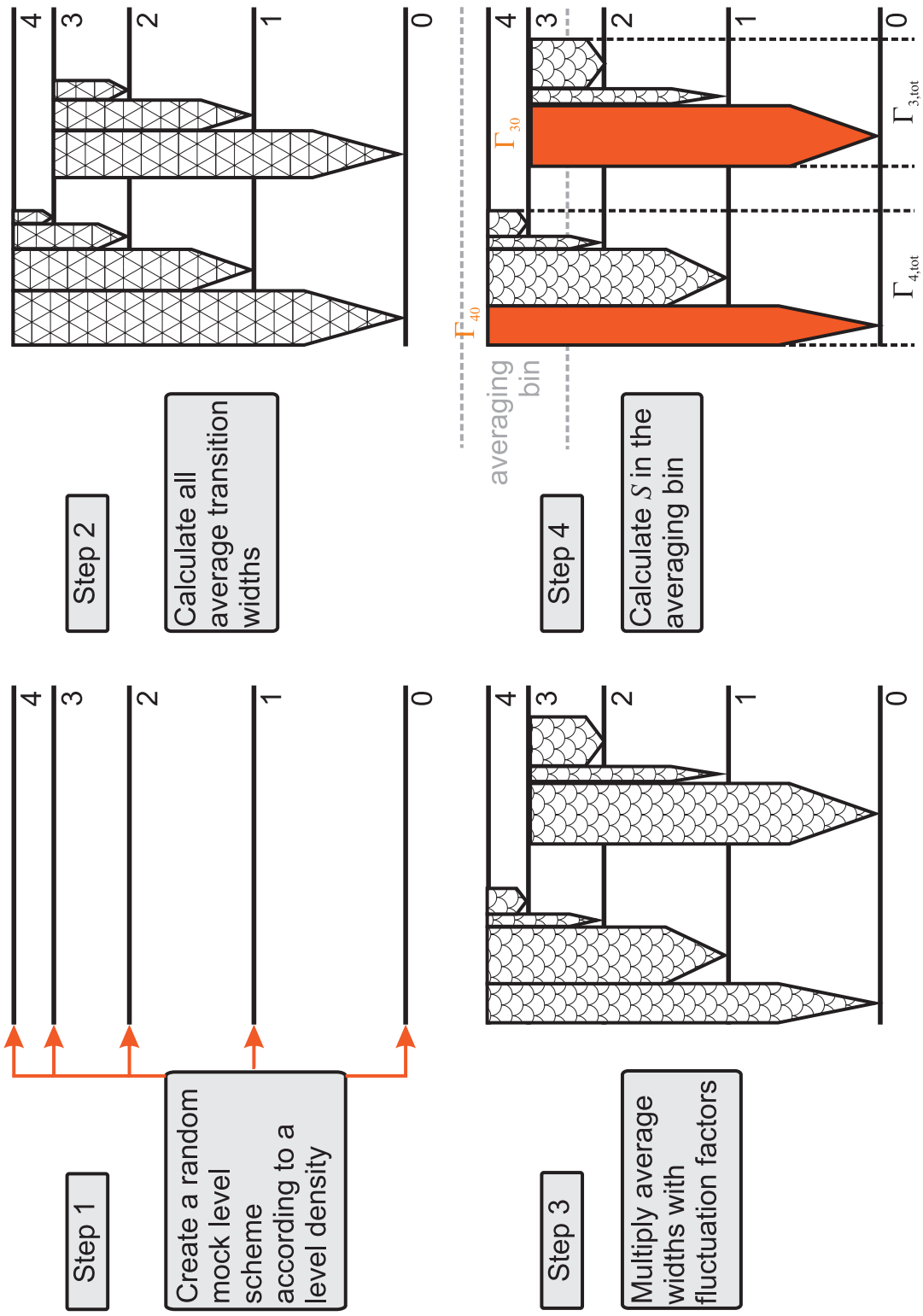

Figure 2.12: The four steps of the simulation algorithm for the statistical fluctuation factor that are explained in the text.

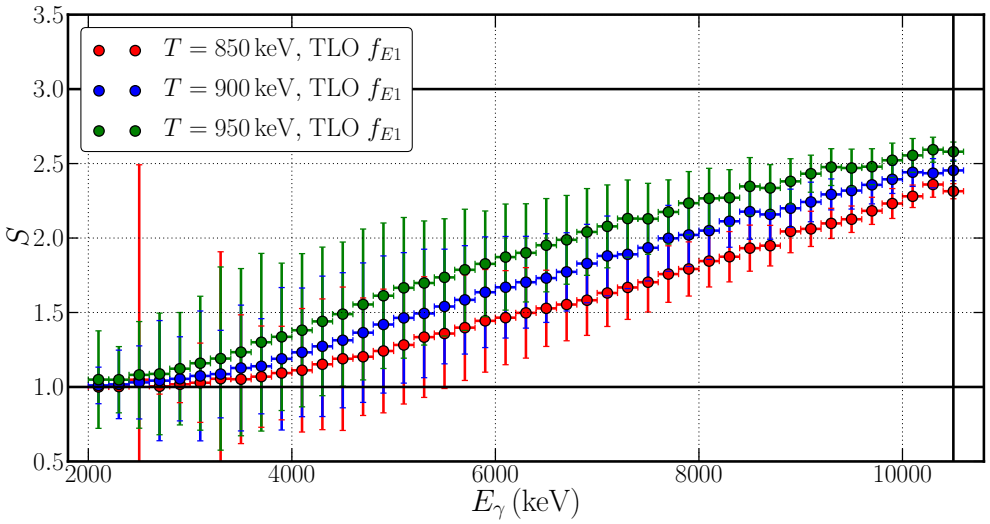

Figure 2.13: Energy dependence of the statistical fluctuation factor S for ^{78}Se. For the computation a TLO $E1$ strength function with $\beta = 0.271$ and $\gamma = 27.1°$ and a CTM level density with $E_0 = 413\,\mathrm{keV}$ and different temperatures was used. 200 keV bins were used for the averaging. The vertical black line represents the neutron separation energy and the horizontal ones correspond to the limiting cases of one and infinite states in the averaging bin. The fluctuations of the single transition widths y_{ij} were drawn from a chi-square distribution with one degree of freedom (Porter-Thomas distribution). The vertical errorbars correspond to one standard deviation of all S deduced from different mock level schemes.

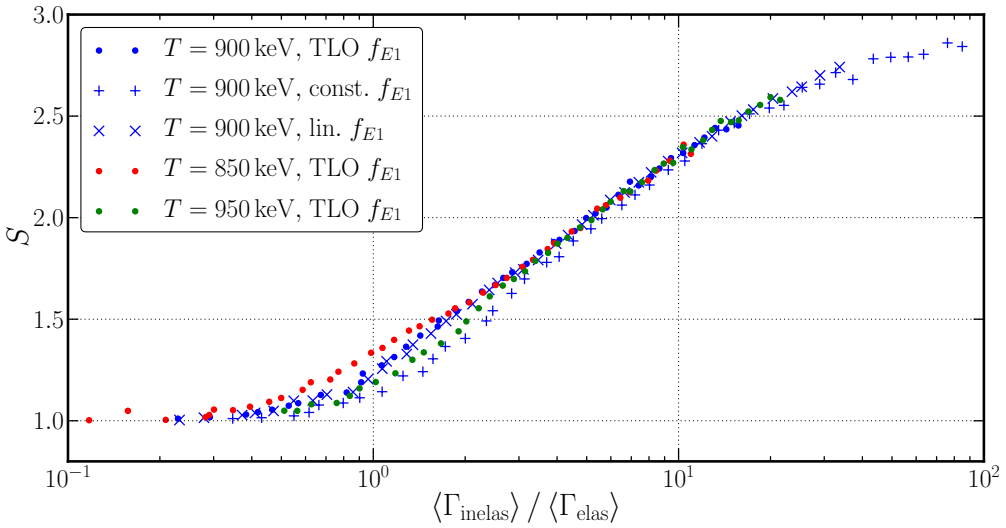

Figure 2.14: The statistical fluctuation factor S as a function of the ratio of average inelastic and elastic transition width (R) for different level densities and $E1$ strength functions.

Chapter 3
Experimental Setups

In this chapter a brief overview of the two experimental facilities used in the two twin experiments is given. Firstly, in section (3.1), the upgraded neutron-induced prompt gamma spectroscopy facility [Szentmiklósi et al., 2010] at the Institute of Isotopes (IKI) in Budapest, where the neutron capture experiments took place is described. Secondly, in section (3.2), the bremsstrahlung facility [Schwengner et al., 2005] at Helmholtz-Zentrum Dresden-Rossendorf (HZDR), where the photon scattering experiments were performed, is presented.

3.1 The Neutron Capture Setup

The Institute of Isotopes in Budapest, Hungary, operates a cold neutron source at a research reactor with a thermal power of $P_{\mathrm{th}} = 10\,\mathrm{MW}$. A floor plan of the reactor and the associated experiments is shown in figure (3.1). For neutron capture experiments cold neutrons are extremely suitable due to the $1/\sqrt{E_{\mathrm{n}}}$ dependence of the neutron capture cross section at low energies.
A tangential beam tube guides neutrons from the reactor core to a cold neutron source (CNS). The CNS uses liquid hydrogen to moderate the incoming neutrons via elastic scattering. The resulting energy spectra of the moderated neutrons follows a Maxwell distribution with a mean kinetic energy of approximately 1 meV. A bent beam tube guides the cold neutrons from the CNS to the Prompt Gamma Activation Analysis (PGAA) setup where the capture gamma ray spectra were measured. Using a tangential and bent neutron guiding system reduces the fraction of unwanted direct radiation from the reactor core impinging the measuring sample.
The PGAA setup, shown in figure (3.2), consists of an optional beam chopper, a beam collimator made of ^{6}Li enriched plastic, a sample holder and a bismuth germanate (BGO) escape-suppression shielded High Purity Germanium (HPGe) detector under an angle of 90° with respect to the beam axis. The detector was brought from HZDR.
The neutron flux in the cold range at the sample position is at maximum $5 \cdot 10^{7} \frac{1}{\mathrm{cm^2 s}}$.
In the two neutron capture experiments ^{77}Se(n,γ) and ^{195}Pt(n,γ) performed in October 2009, a BGO escape-suppression shielded Ortec 41-N31587A HPGe Detector with a relative efficiency of 100 % was used. In addition to the capture experiments on ^{77}Se and ^{195}Pt, a gamma spectrum from neutron capture on urea-d was measured. Cold neutron capture on urea-d consisting of carbon, hydrogen, deuterium, oxygen and nitrogen produces a simple gamma ray spectrum with a few and strong transitions. The shape of this spectrum can be used to test the detector response

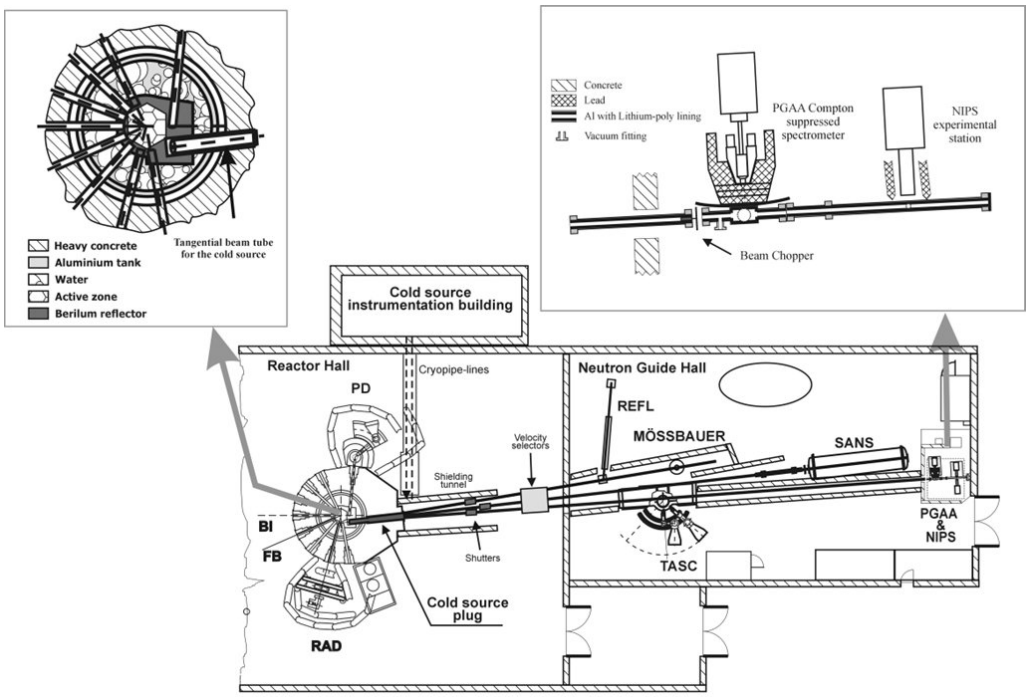

Figure 3.1: Floor plan of the research reactor at IKI Budapest and the associated experiments. For the neutron capture experiments, cold neutrons from the cold neutron source (CNS) were used. The capture gamma ray spectra were measured at the Prompt Gamma Activation Analysis (PGAA) setup. The picture is taken from [W1, 2011].

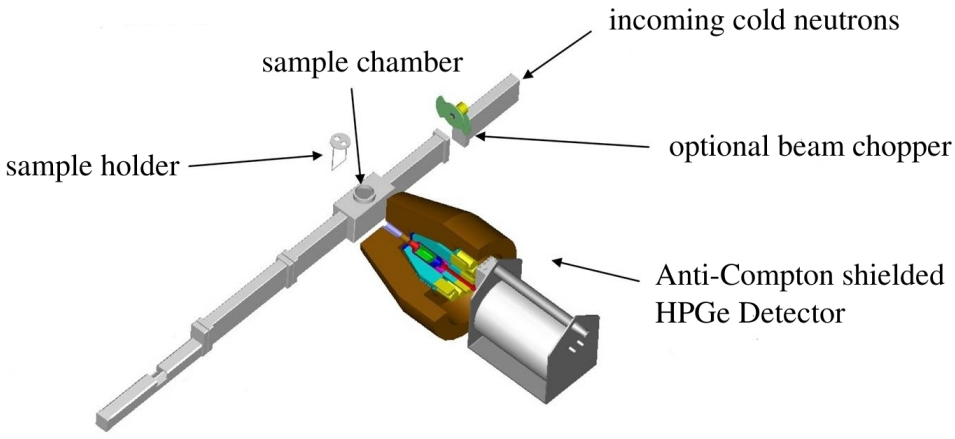

Figure 3.2: PGAA setup for measuring prompt neutron capture gamma spectra consisting of an optional beam chopper, a beam collimator, a sample holder and a BGO shielded HPGe detector. The picture is taken from [W2, 2011].

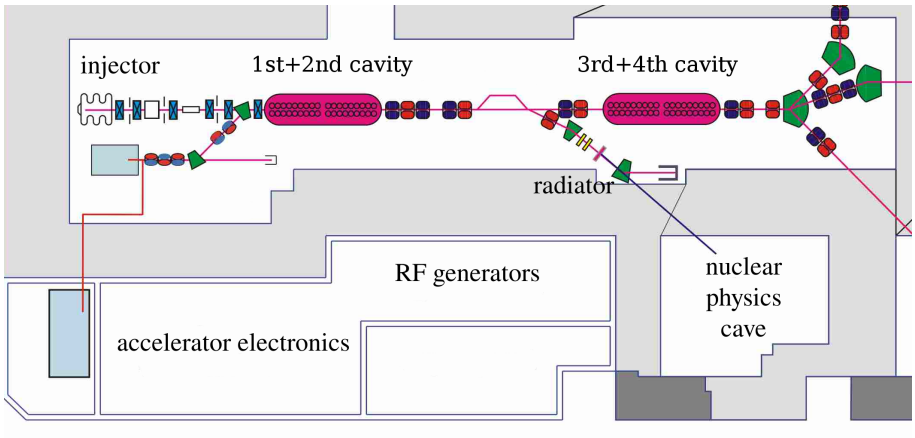

Figure 3.3: Floor plan of the photon scattering facility at ELBE. After injection by a thermionic injector, electrons are accelerated in the first superconducting cavity to at most 20 MeV. Between the second and third cavity the electron beam is deflected and focused on a niobium radiator for producing bremsstrahlung.

correction of the measured spectra needed for the further analysis.

3.2 The Photon Scattering Facility

The second part of the twin experiments, the photon scattering experiments on ^{78}Se and ^{196}Pt took place in October 2009 and in February 2010 at the photon scattering facility [Schwengner et al., 2005] of the superconducting electron accelerator for beams with high brilliance and low emittance (ELBE) at Helmholtz-Zentrum Dresden-Rossendorf (HZDR). Photon scattering experiments using a bremsstrahlung continuum have the advantage that all states up to the endpoint energy of the impinging spectrum can be excited. However, the disadvantage of bremsstrahlung excitations is the lack of knowledge of the actual absorbed photon energy and thus the excitation energy of the target nucleus. By measuring the deexcitation gamma spectra and several corrections which are discussed in (4.3), the spectrum of absorbed photons can be reconstructed.

A floor plan of the photon scattering facility and the nuclear physics cave at ELBE are shown in figures (3.3) and (3.4), respectively. The linear accelerator ELBE, which consists of 4 superconducting cavities, is able to produce electron beams up to 40 MeV with an average current of 1 mA and with a very short micro pulse length down to 1 ps in continuous wave mode. For photon scattering experiments, the electron beam is deflected behind the first two cavities under 45° and focused onto a few micro meter thin niobium radiator. Electrons impinging onto the radiator are slowed down by ionization and emission of bremsstrahlung. A purging magnet behind the radiator deflects all electrons that passed through the radiator into a beam dump. A beam of bremsstrahlung photons with a diameter of approximately 3.8 cm at the target position is shaped by a conical collimator made of pure

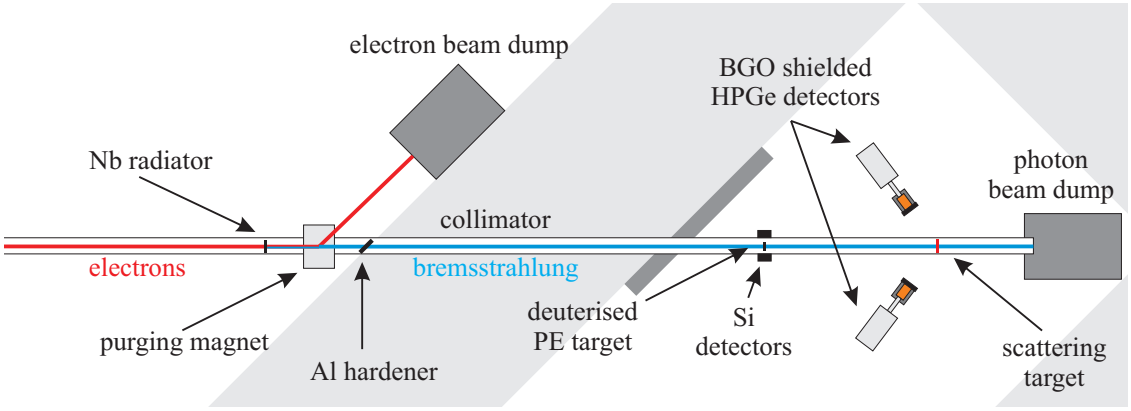

Figure 3.4: Nuclear physics cave at ELBE. Electrons from the accelerator are focused onto a thin Nb radiator and produce bremsstrahlung which is collimated through a wall of heavy concrete towards the target position. Four Silicon detectors are used for measuring proton spectra from photodisintegration of a deuterised PE target for the determination of the maximum energy of the bremsstrahlung beam. The photons scattered from the the target are detected by four bismuth germanate shielded High Purity Germanium detectors.

aluminium placed in the heavy concrete wall between the accelerator hall and the photon scattering hall. In front of the collimator a beam hardener of aluminium can be placed. Aluminium mainly absorbs photons in the low energy region and thus hardens the bremsstrahlung spectrum. For an exact determination of the kinetic energy of the electrons needed for a correct calculation of the bremsstrahlung fluence at the target, four silicon detectors are installed around the beam tube behind the collimator. These detectors are used for measuring protons from photodisintegration of a deuterised polyethylene target. Additionally, the electron beam energy can be measured with an electron spectrometer located at the chicane behind the second cavity. Around the scattering target position four High Purity Germanium (HPGe) detectors are mounted all surrounded with an escape-suppression shield made of bismuth germanate (BGO). Two HPGe detectors are installed vertically at 90° and two are mounted horizontally at 127° with respect to the beam direction. This detector arrangement is chosen to distinguish between dipole and quadrupole elastic scattering due to their different angular distribution. At the end of the beam line, the remaining photons are dumped in a lead and cadmium shielded beam dump made of polyethylene. The experimental parameters of the two photon scattering experiments are given in table (A.8) in the appendix.

Chapter 4
Data Analysis

In this chapter, the data analysis of the two twin experiments is presented. First of all in section (4.1), the most important tool, a statistical simulation for radiative deexcitations of excited nuclei, is explained. Subsequently, sections (4.2) and (4.3), deal with its application in the simulation and analysis of neutron capture and photon scattering experiments.

4.1 Simulation of Nuclear Radiative Deexcitations

Both types of experiments, neutron capture and photon scattering, have in common that deexcitation gamma spectra of excited nuclei are measured. The only difference between both experiments is the way of excitation. In cold neutron capture, the nucleus is excited via the nuclear interaction of a neutron with the target nucleus. As mentioned in section (2.1), due to the small incident kinetic energy of the neutron, one distinct state close to the neutron separation energy in the compound nucleus is excited. In contrast to neutron capture, in photon scattering experiments the nucleus is excited via the electromagnetic interaction of the impinging bremsstrahlung photons with the target nucleus. Instead of exciting only one state, all states from $E_{\mathrm{ex}} = 0$ up to the endpoint energy of the used bremsstrahlung spectrum, with respect to the selection rules, can be excited.
For the analysis of both experiments it is thus important to understand the spectral shape of gamma rays emitted in a deexcitation process of an excited state. This spectral distribution is determined by all transition widths Γ_{if} from the excited state i to all possible final states f. Theoretically, one could try to calculate all transition widths Γ_{if}, but one faces several problems:

1. The energies, spins and parities of excited states in medium and heavy nuclei are only completely known for few stable nuclei in the low energy range ($0 \leq E_{\mathrm{ex}} \lesssim 2\,\mathrm{MeV}$).

2. The number of excited states increases exponentially. In stable medium and heavy nuclei there are approximately $10^4 \ldots 10^5$ states up to the neutron separation energy.

3. Due to the complexity of the nuclear many body system, it is only possible to calculate transition widths between states in the low energy region (up to a few MeV). At higher excitation energies, average transition widths $\langle\Gamma_{if}\rangle$ calculated from photon strength functions and level densities must be used.

4. The transition widths Γ_{if} fluctuate strongly around their mean $\langle\Gamma_{if}\rangle$.

Some years ago, the simulation code DICEBOX [Becvar, 1998] was developed to simulate gamma transitions in excited nuclei. This code calculates the emitted gamma ray spectrum of an excited state by creating several mock level schemes and using fluctuating transition widths. A main application of DICEBOX is the analysis of two-step gamma cascade experiments [Becvar et al., 2007] for deducing photon strength functions in neutron capture experiments.
For the analysis of previous photon scattering experiments Gencho Rusev implemented an algorithm [Schwengner et al., 2007], [Rusev, 2007] based on DICEBOX for the simulation of radiative deexcitations of nuclei excited in photon scattering experiments. These calculations are necessary for the subtraction of inelastic events in the analysis of photon scattering experiments. However, due to the great number of excited states ($\approx 10^5$) up to the high excitation energies used in experiments at HZDR, simulations with this code are very time consuming. Typical calculations on a computing cluster took about two weeks which made a systematic analysis with varying input parameters (level density and strength functions) tedious.

For a faster calculation and a more sophisticated study of the influence of the input parameters on the simulated deexcitation spectra, a new computational approach was developed in this thesis. Instead of using many mock level schemes each containing a large number of excited states, this new approach calculates average gamma deexcitation spectra between energy bins that contain several states. Typically a bin width of 200 keV is used which reduces the number of transition possibilities dramatically leading to much shorter computation times. However, the impact of fluctuations on simulated spectra has to be considered and the validity of using averaged quantities has to be checked.

As derived in section (2.1) and shown in [Bartholomew et al., 1973] the average spectral distribution ν^J_{XL} of emitted primary gamma rays for a given transition type XL of an excited state i with spin J in the extreme statistical limit is given by:

$$\nu^J_{XL}(E_\gamma) = E_\gamma^{2L+1} \frac{f_{XL}(E_\gamma)}{\langle\Gamma_{\mathrm{tot},i}\rangle} \frac{\sum_{I=|J-L|}^{J+L} \varrho(E_i - E_\gamma, I)}{\varrho(E_i, J)} \tag{4.1}$$

In equation (4.1) $\langle\Gamma_{\mathrm{tot},i}\rangle$ is the average total radiative width of the excited state i and $\varrho(E_i, J)$ is the level density of states with spin J at E_i. Since the latter two quantities are independent of the gamma ray energy, the spectral shape $\nu^J_{XL}(E_\gamma)$ is only determined by the photon strength function $f_{XL}(E_\gamma)$ and the level density at possible final states $\varrho(E_i - E_\gamma, I)$.

For practical reasons it is more suitable to use an integrated level density over an energy interval which is equivalent to the number of states in that interval instead of the level density. This has the big advantage that the position of experimentally known states can be included easily in the low-energy region by simply counting the number of experimentally known states in each bin. If the energy interval ΔE

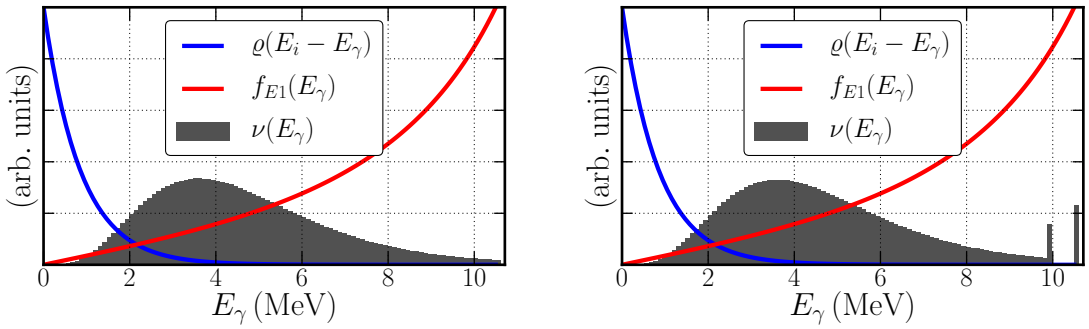

(a) Calculation without using information about experimentally known states.

(b) Calculation with two fixed discrete states at 0 keV and 613 keV

Figure 4.1: Average spectral distribution of emitted primary gamma rays from an excited state at 10.7 MeV calculated from equation (4.1). The strength function (red) and the number of states per 105 keV bin (blue) are shown in arbitrary units. Both spectral distributions are normalized to the same area.

around an energy E is not too large, the number of states in this interval is simply given by:

$$N(E, \Delta E) \approx \varrho(E) \cdot \Delta E \tag{4.2}$$

Inserting this into equation (4.1) does not change the spectral distribution of emitted primary gamma rays. Figure (4.1) shows schematically the shape of emitted primary $E1$ gamma rays calculated using equation (4.1) from an excited state at 10.7 MeV. Furthermore the gamma energy dependence of the $E1$ strength function f_{E1} and the level density at final states $\varrho(E_i - E_\gamma)$ is illustrated.
The rise and fall of the spectral distribution is caused by the two competing mechanisms of the transition strength rising with the transition energy and the exponential decline of the level density at possible final states as function of the transition energy. In the left subfigure, no information about low lying discrete states was used, whereas in the right one two states at 0 and 613 keV were inserted. It is clearly visible that the use of low lying discrete states changes the distribution at high energies.

The actual position of the maximum in the primary gamma distribution is determined by the slope and curvature of the strength function and level density. Figure (4.2) shows schematically the influence of these quantities on the spectral shape of the emitted primary gamma ray spectrum. It is visible that an increase in the steepness of level density and strength function leads to a more narrow distribution of primary gamma rays and a shift of the mean to lower and higher energies, respectively.

It should be emphasised that equation (4.1) only holds in the extreme statistical limit. It is only capable of describing the distribution of transitions to an energy interval containing several final states. Supposing that there are many possible states in the final energy interval, it is assured that fluctuations in the transition

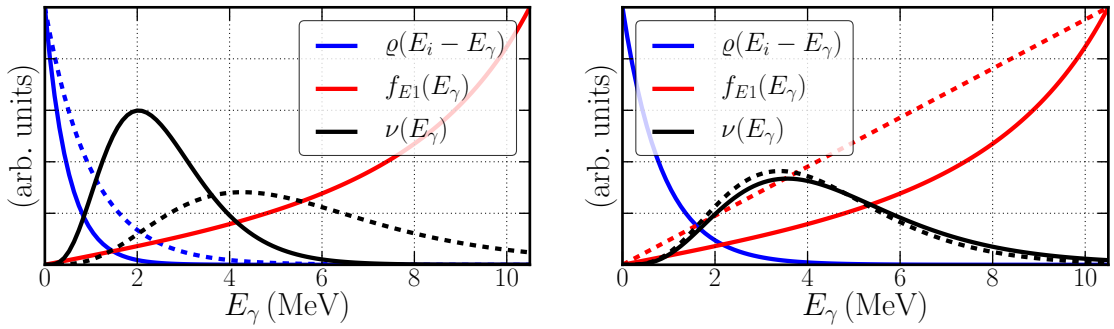

(a) Normalised primary gamma spectrum for two CTM level densities with $T = 500\,\mathrm{keV}$ (solid line) and $T = 1000\,\mathrm{keV}$ (dashed line).

(b) Normalised primary gamma spectrum for two strength functions: TLO (solid line) and linear model (dashed line).

Figure 4.2: Influence of the shape of level density at the final state (blue) and strength function (red) on the normalised primary gamma spectrum (black). The spectral distributions are normalised to the same area.

widths will average out. Situations where and where not the use of equation (4.1) is valid are discussed in the following section.

Knowing the average spectral distribution of primary gamma rays emitted from an excited state, it is moreover possible to calculate a complete gamma deexcitation cascade to the ground state including higher-order gamma rays. For this purpose a Monte Carlo simulation was developed. A visualisation of the algorithm used in the simulation is shown in figure (4.3). First of all, for a given initially excited state i, the possible final energies are divided into bins with equal width ΔE. Subsequently, the numbers of possible final states for all considered spins ($J \leq 5$) and parities are calculated separately in all energy bins using a model for the total level density and spin distribution. In the lowest bins these values are taken from experimentally known states. In the next step the spectral distribution $\nu(E_\gamma)$ of primary gamma rays to all possible final bins is computed according to equation (4.1) for $E1$, $M1$ and $E2$ transitions for all spins and parities using the respective strength functions. After a normalization of $\nu(E_\gamma)$ a uniformly distributed random number drawn into the normalized cumulative spectral distribution is used to select a final energy E_f, a final spin J_f, and a final parity Π_f. This procedure is executed with the chosen final energy as new starting energy until the ground state is reached. During the cascade deexcitations all transition energies, populated states, spins and parities are stored. In order to gain enough statistics several deexcitations processes are simulated.
The simulation algorithm was implemented in programming language Python using Scipy, a package for scientific computing. In addition a graphical user interface (GUI) for an easy and intuitive handling of the program was developed with QT4. Moreover it is possible to plot simulated results directly from the GUI with the help of the Matplotlib library.

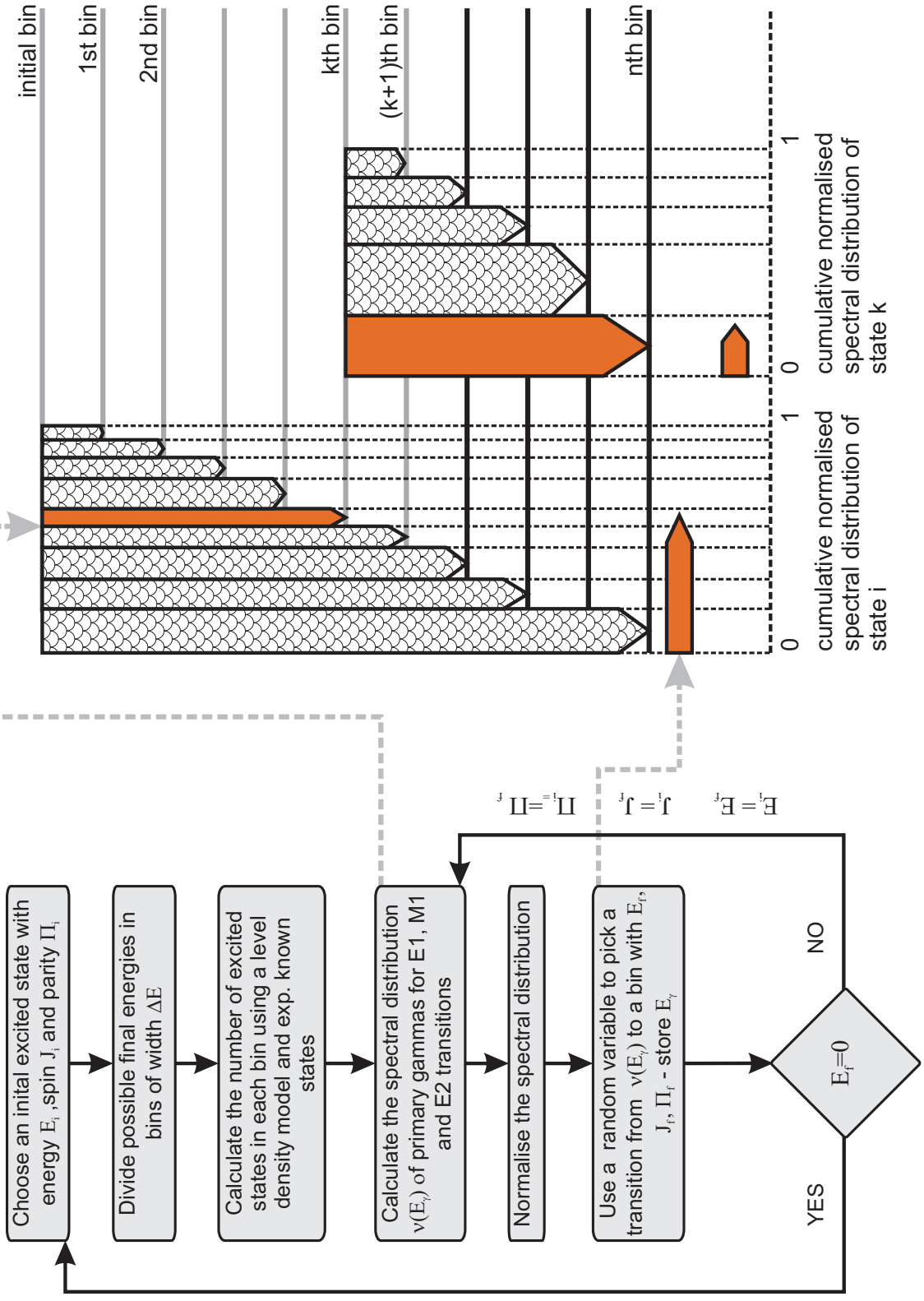

Figure 4.3: Scheme of the simulation algorithm of nuclear radiative deexcitations. According to the calculated transition probabilities from the spectral distribution of emitted gamma rays, transitions are chosen. The procedure is repeated until the ground state is reached.

4.2 Analysis of Neutron Capture Experiments

The aim of the analysis of the measured ^{77}Se(n,γ) and ^{195}Pt(n,γ) spectra is to obtain qualitative information about level density and strength function in the compound nucleus. For this purpose the following analysing steps were performed:

1. Correction of the measured spectra for background, detector response and efficiency
2. Simulation of neutron capture gamma spectra using different level densities and strength functions
3. Comparison of measured and simulated spectra

A simulation of the detector setup used in the experiment including detector response and efficiency was done with GEANT4 by [Massarczyk, 2011]. These simulations were used by Evert Birgersson to correct the measured spectra for detector response and efficiency. The efficiency correction not shown here is based on measurements with calibration sources and GEANT4 simulations for the energy range above 2 MeV. A test of this correction was performed on a measured capture gamma ray spectra of deuterised urea. This target contains nitrogen, oxygen, carbon, deuterium and hydrogen leading to a capture spectrum with few and strong gamma peaks. Figure (4.4) shows the originally measured and the response corrected spectrum. The strongest peaks result from neutron capture on hydrogen (H) and nitrogen (N). Moreover, single escape (SE) and double escape peaks (DE) are visible. The latter two and the Compton continua are detector artefacts and are removed in the response corrected spectrum. Obviously the response correction works well in the high-energy region, whereas it is imperfect in the intermediate and low-energy region. However, the ratios of the leftover artefacts to the corresponding full energy peaks are negligibly small. For the nitrogen peak at 10.8 MeV the ratio of left over artefacts from double escape, single escape peak and Compton continuum is 2 %. For the nitrogen peak at 6.3 MeV,where the detector artefacts are superimposed by other full energy peaks, the ratio of the left over single escape to full energy peak in the response corrected spectrum is 2 %.
Subsequently to the background, response and efficiency corrections of the measured ^{77}Se(n,γ) and ^{195}Pt(n,γ) spectra, these gamma spectra were simulated using the algorithm described in section (4.1) with a few modifications. From other cold neutron capture experiments, the primary transition probabilities of the initially excited state to the first low lying states are known and can be found in [PGA, 2011]. Including these probabilities, simulations of neutron capture gamma ray spectra were performed with different level densities and strength functions to study their influence on the spectral shape.

4.2.1 Analysis of Neutron Capture on Selenium-77

Figure (4.5) shows the background, response and efficiency corrected measured ^{77}Se(n,γ) spectrum. In the spectrum with the original 0.77 keV binning (top subfigure), the primary gamma transitions from the initially excited 1^- state close to

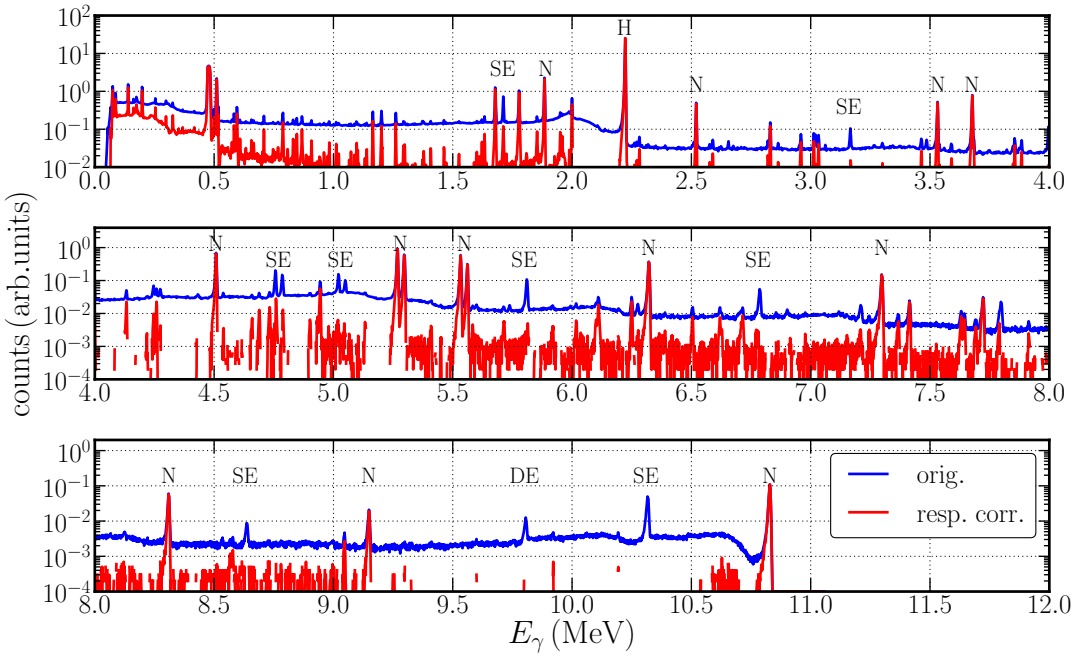

Figure 4.4: Measured (blue) and response corrected (red) neutron capture gamma spectrum on deuterised urea. The marked peaks result from neutron capture on hydrogen (H), nitrogen (N), single escape (SE) and double escape (DE).

S_n to the ground state (0) and the first excited states (1,2,3,7,10) are visible. The properties of these first excited states are listed in table (A.5) in the appendix. The low-energy region of the spectrum is dominated by transitions of the first excited states to the ground state ($2 \rightarrow 0$, $1 \rightarrow 0$). Most interesting for a comparison with a statistical simulation is the intermediate (continuum) region which contains many weak unresolved transitions. For the sake of better statistics and averaging over several transitions, the spectrum was rebinned to 200 keV (bottom subfigure). In the rebinned spectrum, a decreasing slope of the continuum region between 2.4 MeV and 7.8 MeV is clearly visible. Additionally to the smooth shape of the continuum region, a local enhanced gamma yield at around 6.3 MeV can be seen. In the further analysis the shape of the continuum region will be used for a comparison with different simulated spectra.

For the simulation of the measured spectra the algorithm described in section (4.2) was used. The standard input parameters for the simulation of ^{77}Se(n,γ) are listed in table (A.3). The resulting simulated spectra are shown in figure (4.6).
The histogram of all gamma rays emitted during 100000 excitations, presented in the top subfigure of (4.6), shows that the general shape of the measured spectrum is nicely reproduced. Especially the decreasing slope of the continuum region between 2.4 MeV and 6 MeV is clearly visible. A more detailed view on the simulated spectrum is shown in the bottom subfigure where histograms of all simulated gamma rays are shown in different colours corresponding to their order in the deexcitation cascade. Obviously, the continuum region between 2.4 MeV and 6 MeV is a com-

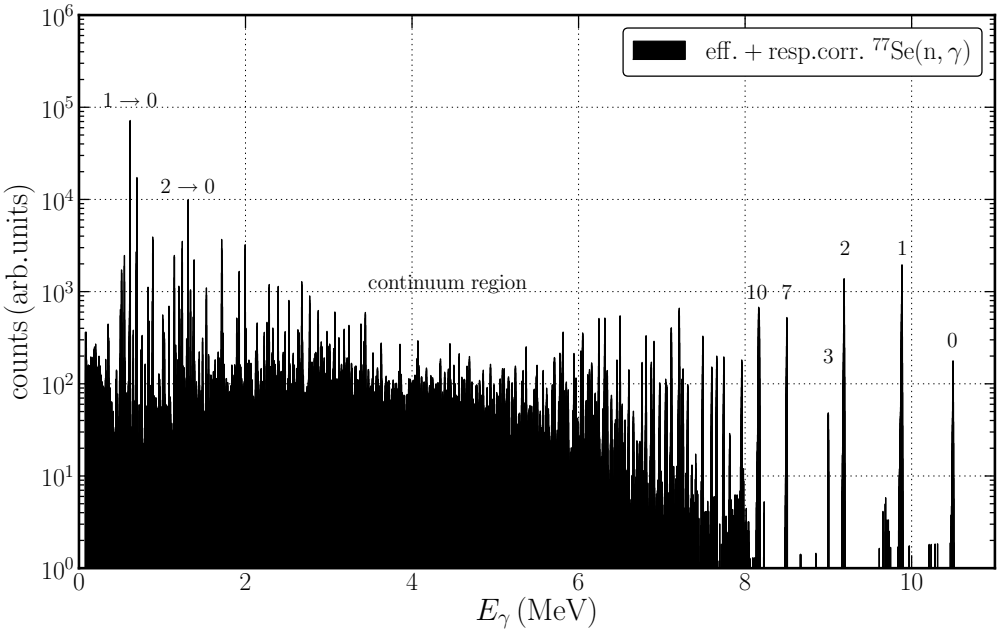

(a) ^{77}Se(n,γ) spectrum with the experimental 0.77 keV binning. In the high-energy region the primary gamma transitions to the ground state (0) and the first excited states (1,2,3,7,10) are visible. In the low-energy region the strongest peaks result from ground state transitions of the 1st (613 keV) and 2nd excited state (1309 keV). The intermediate region consists of distinct peaks and a continuum of weak unresolved transitions.

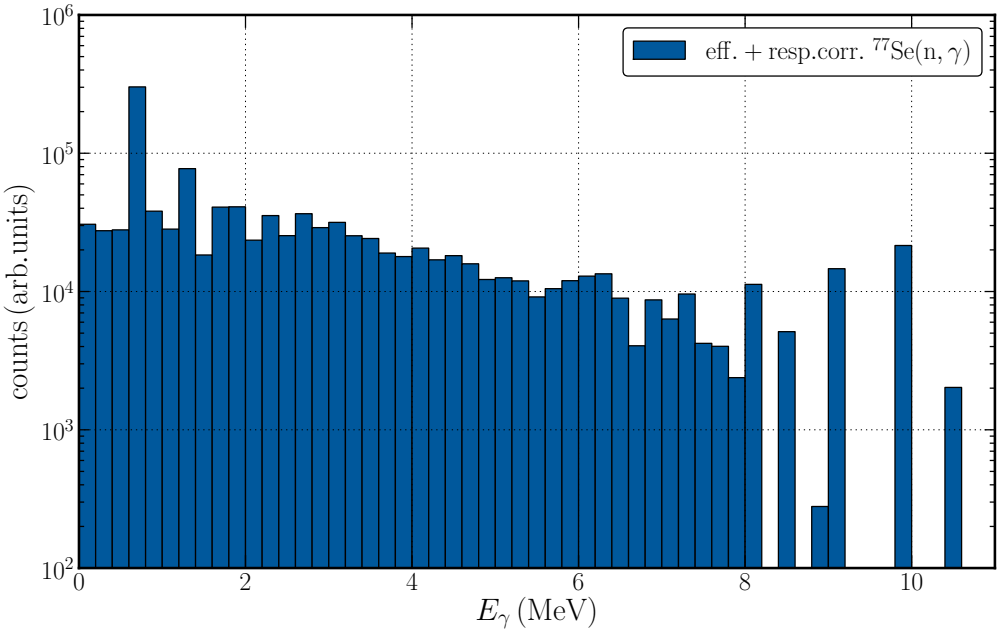

(b) Rebinned spectrum with 200 keV binning. The rebinning averages fluctuations and resolves the shape of the continuum region.

Figure 4.5: Background, response and efficiency corrected experimental ^{77}Se(n,γ) spectrum

position of primary, secondary and third order gamma rays. The contribution of higher-order gamma rays to the continuum increases with decreasing gamma energy. The origins of gamma rays measured in this region can be very different. For example a gamma ray at 4 MeV can result from a primary transition from the initial state at 10.5 MeV to state at 6.5 MeV or from a secondary transition from a state at 7 MeV to a state at 3 MeV, or even from a third order transition from a state at 6 MeV to a state at 2 MeV. This great number of possibilities assures that fluctuations in the single transition widths between two distinct states are averaged out and that the use of the statistical approach for the simulation of this region is valid. In order to understand the influence of the level density on the neutron capture gamma ray spectrum, simulations with different input level densities were performed. Since the normalised average spectral distribution of emitted primary gammas is only dependent on the slope of the level density, simulations using the Constant Temperature Model (CTM) with different temperatures (see figure (4.9)) were performed. The results of these simulations are presented in figure (4.7).

Each subfigure of figure (4.7) shows a comparison between the experimental spectrum (black hatched bars) and the simulated one (filled bars). Moreover the average gamma multiplicity and the reduced chi square for the goodness of fit in the continuum region ($2\,\mathrm{MeV} \leq E \leq 5.4\,\mathrm{MeV}$) are given. In all cases the TLO model was used as $E1$ strength and the parametrisation discussed in section (2.5.2) was used as $M1$ strength. It is visible that the simulated spectrum with $T = 900\,\mathrm{keV}$ fits best to the experimental measured data in the continuum region. This value for the temperature is slightly higher than the one given in [Koning et al., 2008] ($T_\mathrm{K} = 850\,\mathrm{keV}$). However none of the simulations using a monotonically increasing $E1$ strength function is able to describe the measured enhanced gamma yield at energies around 6.3 MeV.

Due to this disagreement, the influence of the shape of the $E1$ gamma strength function on the simulated spectrum, was also investigated in several simulations with different models which are shown in figure (4.9). Simulated spectra using a constant $E1$ strength function, a TLO $E1$ strength function and a composed $E1$ strength function of TLO and an extra Gaussian resonance at 6.3 MeV are shown in figure (4.8). For all these simulations the same CTM level density with $T = 850\,\mathrm{keV}$ and $D_0 = 121\,\mathrm{eV}$ was used.
Again, the gamma multiplicity and a reduced chi square for the goodness of fit in the continuum region ($2\,\mathrm{MeV} \leq E \leq 6.4\,\mathrm{MeV}$) are given for each simulation. All simulations result in the same gamma ray multiplicity $m = 3.6 \pm 0.1$ which can be used for the calculation of the total capture cross section. The first simulations with two monotonously increasing strength functions (linear and TLO model) give poor fits in the region of the enhanced yield at 6.3 MeV. However, adding an Gaussian resonance at this energy with a standard deviation of 200 keV and an amplitude of $2.96 \cdot 10^{-17}\,\mathrm{keV}^{-3}$ to the TLO $E1$ strength results in a good agreement between simulated and experimental measured spectrum. Hence, the enhanced yield at 6.3 MeV could be a hint for a resonance like structure in the gamma strength function. Unfortunately, no quantitative information about the absolute value of the photon strength function can be drawn from these comparisons.

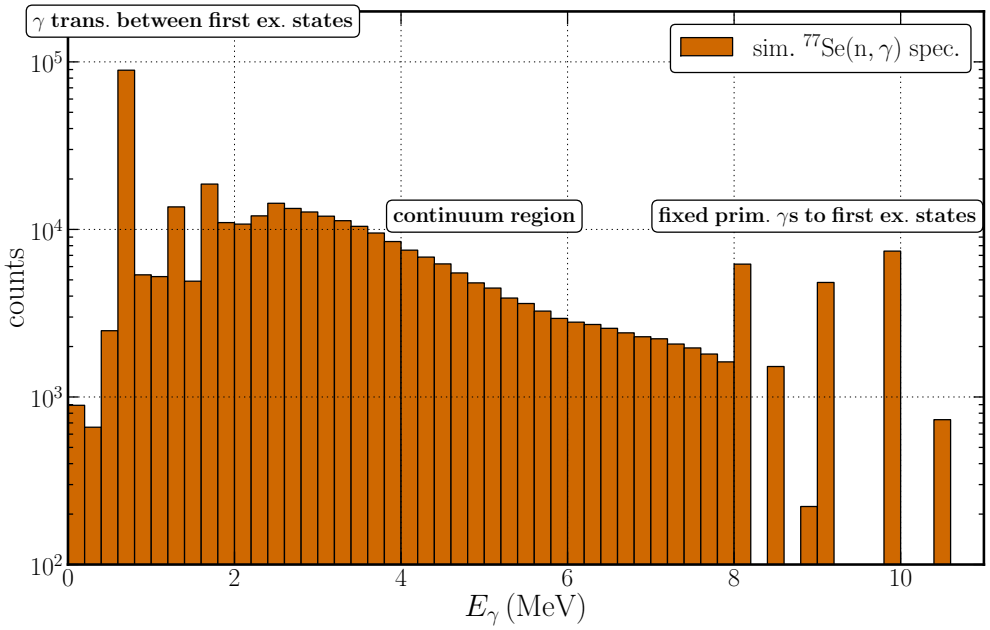

(a) All simulated gamma transitions that occurred during 100000 cascade deexcitations of an excited 1^- state at $S_n = 10.5\,\text{MeV}$. The intensities of the high-energy primary gamma transitions are adjusted to experimental data taken from [PGA, 2011].

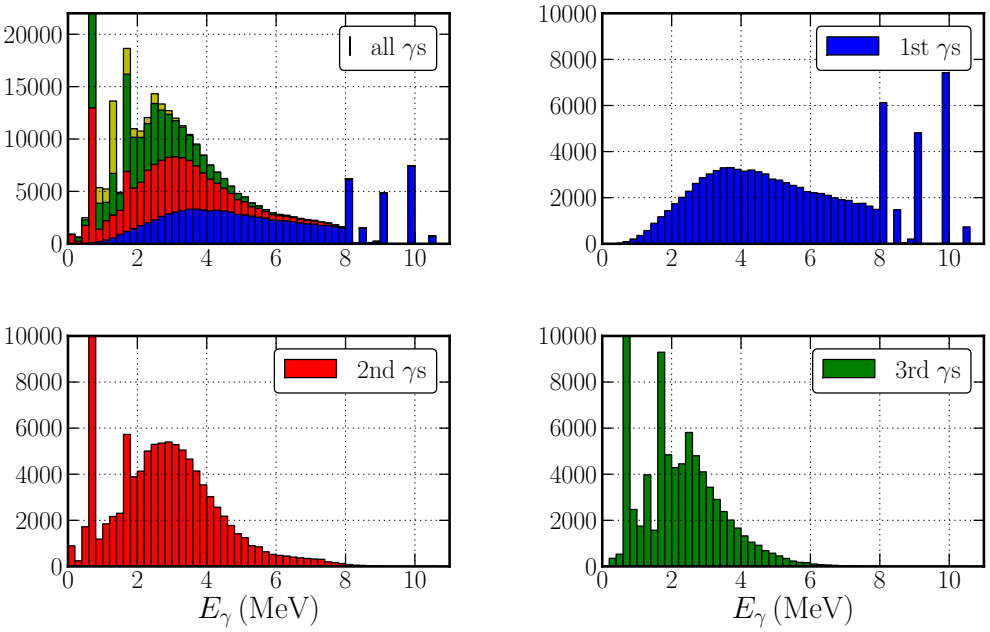

(b) Detailed view on the simulated spectrum. Primary (blue), secondary (red), third order (green) and higher-order (yellow) transitions are shown separately. The high-energy region is dominated by primary transitions, whereas the continuum region also consists of secondary and third order transitions.

Figure 4.6: Simulated ^{77}Se(n,γ) spectra. The used input parameters are listed in table (A.3) in the appendix.

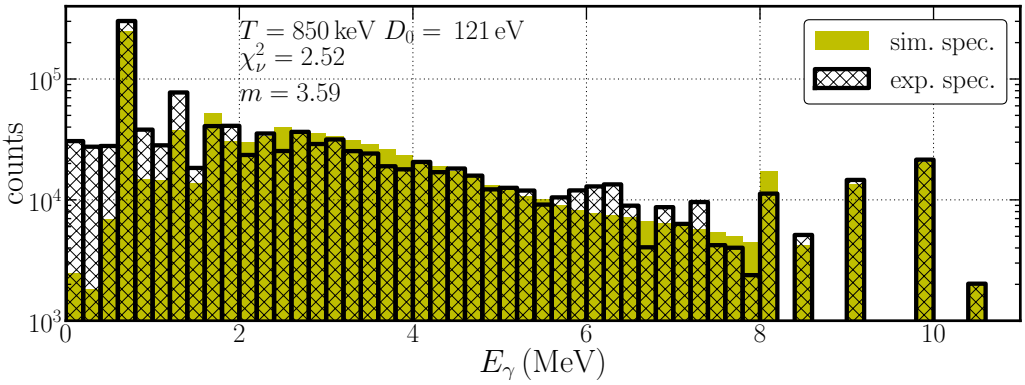

(a) Simulation with $T = 850\,\mathrm{keV}$

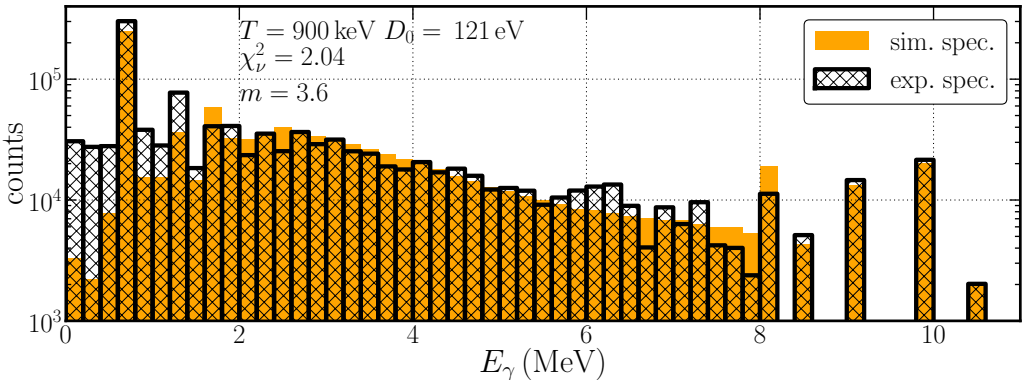

(b) Simulation with $T = 900\,\mathrm{keV}$

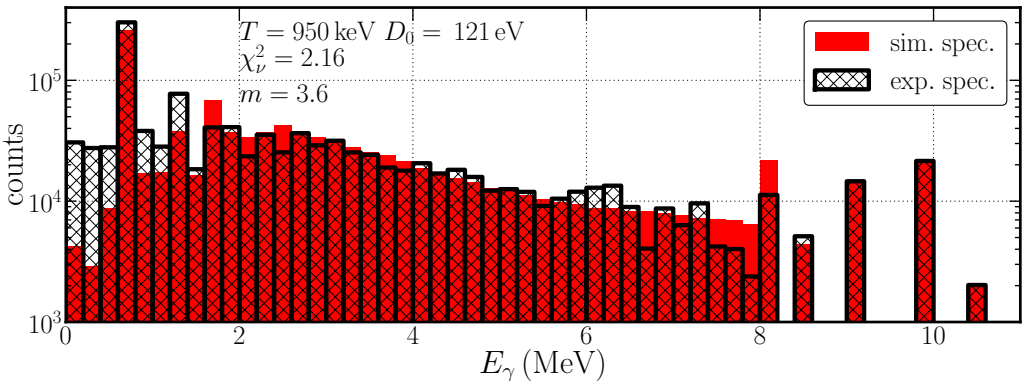

(c) Simulation with $T = 950\,\mathrm{keV}$

Figure 4.7: Simulated ^{77}Se(n,γ) spectra with different temperatures T of the input CTM level density (see figure (4.9)). The simulated spectra (filled bars) containing 100000 iterations are normalised to the experimental yield (black hatched bars) in the highest bin. For each simulation the gamma multiplicity (m) and the reduced chi square for the goodness of fit in the continuum region ($2\,\mathrm{MeV} \leq E_\gamma \leq 5.4\,\mathrm{MeV}$) are given. The deviation in the bin at 8 MeV is a binning artefact.

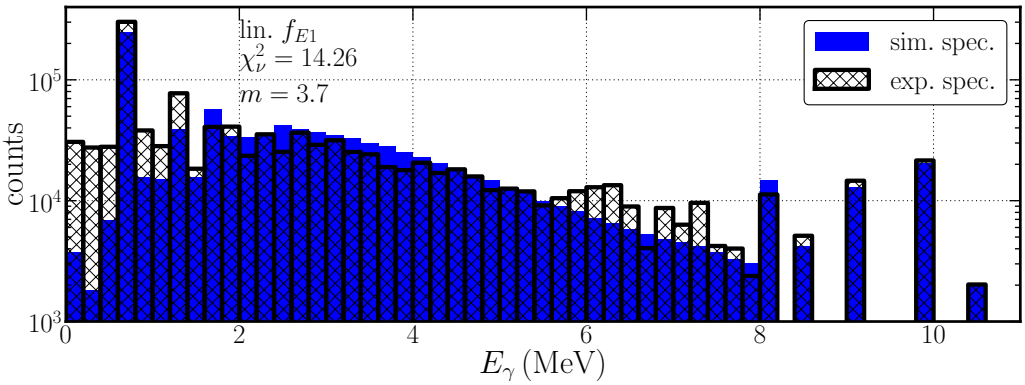

(a) Simulation with a linear $E1$ strength function

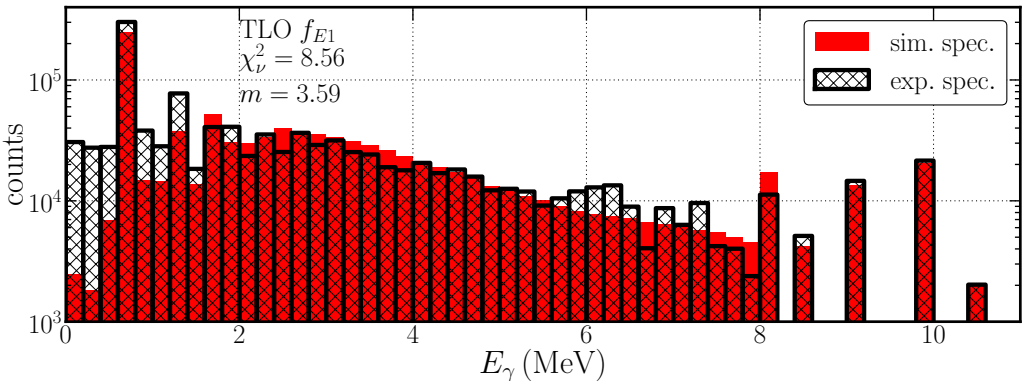

(b) Simulation with TLO $E1$ strength function

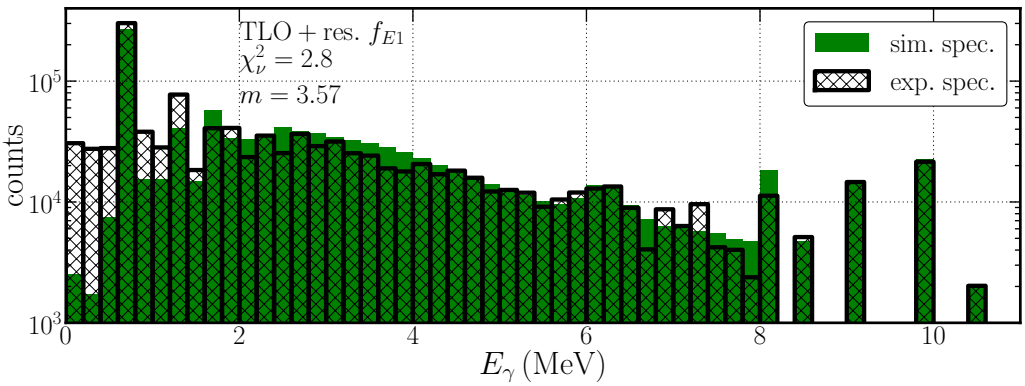

(c) Simulation with $E1$ strength function consisting of TLO and Gaussian resonance at 6300 keV with $\sigma = 200$keV and an amplitude $A = 2.96 \cdot 10^{-17}\,\mathrm{keV}^{-3}$

Figure 4.8: Comparisons of experimental measured spectrum (black) with simulated ones (red) using different input $E1$ strength functions (see figure (4.9)). For each simulation the gamma multiplicity (m) and the reduced chi square for the goodness of fit in the continuum region ($2\,\mathrm{MeV} \leq E \leq 6.4\,\mathrm{MeV}$) are given. It is visible that a resonance like structure in the $E1$ strength is able to describe the enhanced measured gamma yield in the region at 6.3 MeV.

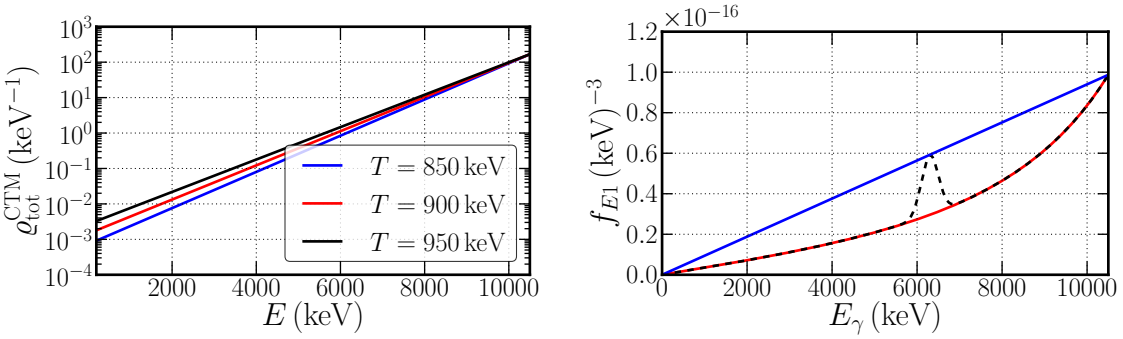

(a) CTM level density for different temperatures. The absolute value at the neutron separation energy is kept constant.

(b) Energy dependence of linear (blue), TLO (red) and TLO plus additional Gaussian resonance at 6300 keV (black dashed) $E1$ strength functions.

Figure 4.9: Different input CTM level densities and $E1$ strength functions for the simulation of ^{77}Se(n,γ)

4.2.2 Analysis of Neutron Capture on Platinum-195

For the analysis of ^{195}Pt(n,γ) the same approach as in the case of ^{77}Se(n,γ) was used. The measured efficiency and response corrected gamma spectrum is presented in figure (4.10). In the top subfigure, the high-energy primary gammas and the continuum region are obvious. Moreover many strong gamma lines can be found in the region between 5 MeV and 6 MeV. This is visible in the bottom subfigure as well, where the spectrum rebinned to 200 keV is shown. In comparison to ^{77}Se(n,γ) the ratio of the high lying primary gammas to the continuum region is much smaller, which can be explained with the higher level density of ^{196}Pt compared to ^{78}Se.

As in the previous analysis, simulations with a TLO $E1$ and a $M1$ strength function discussed in section (2.5.2) and different temperatures T were made and are shown in figure (4.11). The standard input parameters for the simulation of ^{195}Pt(n,γ) and the properties of the used first excited states are listed in tables (A.4) and (A.5) in the appendix. For the goodness of fit between simulated and experimental spectrum, the reduced chi square in the energy region $1.4\,\mathrm{MeV} \leq E \leq 4.4\,\mathrm{MeV}$ was calculated. Apparently, the simulation using $T = 650\,\mathrm{keV}$ fits the data best. Again this value is higher than the one given in [Koning et al., 2008] ($T_{\mathrm{K}} = 553\,\mathrm{keV}$). As in the case of ^{77}Se(n,γ) none of the simulations with a monotonically increasing $E1$ strength function is able to describe the enhanced measured gamma yield in the region around 5.4 MeV. Compared to ^{77}Se(n,γ), all simulations of ^{195}Pt(n,γ) give a higher gamma ray multiplicity of $m = 4.1 \pm 0.1$ which can be explained with the greater number of excited states up to S_{n}.

As discussed in [Bartholomew et al., 1973], the origin of the enhanced gamma yield at around 5.4 MeV in heavy nuclei can not be a local enhancement of the level density. It could be shown that the center of gravity of this bump does not change when varying the incident neutron energy (capture on higher lying resonances). Moreover, from comparisons of s-wave and p-wave neutron capture gamma spectra,

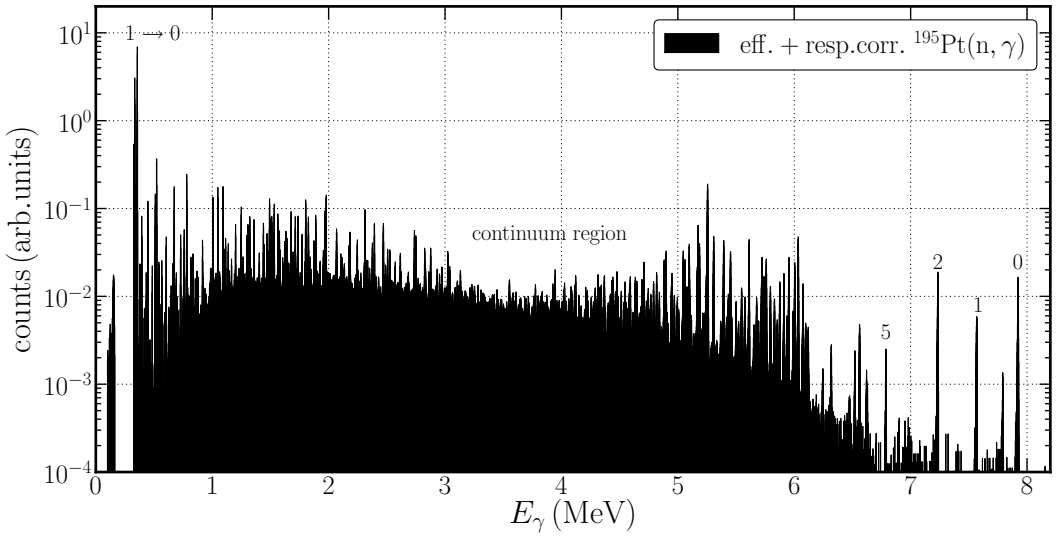

(a) ^{195}Pt(n,γ) spectrum with experimental 0.77 keV binning. In the high-energy region the primary gamma transitions to the ground state (0) and the first excited states (1,2,5) are visible. In the low-energy region the strongest line results from ground state transitions of the 1st excited state. The intermediate region consists of distinct lines and a continuum of weak unresolved transitions. In the region between 5 MeV and 6 MeV an enhanced number of strong transitions is visible. The neutron separation energy of ^{196}Pt is 7.92 MeV [Xiaolong, 2007]

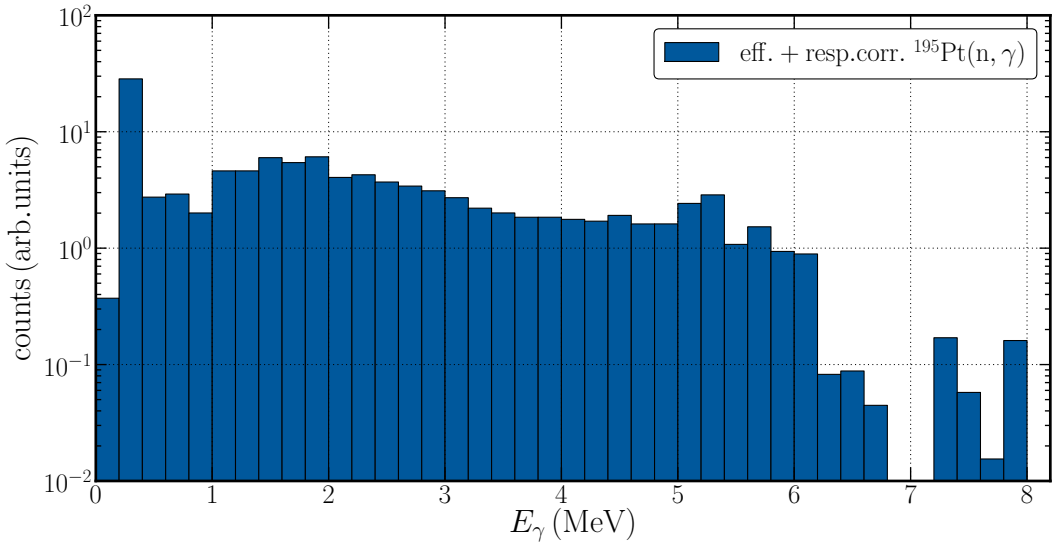

(b) Rebinned spectrum with 200 keV binning. The rebinning averages fluctuations and resolves the shape of the continuum region. In the region between 5 MeV and 6 MeV a strongly enhanced yield is obvious.

Figure 4.10: Background, response and efficiency corrected experimental ^{195}Pt(n,γ) spectrum

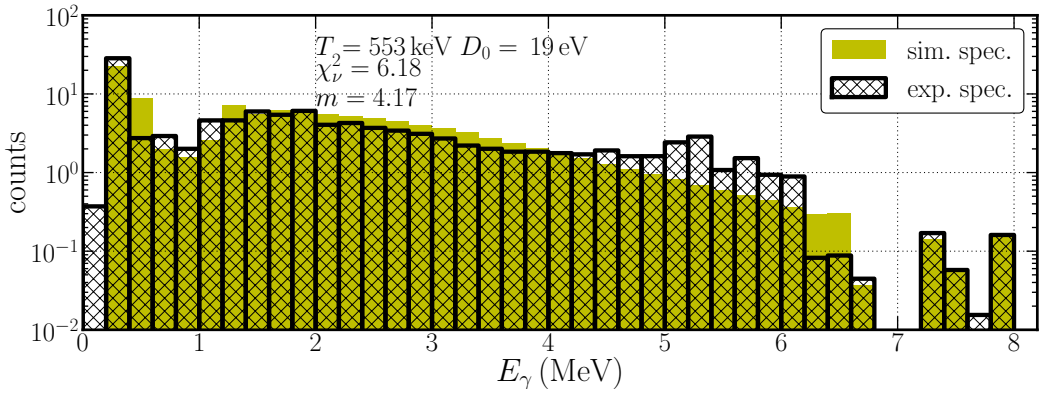

(a) Simulation with $T = 553\,\mathrm{keV}$

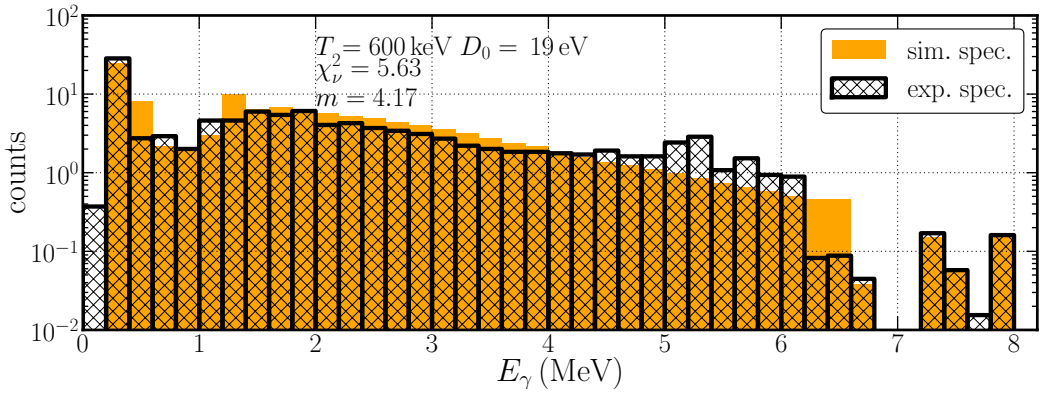

(b) Simulation with $T = 600\,\mathrm{keV}$

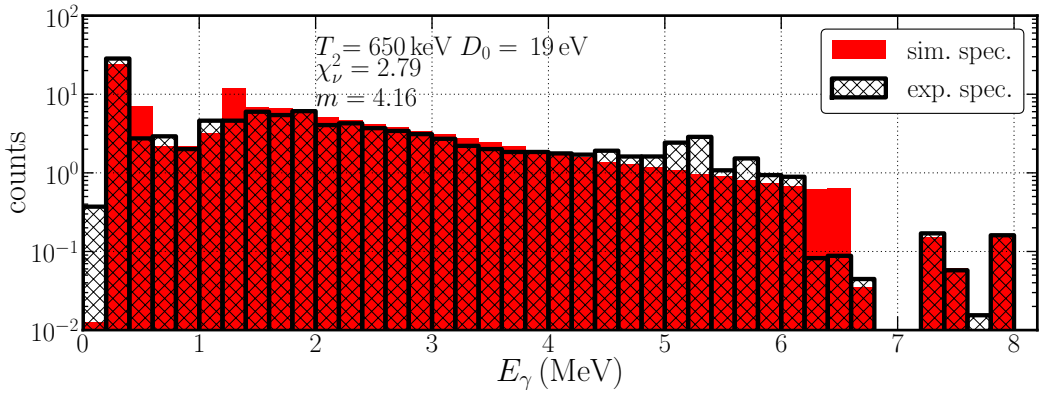

(c) Simulation with $T = 650\,\mathrm{keV}$

Figure 4.11: Simulated ^{195}Pt(n,γ) spectra with different temperatures T for the input CTM level density (see figure (4.9)). The simulated spectra (filled bars) containing 100000 iterations are normalised to experimental yield (black hatched bars) in the highest bin. For each simulation the gamma multiplicity (m) and the reduced chi square for the goodness of fit in the continuum region ($1.4\,\mathrm{MeV} \leq E_\gamma \leq 4.4\,\mathrm{MeV}$) are given.

it could be deduced that this extra yield are $E1$ transitions.
In order to describe the 5.4 MeV extra yield, simulations with a modified $E1$ strength function consisting of the TLO model and a Gaussian resonance at 5.4 MeV have been performed (see figure 4.13). The results of these simulations are shown in figure (4.12). Obviously, simulations with an additional Gaussian resonance in the $E1$ strength function are able to reproduce the enhanced gamma yield at 5.4 MeV. In order to fit the width and height of the extra bump, a resonance with an amplitude of $A \approx 1.88 \cdot 10^{-16}\,\mathrm{keV}^{-3}$ and a width of $\sigma = 0.25\,\mathrm{MeV}$ is necessary. Compared to the area of the TLO $E1$ strength function up to S_n this corresponds to an extra strength of 17%.

Conclusions

1. The comparisons of simulated and experimental neutron capture gamma ray spectra show that the developed simulation code for a statistical description of radiative deexcitations in excited nuclei works.

2. By comparison of simulated and experimental continuum regions in the spectra, a temperature for the Constant Temperature level density of the compound nuclei of $T = 900\,\mathrm{keV}$ for ^{78}Se and $T = 650\,\mathrm{keV}$ for ^{196}Pt could be estimated.

3. Enhanced gamma yields at 6.3 MeV in ^{77}Se(n,γ) and 5.4 MeV in ^{195}Pt(n,γ) are hints for extra $E1$ photon strength.

4. The gamma ray multiplicity for ^{77}Se(n,γ) $m = 3.6 \pm 0.1$ and for ^{195}Pt(n,γ) $m = 4.1 \pm 0.1$ could be determined.

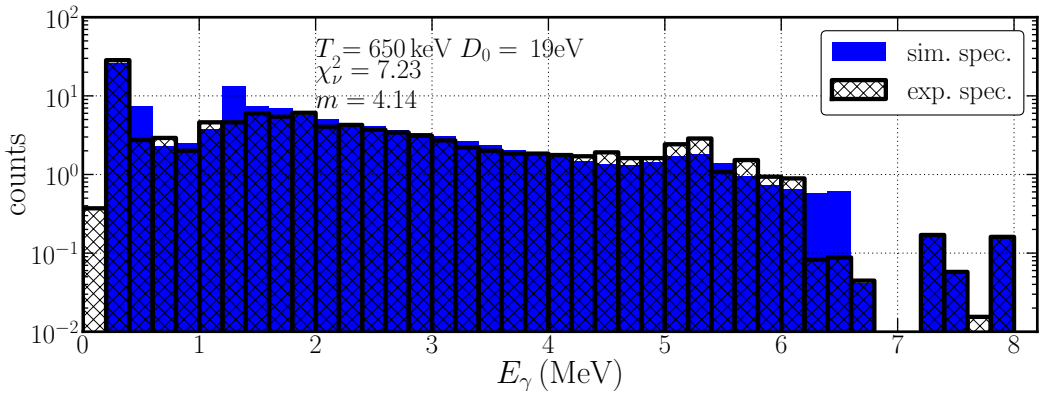

(a) $A = 1.18 \cdot 10^{-16}\,\mathrm{keV}^{-3}$, $E_r = 5.4\,\mathrm{MeV}$, $\sigma = 0.25\,\mathrm{MeV}$

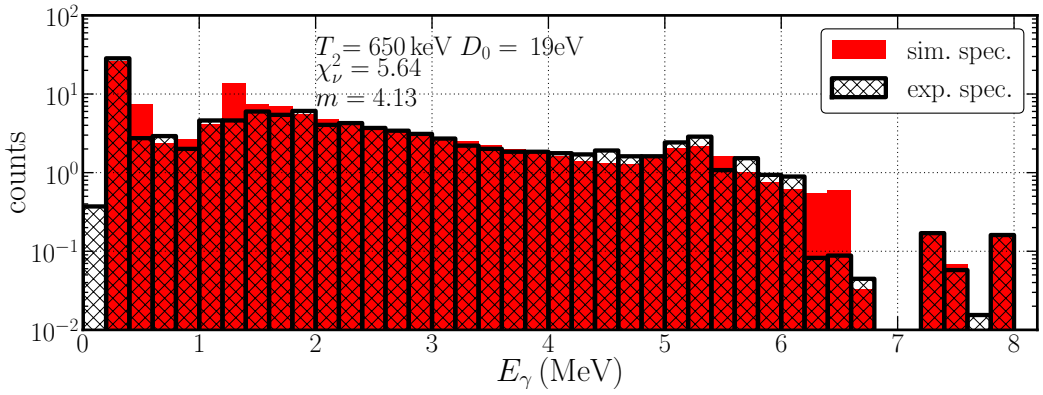

(b) $A = 1.88 \cdot 10^{-16}\,\mathrm{keV}^{-3}$, $E_r = 5.4\,\mathrm{MeV}$, $\sigma = 0.25\,\mathrm{MeV}$

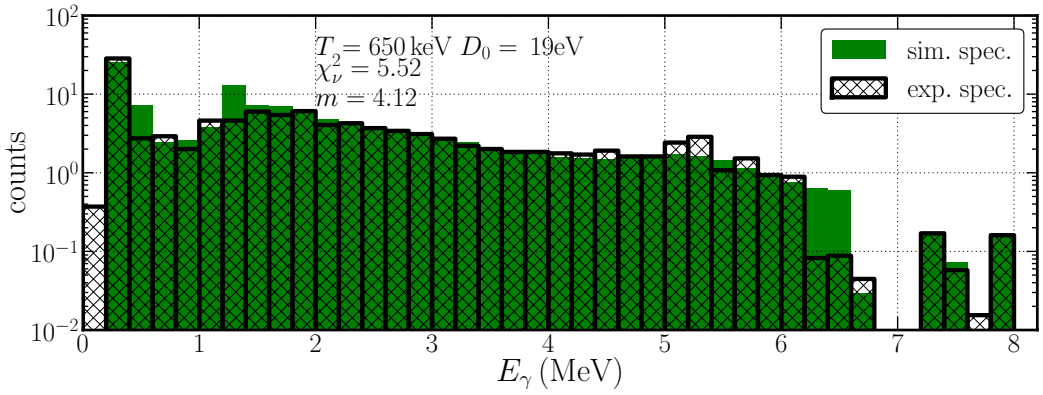

(c) $A = 2.34 \cdot 10^{-16}\,\mathrm{keV}^{-3}$, $E_r = 5.5\,\mathrm{MeV}$, $\sigma = 0.5\,\mathrm{MeV}$

Figure 4.12: Simulations of ^{195}Pt(n,γ) with a modified $E1$ strength function consisting of the TLO model plus an additional Gaussian resonance with amplitude A, mean E_r and standard deviation σ (see figure (4.13)). For all cases, a CTM level density with $T = 650\,\mathrm{keV}$ and $D_0 = 19.2\,\mathrm{eV}$ was used. For each simulation the gamma multiplicity (m) and the reduced chi square for the goodness of fit in the continuum region ($1.4\,\mathrm{MeV} \leq E_\gamma \leq 6.0\,\mathrm{MeV}$) are given.

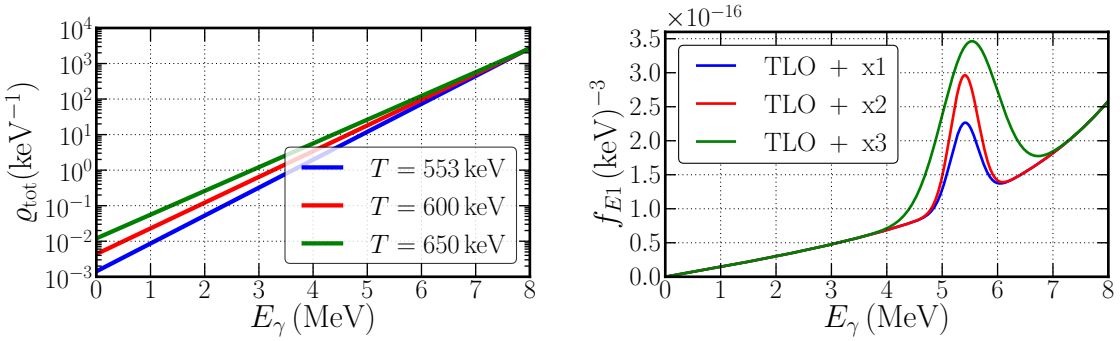

(a) CTM level density for different temperatures. The absolute value at the neutron separation energy is kept constant.

(b) Modified $E1$ strength functions consisting of TLO model and a Gaussian resonance. The parameters of the curves are given in table (A.2) in the appendix.

Figure 4.13: Different input CTM level densities and $E1$ strength functions for the simulation of ^{195}Pt(n,γ)

4.3 Analysis of Photon Scattering Experiments

In this section the different steps in the analysis of the two photon scattering experiments on ^{78}Se and ^{196}Pt are presented. The first two of these steps, the deconvolution of the measured spectra for detector response and efficiency and the subtraction of non-nuclear background was done by [Massarczyk, 2011] using GEANT4 simulations of the experimental setup. In this work, the remaining steps, the determination of the incident bremsstrahlung fluence and the correction for inelastically scattered events and branching will be presented.

4.3.1 Analysis of Photon Scattering from Selenium-78

Determination of the Bremsstrahlung Fluence

For the determination of the incident bremsstrahlung fluence, photon scattering from a ^{11}B calibration target is used. ^{11}B has only few excited states up to 9 MeV with known branching ratios and integrated elastic scattering cross sections. These quantities are listed in table (A.1) in the appendix.

The number of photons Y_{abs} absorbed by a resonance in a thin target irradiated by a homogeneous photon fluence distribution is given by:

$$Y_{\mathrm{abs}} = N_{\mathrm{T}} \cdot \int_{\mathrm{res}} \sigma(E)\Phi_E(E)dE \tag{4.3}$$

Here, N_{T} is the number of target atoms in the beam, $\sigma(E)$ is the cross section for absorption into a resonance and $\Phi_E(E)$ is the spectral photon fluence (the number of photons per unit energy and unit area perpendicular to the beam). Assuming that the impinging spectral photon fluence is constant over the narrow resonance one obtains:

$$\Phi_E(E_{\mathrm{res}}) = \frac{Y_{\mathrm{abs}}}{N_{\mathrm{T}} \cdot I_{\mathrm{abs}}} \tag{4.4}$$

Here I_{abs} is the energy integrated cross section for absorption in a resonance. In the experiment, the number of elastically scattered photons Y_{scat} is measured which is given by:

$$Y_{\mathrm{scat}} = Y_{\mathrm{abs}} \cdot B_0 \cdot \varepsilon(E_{\mathrm{res}}) \cdot W \tag{4.5}$$

where B_0 is the ground state branching ratio of the resonance, W is an angular correlation factor and ε is the detector efficiency.
It has to be taken into account that the resonances at 2124 keV, 4444 keV, 5020 keV are fed from excited states at higher energies. The number of absorbed photons is obtained by subtracting the amount of feeding transitions from the measured number of detected transitions using the branching ratios given in table (A.6) in the appendix. Finally one obtains for the feeding-corrected number of absorbed photons in the resonances:

$$\begin{aligned}
Y_{\mathrm{abs,8920}} &= \frac{Y_{\mathrm{scat,8920}}}{0.973 \cdot \varepsilon_{8920} \cdot W_{8920}} \\
Y_{\mathrm{abs,7285}} &= \frac{Y_{\mathrm{scat,7285}}}{0.884 \cdot \varepsilon_{7285} \cdot W_{7285}} \\
Y_{\mathrm{abs,5020}} &= \frac{Y_{\mathrm{scat,5020}}}{0.858 \cdot \varepsilon_{5020} \cdot W_{5020}} - 0.06\, Y_{\mathrm{abs,7285}} \\
Y_{\mathrm{abs,4444}} &= \frac{Y_{\mathrm{scat,4444}}}{1.000 \cdot \varepsilon_{4444} \cdot W_{4444}} - 0.03\, Y_{\mathrm{abs,8920}} - 0.06\, Y_{\mathrm{abs,7285}} \\
Y_{\mathrm{abs,2124}} &= \frac{Y_{\mathrm{scat,2124}}}{1.000 \cdot \varepsilon_{2124} \cdot W_{2124}} - 0.14\, Y_{\mathrm{abs,5020}}
\end{aligned}$$

In order to describe the shape of the incident photon fluence for a given endpoint energy a two dimensional interpolation of the values given in [Seltzer and Berger, 1986] for a thin niobium radiator multiplied with a simulated function that takes the influence of the aluminium hardener into account is used. The hardener function was simulated with GEANT4 by Ralph Massarczyk and is shown in figure (A.1) in the appendix. The fluence values deduced from fits to the measured yield of elastically scattered photons on the ^{11}B resonances are given in table (4.1). Moreover the calculated photon fluence distribution from the Seltzer and Berger values for an incident kinetic electron endpoint energy of $E_{\mathrm{end}} = 11.5\,\mathrm{MeV}$ is shown in figure (4.14). The value of the kinetic electron endpoint energy was determined by analysing proton spectra from deuteron breakup [Schwengner et al., 2005].
It is visible in figure (4.14) that the fluence deduced from the 7285 keV resonance is too high and has a large uncertainty. In the measured spectrum this peak has a non-Gaussian distribution indicating an unresolved contribution from another transition. The uncertainty in the deduced fluence distribution has two contributions. These are on the one hand the normalisation uncertainty which is 7.4% resulting from the statistical error of the fitted peak area and an estimated 5% uncertainty of the efficiency and on the other hand a 200 keV uncertainty of the endpoint energy.

E_{res} (keV)	Y_{scat}	Y_{abs}	Φ_E ($\mathrm{eV}^{-1}\mathrm{b}^{-1}$)
8920	7954(228)	$5.1(3)\cdot 10^7$	$1.46(11)\cdot 10^{-17}$
7285	9083(4083)	$4.9(22)\cdot 10^7$	$3.9(18)\cdot 10^{-17}$
5020	29040(6766)	$10.6(26)\cdot 10^7$	$3.6(9)\cdot 10^{-17}$
4444	31112(728)	$8.6(5)\cdot 10^7$	$4.5(3)\cdot 10^{-17}$
2124	39065(723)	$5.4(5)\cdot 10^7$	$9.1(11)\cdot 10^{-17}$

Table 4.1: Spectral bremsstrahlung fluence deduced from fits to the measured gamma yield of elastically scattered photons on ^{11}B resonances in the ^{78}Se(γ,γ) experiment. Y_{scat} are the number of measured elastic scattered photons on a resonance at E_{res}. Y_{abs} are the calculated numbers of absorbed photons in the resonance and Φ_E is the spectral bremsstrahlung fluence. The calculated fluence at 8.9 MeV corresponds to a flux of approximately $10^7\,\mathrm{MeV}^{-1}\mathrm{cm}^{-2}\mathrm{s}^{-1}$ typically for this bremsstrahlung setup.

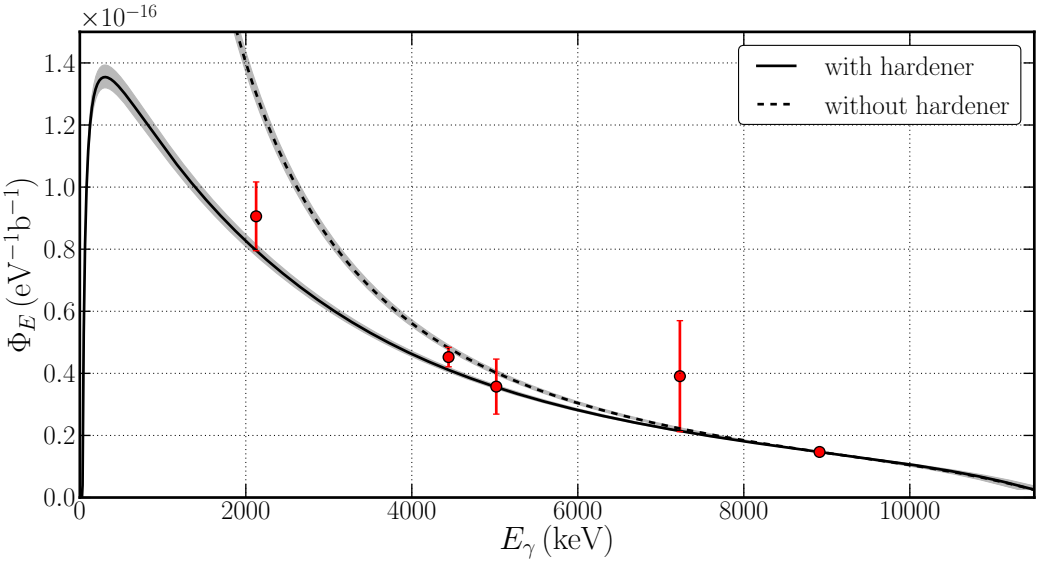

Figure 4.14: Spectral bremsstrahlung fluence of the ^{78}Se(γ,γ) experiment. The red circles correspond to the fluence determined from measured transitions in ^{11}B. The dashed black line is the flux distribution calculated using the Seltzer and Berger Formula. The solid black line takes the influence of the aluminium hardener into account. Both curves are normalised to the fluence deduced from scattering from the 8920 keV resonance. The gray bands correspond to the uncertainty due to a 200 keV uncertainty of the 11500 keV kinetic electron endpoint energy.

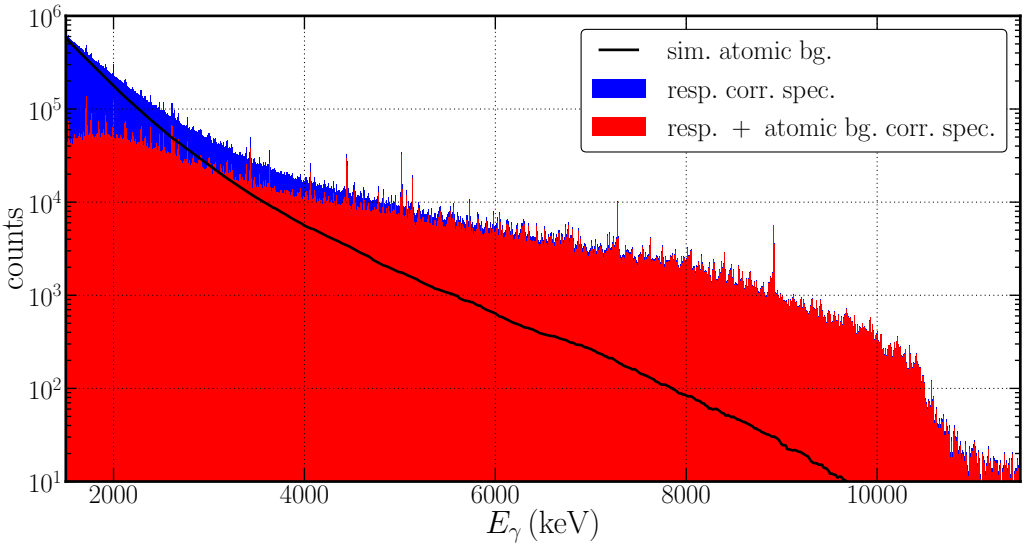

Figure 4.15: Simulation (black) and subtraction (red) of the atomic background from the response corrected measured ^{78}Se(γ,γ) spectrum (blue). The atomic background was simulated with GEANT4 by Ralph Massarczyk.

The latter one is small compared to the first one for energies less than the neutron separation energy of 10.5MeV ($< 5\%$). The total uncertainty of the fluence is estimated to be at maximum 9%.

Correction for Non-Nuclear Scattered Transitions

The non-nuclear background (atomic background) contained in the measured spectrum, resulting from interactions of the impinging photons with electrons in the target was simulated with GEANT4 by [Massarczyk, 2011]. The results of the simulation and the subtraction of the atomic background from the response corrected measured spectrum are shown in figure (4.15). It is clearly visible that the measured spectrum (blue) below 4 MeV is strongly influenced by non-nuclear scattered events (black). Above 4 MeV the ratio of the atomic background to the measured events decreases steadily from 30% to $\approx$ 1% at the neutron threshold of 10.5 MeV. Due to the huge corrections in the low energy region, an analysis of the data is only reasonable above $\approx$ 4 MeV.

Correction for Inelastic Transitions

As discussed in section (2.2), the yield of elastic scattered photons and the ground state branching ratio of an excited state in an energy bin $\left[E - \frac{\Delta E}{2}, E + \frac{\Delta E}{2}\right]$ are needed to calculate the average absorption cross section. The measured gamma spectrum however, contains not only gammas from elastic transitions, but also inelastic transitions that occur in cascade deexcitations. Hence a two step correction of the measured spectrum for inelastic transitions is necessary:

1. Subtraction of all inelastic transitions which yields the spectrum of elastically scattered photons Y_{elas}.

2. Calculation of the absorption spectrum Y_{abs} by division of the spectrum of elastically scattered photons Y_{elas} by the ground state branching ratio B_0.

The simulation code described in section (4.1) is able to calculate the average ground state branching ratio as well as the average yield of inelastic transitions emitted during a deexcitation of an excited state. However, it has to be emphasized again, that photon scattering is a two step process consisting of excitation and deexcitation. Due to fluctuations in the ground state transition widths, not all states in an energy bin are excited equally. Those with a large transition width are excited more often than those with a small one. Subsequently to the excitation, states with a large ground state width will deexcite with a higher probability directly back to the ground than the other states. This effect results in an enhancement of direct ground state transitions in photon scattering experiments and can be calculated with a numerical simulation discussed in section (2.6) to a statistical fluctuation factor S for each excitation energy.
For the correction of inelastic transitions, the average deexcitation spectra for states at different excitation energies were simulated. In the analysis of ^{78}Se(γ,γ) this was done in steps of 200 keV up to the neutron separation energy. The simulated deexcitation spectra for a TLO $E1$ strength function and CTM level density with $T = 900\,\mathrm{keV}$ and $D_0 = 121\,\mathrm{eV}$ are shown in figure (4.16). For each excitation energy the direct ground state transitions and the transitions to the first excited states are visible (diagonal structure). Moreover vertical structures in the low energy region which correspond to transitions between the first excited states can be seen. In the simulation experimentally known states and their branching ratios were used up to 2400 keV.
Figures (4.17) and (4.18) show the simulated statistical fluctuation S factor and the ground state transition probabilities which are the products of the average branching ratio $\langle\Gamma_0\rangle / \langle\Gamma_{\mathrm{tot}}\rangle$ and S for different CTM level densities. Each time a fixed mean resonance spacing at the threshold, an $E1$ TLO strength function and a Porter-Thomas distribution for the fluctuations of the transition width was used. In the top subfigure it is visible that at high energies the branching ratio decreases with increasing temperature for a fixed excitation energy. This is due to the fact, that there are simply more possible final states between the ground state and the excited state for increasing T and a fixed D_0. The statistical fluctuation factor, shown in the bottom subfigure, increases steadily from 1 at low excitation energies where only one resonance lies in the averaging bin. At high excitations energies (above the threshold) it will approach its limiting value of $1 + \frac{2}{\nu}$ for a reduced chi-square distribution with ν degree of freedoms of the transition widths. For the assumed Porter-Thomas distribution ($\nu = 1$) it will approach 3 at high energies. With increasing T which corresponds to an increasing number of states in the averaging bin, S rises faster.
For the correction of the inelastic transitions a step by step subtraction method is used beginning at the bin corresponding to the highest possible excitation energy (S_{n}) in the uncorrected spectrum. The gamma yield in this bin can only result from elastic transitions because all possible inelastic transitions must have smaller energies. For this excitation energy the simulated deexcitation spectrum is normalized to the gamma yield in the bin of the uncorrected spectrum. Subsequently all simulated

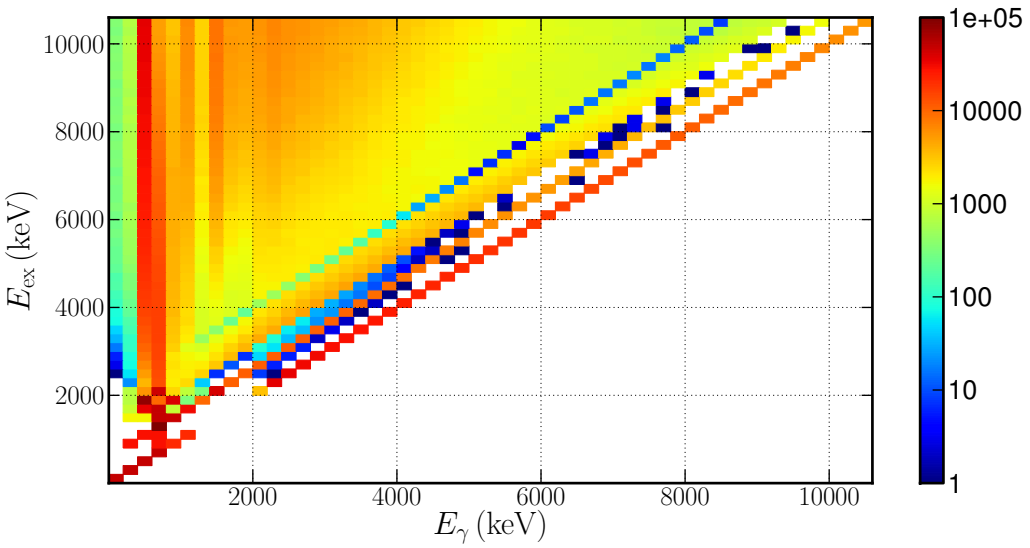

Figure 4.16: Simulated deexcitation spectra for excited 1^- states in ^{78}Se in steps of 200 keV. For each excitation energy 50000 deexcitations were simulated. A CTM level density with $T = 900$ keV and a TLO $E1$ strength function were used as input parameters. Clearly visible are the direct ground state transitions and the transitions to the first excited states (diagonal structures). Moreover the transitions between the first excited states can be seen in the low energy region (vertical structures).

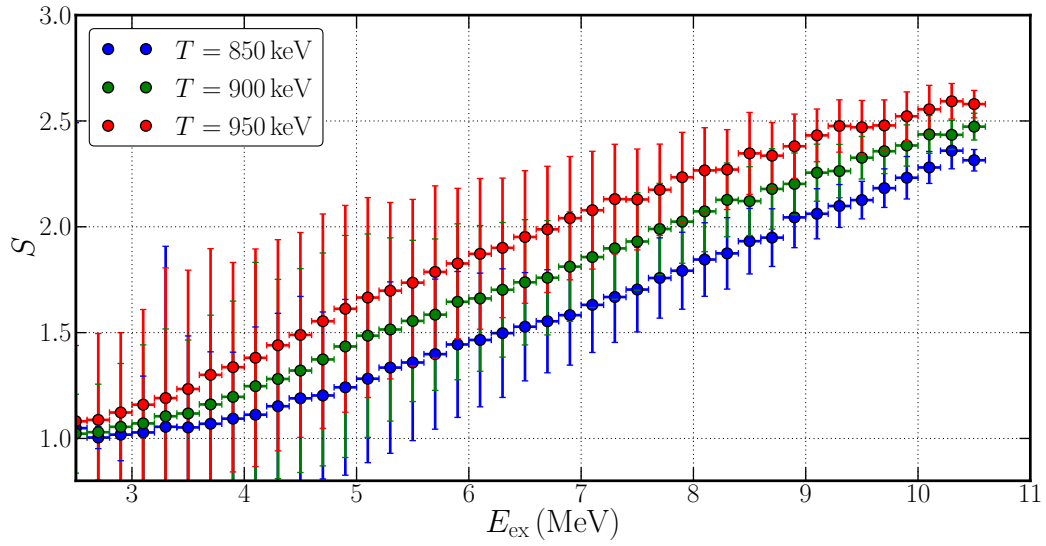

Figure 4.17: Simulated statistical fluctuation factor for ^{78}Se. For the simulations a CTM level density with different temperatures T, but a fixed mean resonance spacing at the threshold $D_0 = 121.0$ eV and an $E1$ TLO strength function were used.

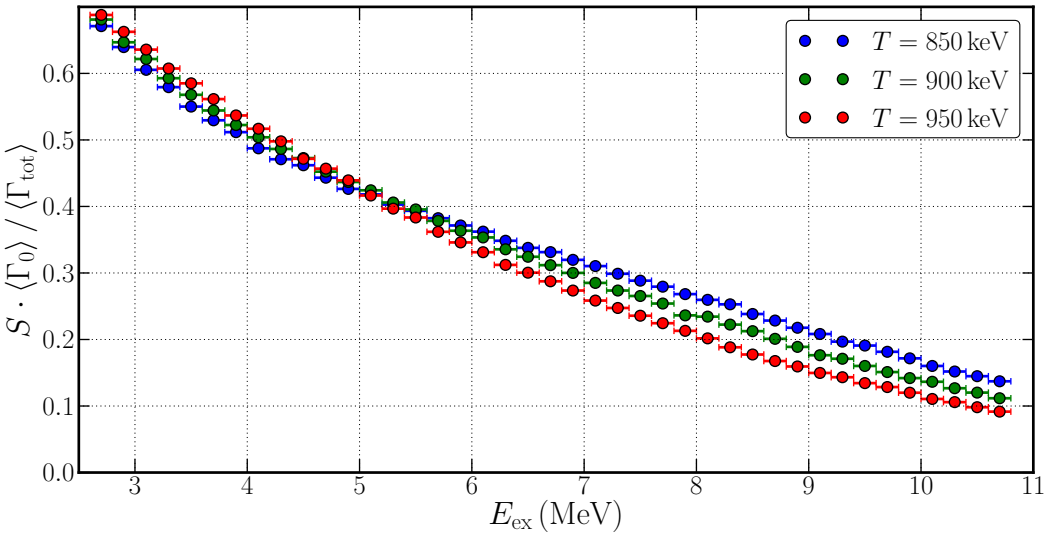

Figure 4.18: Simulated ground state branching ratios enhanced by the statistical enhancement factor for ^{78}Se. For the simulations a CTM level density with different temperatures T, but a fixed mean resonance spacing at the threshold $D_0 = 121.0\,\mathrm{eV}$ and an $E1$ TLO strength function were used.

inelastic transitions are subtracted from the uncorrected spectrum. This procedure is executed on all bins in decreasing order starting at the highest one. Finally, after subtracting all inelastic events from all possible excitation energies, the spectrum should contain only elastic transitions. In the last step of the correction, the elastic spectrum is divided by the simulated ground state transition probability for each excitation energy.
Figure (4.19) shows the two correction steps for the case of ^{78}Se(γ,γ). The spectrum containing all transitions (red), the spectrum without inelastic transitions (blue) and the calculated absorption spectrum (black hatched) are shown. As visible, transitions in the highest bins ($E_\gamma > 9\,\mathrm{MeV}$) are hardly fed by inelastic transitions from above. For those states the division by the ground state transition probability leads to a larger value of absorbed transitions compared to measured transitions. In the intermediate region ($5.5\,\mathrm{MeV} < E_\gamma < 7.5\,\mathrm{MeV}$) the subtraction of inelastic transitions and the correction for ground state branching nearly cancels out which means that the number of measured photons is approximately equal to the number of absorbed photons. In the low-energy region ($E_\gamma < 5.5\,\mathrm{MeV}$) the feeding effect dominates which means that the measured gamma yield is bigger than the number of absorbed photons. However it should be mentioned that the uncertainties rapidly increase towards low excitations energies due to the stepwise subtraction method.

Using the calculated absorption spectrum, and equations (2.14), (2.19) and (4.4) allows to calculate the integrated absorption cross section $I_{\mathrm{abs,T}}$ of the target relative to the integrated absorption cross section $I_{\mathrm{abs,B}}$ of a ^{11}B resonance.

$$\frac{I_{\mathrm{abs,T}}(E,\Delta E)}{I_{\mathrm{abs,B}}(E_{\mathrm{B}})} = \frac{Y_{\mathrm{abs}}(E,\Delta E)}{Y_{\mathrm{abs,B}}(E_{\mathrm{B}})} \cdot \frac{N_{\mathrm{B}}}{N_{\mathrm{T}}} \cdot \frac{\Phi_E(E_{\mathrm{B}})}{\Phi_E(E)} \cdot \frac{W_{\mathrm{B}}}{W_{0\to1\to0}} \tag{4.6}$$

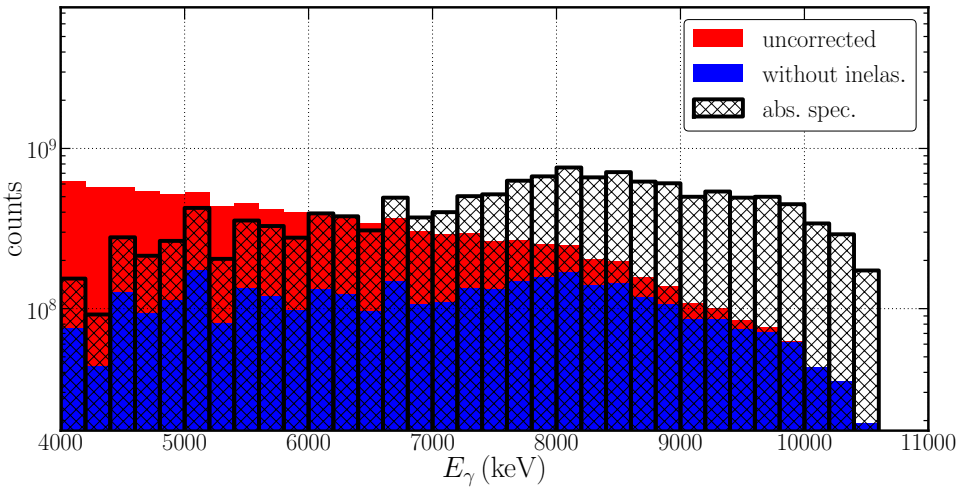

Figure 4.19: Different steps in the correction for inelastic transitions. The response, efficiency and atomic background corrected measured spectrum containing elastic and inelastic transitions (red), the spectrum without inelastic transitions (blue) and the calculated absorption spectrum (black hatched) are shown for ^{78}Se(γ,γ) using the simulated deexcitation spectra shown in figure (4.16).

Inserting the relation between the number of absorbed photons in the target and the measured elastically scattered ones in the detector yields:

$$\frac{I_{\mathrm{abs,T}}(E,\Delta E)}{I_{\mathrm{abs,B}}(E_\mathrm{B})} = \frac{Y_{\mathrm{scat}}(E,\Delta E)}{\varepsilon(E)B(E)S(E)} \cdot \frac{\varepsilon(E_\mathrm{B})B(E_\mathrm{B})}{Y_{\mathrm{scat,B}}(E_\mathrm{B})} \frac{N_\mathrm{B}}{N_\mathrm{T}} \cdot \frac{\Phi_E(E_\mathrm{B})}{\Phi_E(E)} \cdot \frac{W_\mathrm{B}}{W_{0\to1\to0}} \tag{4.7}$$

In equations (4.6) and (4.7) E_B is the energy of elastically scattered photons on the ^{11}B resonance, $\varepsilon(E)$ is the detector efficiency, $B(E)$ is the average branching ratio, $S(E)$ is the statistical fluctuation factor, N_B and N_T are the numbers of boron and scattering target atoms in the beam, W is a angular correlation coefficient and $\Phi_E(E)$ is the spectral bremsstrahlung fluence.

The uncertainty of $I_{\mathrm{abs,T}}$ is given by:

$$\left(\frac{\Delta I_{\mathrm{abs,T}}}{I_{\mathrm{abs,T}}}\right)^2 = \left(\frac{\Delta Y_{\mathrm{abs,T}}}{Y_{\mathrm{abs,T}}}\right)^2 + \left(\frac{\Delta Y_{\mathrm{abs,B}}}{Y_{\mathrm{abs,B}}}\right)^2 + \left(\frac{\Delta \Phi_E}{\Phi_E}\right)^2 + \left(\frac{\Delta I_{\mathrm{abs,B}}}{I_{\mathrm{abs,B}}}\right)^2 \tag{4.8}$$

Here, the uncertainty in the number of absorbed photons is given by:

$$\left(\frac{\Delta Y_{\mathrm{abs,T}}}{Y_{\mathrm{abs,T}}}\right)^2 = \left(\frac{\Delta Y_{\mathrm{scat,T}}}{Y_{\mathrm{scat,T}}}\right)^2 + \left(\frac{\Delta \varepsilon}{\varepsilon}\right)^2 + \left(\frac{\Delta B}{B}\right)^2 + \left(\frac{\Delta S}{S}\right)^2 \tag{4.9}$$

The number of elastically scattered photons $Y_{\mathrm{scat}}(i)$ in a bin i is calculated by a stepwise subtraction of simulated inelastic transitions $Y_{\mathrm{inelas,j}}(i)$ of higher lying states at energies E_j from the measured spectrum $Y_{\mathrm{exp}}(i)$.

$$Y_{\mathrm{scat}}(i) = Y_{\mathrm{exp}}(i) - \sum_{j>i} n_j Y_{\mathrm{sim,E_{ex}=E_j}}(i) \tag{4.10}$$

Here, n_j is a normalisation factor of the simulated deexcitation spectra. The uncertainty of Y_{scat} is thus given by:

$$(\Delta Y_{\mathrm{scat}}(i))^2 = (\Delta Y_{\mathrm{exp}}(i))^2 + \sum_{j>i} (\Delta n_j)^2 \left(Y_{\mathrm{sim,E_{ex}=E_j}}(i)\right)^2 + \sum_{j>i} (n_j)^2 \left(\Delta Y_{\mathrm{sim,E_{ex}=E_j}}(i)\right)^2 \tag{4.11}$$

The normalisation factor n_i for the bin i is the ratio of the yield in the bin i of the spectrum corrected for all inelastic transitions from higher bins j divided by the number of simulated ground state transitions for the excitation energy E_i.

$$n_i = \frac{Y_{\mathrm{ex}}(i) - \sum_{j>i} n_j Y_{\mathrm{sim,E_{ex}=E_j}}(i)}{Y_{\mathrm{sim,i}}(i)} \tag{4.12}$$

That means for the highest bin h the normalisation factor is:

$$n_h = \frac{Y_{\mathrm{ex}}(h)}{Y_{\mathrm{sim,E_{ex}=E_h}}(h)} \tag{4.13}$$

Its uncertainty is given by:

$$\left(\frac{\Delta n_h}{n_h}\right)^2 = \left(\frac{\Delta Y_{\mathrm{ex}}(h)}{Y_{\mathrm{ex}}(h)}\right)^2 + \left(\frac{\Delta Y_{\mathrm{sim,E_{ex}=E_h}}(h)}{Y_{\mathrm{sim,E_{ex}=E_h}}(h)}\right)^2 \tag{4.14}$$

For the adjacent bin $h-1$ the factor is given by:

$$n_{h-1} = \frac{Y_{\mathrm{ex}}(h-1) - n_h Y_{\mathrm{sim,E_{ex}=E_h}}(h-1)}{Y_{\mathrm{sim,E_{ex}=E_{h-1}}}(h-1)} \tag{4.15}$$

In general, the normalisation factor n_i depends on all normalisation factors n_j with $j > i$ which means that the uncertainty of n_i increases exponentially with the number of performed subtractions ($n_{\mathrm{sub}} = h - i$).
Estimates for the uncertainties that enter in the uncertainty of $I_{\mathrm{abs,T}}$ are given in table (4.2). At high energies the total uncertainty is determined by the uncertainty of S, B, Φ_E, ε and $I_{\mathrm{abs,B}}$, whereas the uncertainty in the low energy region is completely dominated by the uncertainty of the subtraction of inelastic transitions which rises exponentially with the number of performed subtractions.

As mentioned in section (2.2), the simulation and correction for inelastic transitions needed for the determination of the average photoabsorption cross section and the related photon strength function depends on the used input photon strength functions. Hence, to have a self-consistent analysis, the correction has to be performed several times in an iterative process. As a starting point for the iteration, a TLO $E1$ and a $M1$ strength function discussed in section (2.5.2) were used. In the next step, the mean of input and smoothed output dipole strength function of the previous step is used as new input $E1$ strength function for the simulation of inelastic transitions. This procedure is repeated until input and output strength function are in

quantity	relative uncertainty	comment
Φ_E	5.0 %	due to uncertainty in endpoint energy
$I_{\mathrm{abs,B}}$	4.8 %	from [Ajzenberg-Selove, 1990]
ε	5.0 %	from [Massarczyk, 2011]
B	5.0 %	due to uncertainty in temperature
Y_{sim}	5.0 %	
S	7.0 %	from fluctuation simulation
$Y_{\mathrm{scat,B}}$	3.0 %	from fit of yield in ^{11}B resonance
Y_{exp}	$1/\sqrt{Y_{\mathrm{exp}}}$	statistical unc. of measurement

Table 4.2: Relative uncertainties that enter in the uncertainty of $I_{\mathrm{abs,T}}$ for ^{78}Se(γ,γ)

agreement. Figure (4.20) shows the calculated average photoabsorption cross section after different steps of the iteration for simulations using a CTM level density with $T = 900\,\mathrm{keV}$. This value was chosen from comparisons of simulated and measured ^{77}Se(n,γ) in section (4.2). It is visible that after three iteration steps the input and output strength function (average absorption cross section) are self-consistent. The steep drop of the average photoabsorption cross section above 10.3 MeV is due to the opening (γ,n) channel at 10.49 MeV.

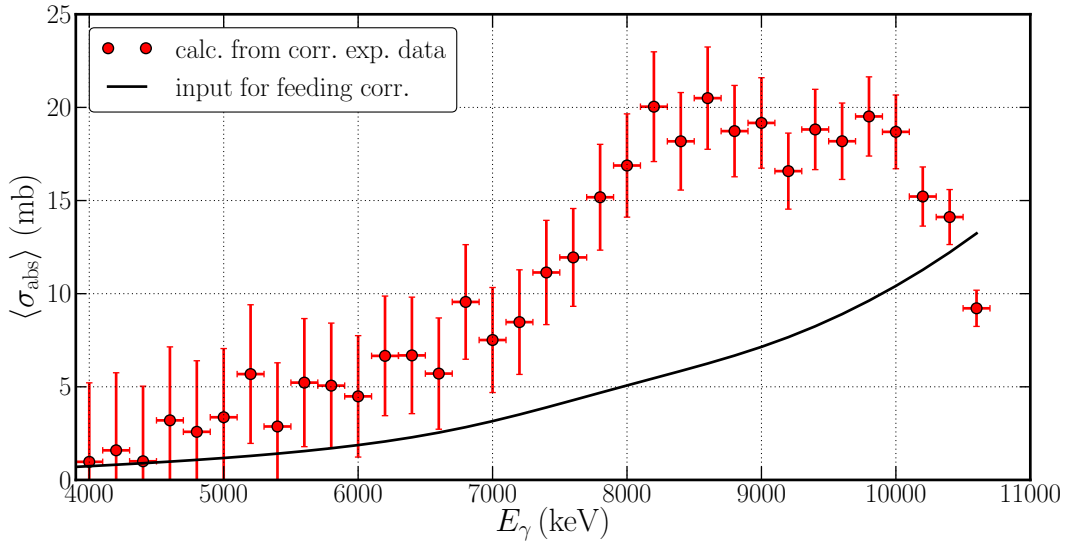

(a) 1st step of the iteration (TLO strength function used as input for the correction of inelastic transitions)

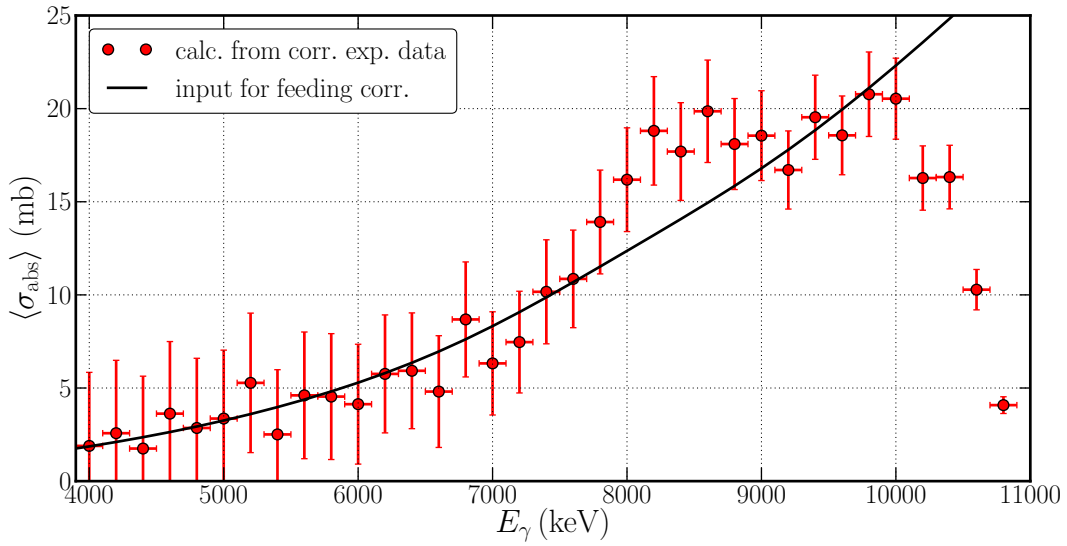

(b) 3rd step of the iteration (mean of input and output strength function of 2nd iteration used as input for the correction of inelastic transitions)

Figure 4.20: Calculated average photoabsorption cross section (red circles) from experimental data of ^{78}Se(γ,γ). The black line represents the average photo absorption cross section deduced from the dipole strength function that was used as input for the simulation and correction of inelastic transitions. For this purpose, the data points of the previous iteration were fitted locally (up to 10 MeV) with a quadratic polynomial. In both cases a CTM level density with $T = 900$ keV and $D_0 = 121$ eV was used for the simulation. After the third step input and output strength functions are self-consistent. The steep drop of the average photoabsorption cross section above 10.3 MeV is due to the opening (γ,n) channel at 10.49 MeV. As mentioned before, the black line is a local fit and therefore must not be extrapolated to higher energies.

E_{res} (keV)	Y_{scat}	Y_{abs}	Φ_E ($\mathrm{eV}^{-1}\mathrm{b}^{-1}$)
8920	376(23)	$2.4(2)\cdot10^{6}$	$1.39(13)\cdot10^{-18}$
7285	689(52)	$3.7(3)\cdot10^{6}$	$6.0(7)\cdot10^{-18}$
5020	4154(146)	$15.4(9)\cdot10^{6}$	$10.4(7)\cdot10^{-18}$
4444	3779(158)	$10.6(7)\cdot10^{6}$	$11.3(9)\cdot10^{-18}$
2124	5151(726)	$6.9(13)\cdot10^{6}$	$23(5)\cdot10^{-18}$

Table 4.3: Spectral bremsstrahlung fluence deduced from fits to the measured gamma yield of elastically scattered photons on ^{11}B resonances in the ^{196}Pt(γ,γ) experiment. Y_{scat} is the number of measured elastically scattered photons from a resonance at E_{res}. Y_{abs} is the calculated number of absorbed photons in the resonance and Φ_E is the spectral bremsstrahlung fluence.

4.3.2 Analysis of Photon Scattering from Platinum-196

The analysis of the photon scattering experiment on ^{196}Pt was performed in a similar way to the analysis of ^{78}Se(γ,γ). Therefore, only the results of the important steps are presented in the following.

Determination of the Bremsstrahlung Fluence

As in the ^{78}Se(γ,γ) experiment, elastic photon scattering on a ^{11}B calibration target was used to determine the incident bremsstrahlung fluence in the ^{196}Pt(γ,γ) experiment. The number of elastically scattered photons and the deduced fluence at the transition energies are shown in table (4.3).
The fluence deduced from scattering from the 5020 keV resonance was used to normalise the calculated bremsstrahlung fluence with the Seltzer and Berger formula using a kinetic electron energy of 9.5 MeV which was measured with the Browne-Buechner spectrometer of ELBE. Due to this low endpoint energy the fluence deduced from the 8920 keV resonance is not capable for the flux normalisation because close to the endpoint energy the bremsstrahlung spectrum strongly depends on the exact value of the electron energy. An uncertainty of 200 keV for an endpoint energy of 9.5 MeV results in a relative uncertainty in the calculated fluence at 8920 keV of approximately 25 %. In contrast, it only leads to an uncertainty of approximately 3 % at 5020 keV. Moreover, the statistical uncertainty of the gamma yield scattered from the 5020 keV resonance is much smaller.
Figure (4.21) shows the shape of the incident spectral bremsstrahlung fluence in the ^{196}Pt(γ,γ) experiment. Up to the neutron separation energy of ^{196}Pt (7922 keV), the uncertainty of the bremsstrahlung fluence can be estimated to 8 % at maximum.

Correction for Non-Nuclear Scattered Transitions

As in the case of ^{78}Se(γ,γ), the spectrum of non-nuclear scattered events was simulated with GEANT4 by Ralph Massarczyk. Inexplicably the results of the simulation do not fit to the measured spectrum. Nevertheless, as shown in figure (4.15), it can be assumed that at high energies (> 6 MeV) the ratio of nuclear and non-nuclear

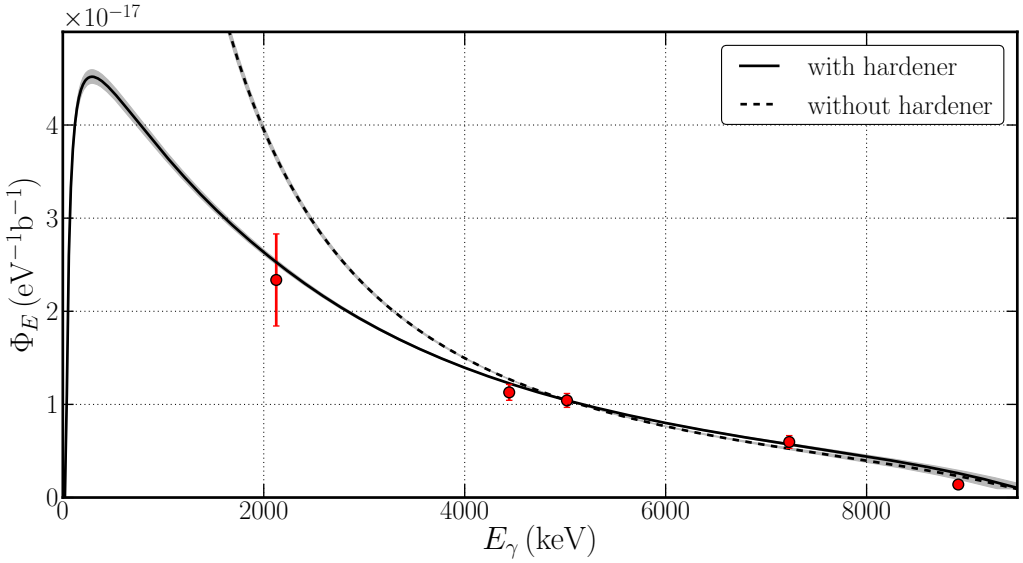

Figure 4.21: Spectral bremsstrahlung fluence of the ^{196}Pt(γ,γ) experiment. The red circles correspond to the fluence determined from measured transitions in ^{11}B. The dashed black line is the flux distribution calculated using the Seltzer and Berger Formula. The solid black line takes the influence of the aluminium hardener into account. Both curves are normalised to the fluence deduced from scattering from the 5020 keV resonance. The gray bands correspond to the uncertainty due to a 200 keV uncertainty of the 9500 keV electron kinetic energy.

scattered events is negligibly small. Thus, the measured data was only analysed above 6 MeV so far under the assumption that above this energy the contribution of non-nuclear scattered background is negligible.

Correction for Inelastic Transitions

For the correction of inelastic events deexcitation spectra and ground state branching ratios for excitation energies up to S_n in steps of 200 keV were simulated. The resulting spectra and enhanced average ground state branching ratios are shown in figures (4.22) and (4.23) respectively. In addition the simulated statistical fluctuation factor is shown in figure (A.2) in the appendix.
Obviously, the simulated enhanced ground state branching ratios for ^{196}Pt are much smaller then those of ^{78}Se which is due to the higher level density of ^{196}Pt compared to ^{78}Se ($D_0 = 19.2\,\text{eV} \Leftrightarrow D_0 = 121\,\text{eV}$). Moreover, it can be seen that small uncertainties in the CTM temperature lead to large uncertainties in the branching ratios ($\approx 40\%$ at 8 MeV, 30% at 6 MeV) which makes a precise estimate of B_0 difficult.
Figure (4.24) shows the subtraction of inelastic transitions and the correction for branching using the simulated deexcitation spectra for the response corrected measured ^{196}Pt(γ,γ) spectrum. What can be seen is that at 6 MeV (2 MeV below S_n) approximately 50 % of the measured gamma yield are inelastic transitions. The rise in the measured yield with decreasing gamma energy below 6 MeV is due to atomic background which is not subtracted from the spectrum.

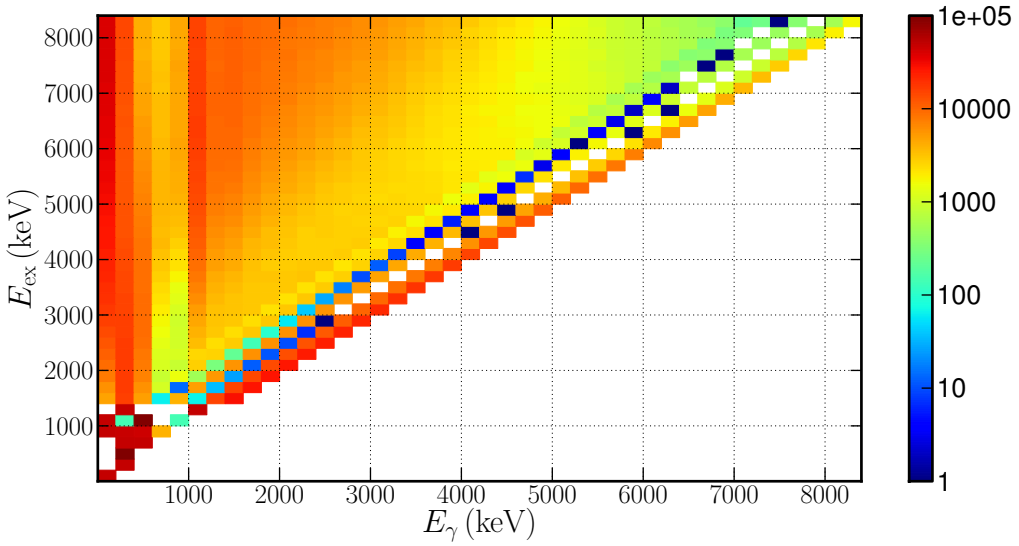

Figure 4.22: Simulated deexcitation spectra for excited 1^- states in ^{196}Pt in steps of 200 keV. For each excitation energy 50000 deexcitations were simulated. A CTM level density with $T = 600\,\text{keV}$ and $D_0 = 19.2\,\text{eV}$ and a TLO $E1$ strength function were used as input parameters.

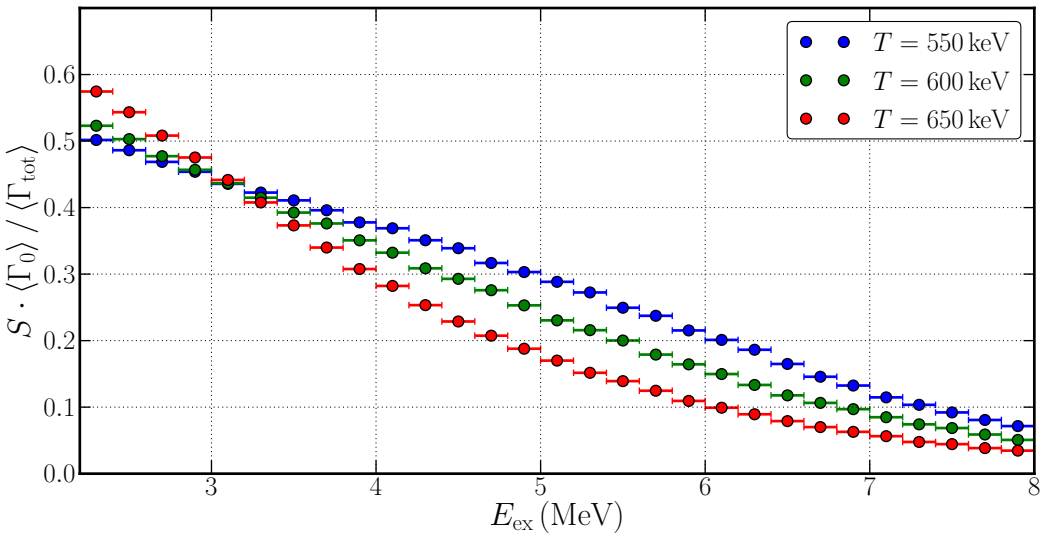

Figure 4.23: Simulated ground state branching ratios for ^{196}Pt. For the simulations a CTM level density with different temperatures T, but a fixed mean resonance spacing at the threshold $D_0 = 19.2\,\text{eV}$ and an $E1$ TLO strength function were used.

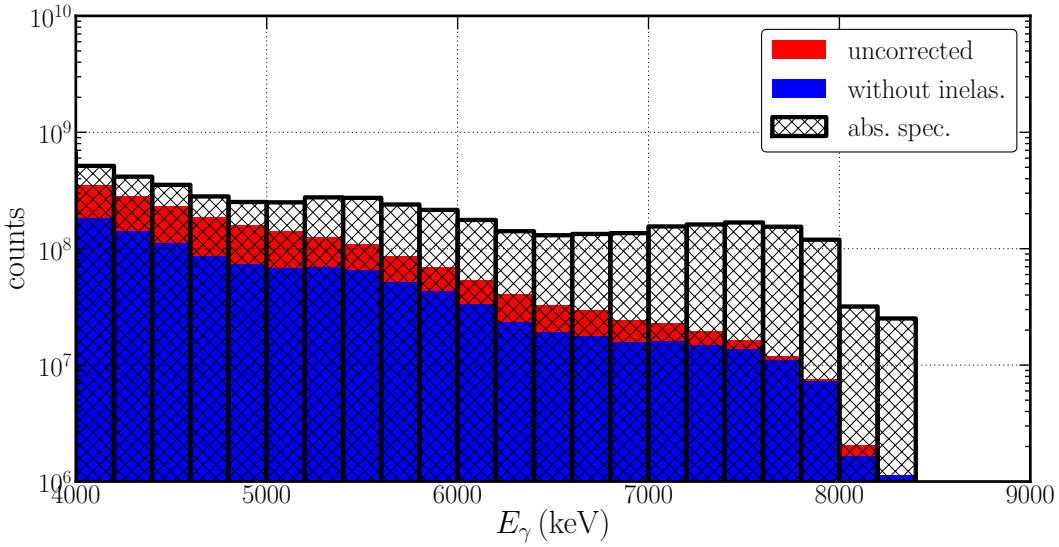

Figure 4.24: Different steps in the correction for inelastic transitions. The response and efficiency corrected measured spectrum containing elastic and inelastic transitions (red), the spectrum without inelastic transitions and the calculated absorption spectrum (black hatched) are shown for ^{196}Pt(γ,γ) using the simulated deexcitation spectra shown in figure (4.22). The uncorrected spectrum (red) still contains the atomic background which distorts the correction at energies below 6 MeV.

In the last step of the analysis, the average photoabsorption cross section was calculated from the absorption spectrum with the help of equations (4.6) and (4.8). The relative uncertainties that enter into equation (4.8) are listed in table (4.4). Obviously, the large uncertainties in the simulated branching ratios dominate the total uncertainty. Figure (4.25) shows the resulting calculated average photoabsorption cross section for ^{196}Pt. The steep drop in the cross section at 8 MeV is due to the opening of the (γ,n) channel at 7.9 MeV. Due to the failure of the atomic background subtraction, the cross section is only shown for energies above 6 MeV where it is assumed that the contribution of non-nuclear scattered events to the measured yield is negligible. For the used CTM level density with $T = 550$ keV, $D_0 = 19.2$ eV and a TLO $E1$ strength function, the subtraction procedure is already self-consistent after the first iteration. In the considered energy range, the relative uncertainty of the calculated average absorption cross section is 35 % which mainly results from the large uncertainties in the estimated ground state branching ratios.

quantity	relative uncertainty	comment
Φ_E	5.0 %	due to uncertainty in endpoint energy
$I_{\mathrm{abs,B}}$	3.5 %	from [Ajzenberg-Selove, 1990]
ε	5.0 %	from [Massarczyk, 2011]
B	30.0 %	due to uncertainty in temperature
Y_{sim}	5.0 %	
S	7.0 %	from fluctuation simulation
$Y_{\mathrm{scat,B}}$	3.5 %	from fit of yield in ^{11}B resonance
Y_{exp}	$1/\sqrt{Y_{\mathrm{exp}}}$	statistical unc. of measurement

Table 4.4: Relative uncertainties that enter in the uncertainty of $I_{\mathrm{abs,T}}$ for ^{196}Pt(γ,γ)

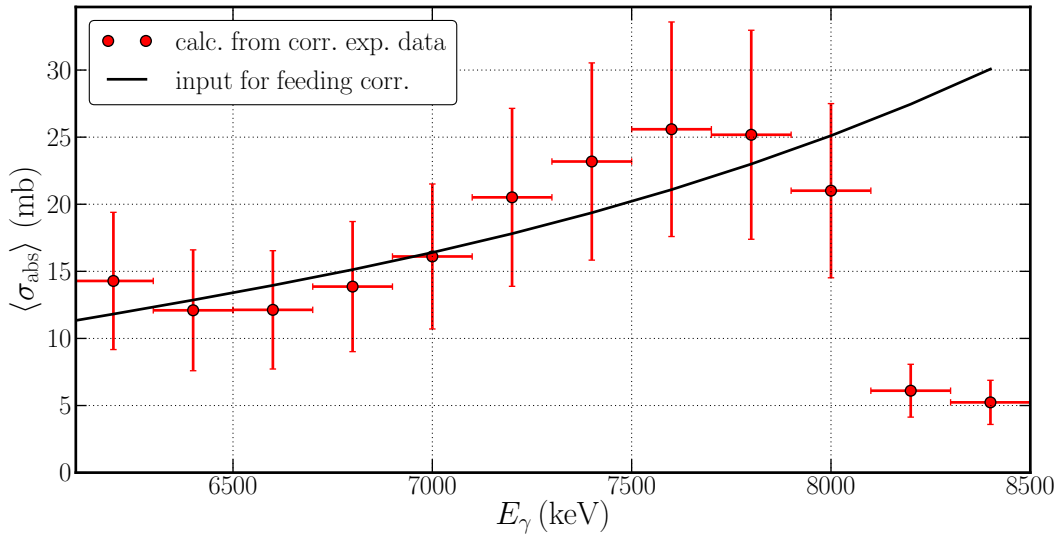

Figure 4.25: Calculated average photoabsorption cross section (red circles) from ^{196}Pt(γ,γ). The black line represents the average photoabsorption cross section deduced from the dipole strength function that was used as input for the simulation and correction of inelastic transitions. For the simulation a CTM level density with $T = 550\,\mathrm{keV}$ and $D_0 = 19.2\,\mathrm{eV}$ was used. The steep drop of the average photoabsorption cross section above 7.8 MeV is due to the opening (γ,n) channel at 7.9 MeV.

Chapter 5
Results, Discussion and Outlook

In the following chapter the results gained from the analysis of the two twin experiments ^{77}Se(n,γ) / ^{78}Se(γ,γ) and ^{195}Pt(n,γ) / ^{196}Pt(γ,γ) are presented and discussed. Moreover a brief outlook is given.

5.1 Selenium

The analysis of the ^{77}Se(n,γ) experiment revealed three major insights:

- The developed simulation code for the description of gamma deexcitations of excited nuclear states works well, and is able to nicely reproduce the shape of the continuum region of the measured neutron capture gamma spectrum.
- From a comparison of the shape of the continuum region of the simulated and experimental spectrum, it can be concluded that the total level density in the compound nucleus ^{78}Se is described best by a Constant Temperature Model (CTM) with a temperature of $T = 900\,\mathrm{keV}$ and $D_0 = 121\,\mathrm{eV}$.
- An enhanced measured gamma yield at 6.3 MeV is a hint for strength additional to Lorentzian models. In order to reproduce the enhanced yield a 200 keV wide resonance like structure at 6.3 MeV is necessary (see figure (4.8)) which contributes to about 5 % of the photon strength below S_n equivalent to 0.1 % of the Thomas-Reiche-Kuhn sum rule.

With the help of the gained information about the level density in the compound nucleus and the developed simulation code for gamma deexcitations, it was possible to perform the correction for inelastically scattered events in the analysis of the photon scattering experiment ^{78}Se(γ,γ) in a fast and efficient way. Figure (5.1) shows the final deduced average photoabsorption cross section after three iterations of the correction for inelastic transitions. In addition, the experimental (γ,n) cross section [Carlos et al., 1976] scaled with 0.85 due to a normalisation uncertainty proposed by [Berman et al., 1987] and the absorption cross section calculated from Single Lorentzian (SLO) and Triple Lorentzian (TLO) $E1$ strength functions are shown. At the neutron separation energy ($S_\mathrm{n} = 10.5\,\mathrm{MeV}$) the photon scattering data match the (γ,n) data. Above the threshold the photon scattering cross section rapidly decreases due to the opening (γ,n) channel. Below the threshold, where photon scattering is the only contribution to photoabsorption, the measured data are up to a factor of three higher than the SLO and TLO model predictions. A resonance

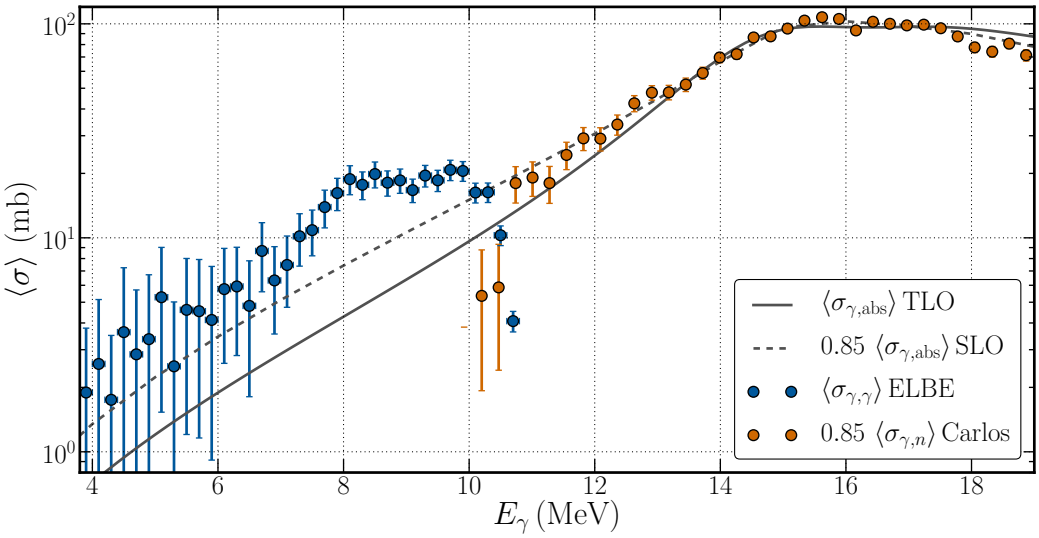

Figure 5.1: Average photoabsorption cross section for ^{78}Se. The blue circles are values measured via photon scattering at HZDR. The orange circles are values from (γ,n) measurements at Saclay [Carlos et al., 1976] scaled with 0.85 due to a systematic error proposed by [Berman et al., 1987]. Moreover the absorption cross section calculated from SLO (dashed line) and TLO (solid line) $E1$ strength functions are shown. The calculated numerical values are given in table (A.7) in the appendix.

structure at 6.3 MeV, as seen in the ^{77}Se(n,γ) spectrum, is not visible. However, it should be mentioned that the uncertainties of the photon scattering data at this energies are large ($\approx 70\,\%$) due to the stepwise subtraction method. In contrast to the (n,γ) analysis, the (γ,γ) data show a broad increased strength around 8.2 MeV equivalent to approximately 1.3 % of the Thomas-Reiche-Kuhn sum rule.

5.2 Platinum

From the analysis of the ^{195}Pt(n,γ) experiment the following conclusions can be drawn:

- Simulations with a CTM level density with $T = 650\,\mathrm{keV}$ and $D_0 = 19.2\,\mathrm{eV}$ describe the slope of the continuum region in the measured gamma spectrum best. This value for T is higher than the ones given in the compilations [Koning et al., 2008] ($T_\mathrm{K} = 550\,\mathrm{keV}$) and in [Egidy and Bucurescu, 2009] ($T_\mathrm{E} = 600\,\mathrm{keV}$).

- An enhanced measured gamma yield at 5.4 MeV is a hint for extra strength at this transition energy. As discussed in [Bartholomew et al., 1973], this extra strength must be of $E1$ type. Simulations with a modified $E1$ strength function show that the enhanced yield can be reproduced with a Gaussian extra strength at 5.4 keV with $\sigma = 250\,\mathrm{keV}$ (see figure (4.12)) which contributes

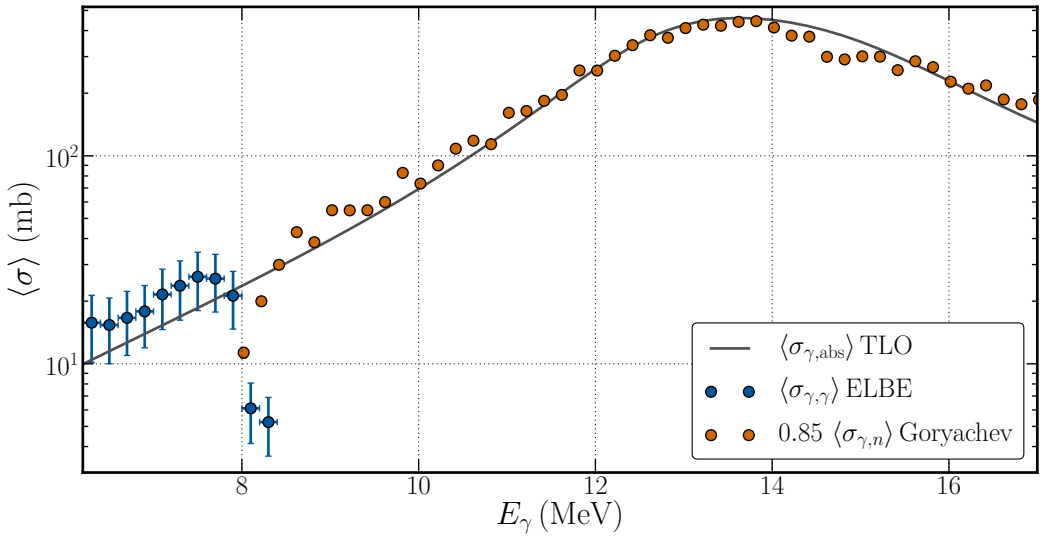

Figure 5.2: Average photoabsorption cross section for ^{196}Pt. The blue circles are values measured via photon scattering at HZDR. The orange circles are values from (γ,n) measurements from [Goryachev and Zalesnyi, 1978] scaled with 0.85. Moreover the absorption cross section calculated from SLO (dashed line) and TLO (solid line) $E1$ strength functions are shown. The calculated numerical values are given in table (A.7) in the appendix.

to about 17 % of the photon strength below S_n equivalent to 0.3 % of the Thomas-Reiche-Kuhn sum rule.

The deduced information about the level density in the compound nucleus ^{196}Pt were used in the correction for inelastically scattered events in the analysis of ^{196}Pt(γ,γ). Figure (5.2) shows the average photoabsorption cross section calculated from the corrected measured photon scattering spectrum. In addition, the experimental (γ,n) cross section from [Goryachev and Zalesnyi, 1978] scaled with 0.85 and the prediction of the global TLO model are presented. In contrast to ^{78}Se, no SLO data from [RIP, 2011] was available for ^{196}Pt. Below the neutron separation energy (S_n = 7.9 MeV), where photon scattering is the only contribution to the photoabsorption cross section, the calculated data exceed on average 33 % the TLO prediction. Nevertheless, the general trend is nicely described by the TLO model. At the neutron threshold the photon scattering data matches the (γ,n) data. Above the threshold, where the photoabsorption cross section is dominated by the rising (γ,n) channel, the photon scattering contribution strongly decreases. The relative uncertainty of the calculated photoabsorption cross section in the region between 6 MeV and 8 MeV is approximately 35 % and dominated by the uncertainty in the estimated ground state branching ratio.

Due to the failure of the atomic background correction, an analysis of the data was only reasonable above 6 MeV. Thus it yet remains unclear whether the deduced extra $E1$ strength from ^{195}Pt(n,γ) is also observed in photon scattering.

5.3 Discussion and Outlook

The main effort of this thesis was the development and implementation of a new, fast and efficient simulation algorithm using an extreme statistical approach for the description of radiative nuclear deexcitations. The application of this code in the analysis of the two twin experiments revealed qualitative and quantitative information about level density and $E1$ photon strength function and the related average photoabsorption cross section below the neutron separation energy in the compound nuclei ^{78}Se and ^{196}Pt. In both cases the calculated photoabsorption cross section below S_n exceeds the predictions of the global TLO $E1$ model. The hints for extra $E1$ strength in the neutron capture gamma spectra of ^{77}Se at 6.3 MeV could not be confirmed in the analysis of the photon scattering experiments on ^{78}Se. In contrast, extra strength in a rather broad distribution is visible in the photon scattering data around 8.2 MeV. For ^{196}Pt, the hints for extra strength at 5.4 MeV could not be verified so far, due to the failure of the atomic background correction. With respect to the different results of the twin experiments on selenium, it still remains an open questions whether these two different experimental types reveal information about the exactly same quantity. In addition, recent $(\alpha,\alpha'\gamma)$ and (γ,γ) measurements on ^{124}Sn [Endres et al., 2010] show extra $E1$ strength at different excitation energies, as well, raising the question whether different excitation methods are sensitive to different excited states in nuclei.

Possible future benchmark tests for the developed simulation algorithm can be the analysis of photon scattering experiments performed at HIγS [Tonchev et al., 2005] where quasi monochromatic photons from Laser Compton backscattering are used for nuclear excitations. In principle, due to the known and relatively sharp excitation energy ($\Delta E \approx 200$ keV) the code is directly able to simulate the emitted deexcitation spectra. In addition, the finite energy spread assures that at high energies several states are excited and a extreme statistical treatment of the scattering process is valid.

Another major insight of this thesis is the enhancement of elastic transitions in photon scattering due to fluctuations in the transition widths. This enhancement could be quantified with the statistical fluctuation factor S. So far, this factor is simulated as a function of excitation energy for a given level density and strength function. However, regarding figure (2.14) it seems that there is a unique definite relation between S and the ratio of average inelastic transition width and average elastic transition width. An analytic expression or a numerical parametrisation for this relation would redundantise the simulations of S leading to even shorter calculation times of the deexcitation spectra needed for the correction of inelastic transitions in the analysis of photon scattering experiments. Moreover, it could be shown that the shape of the distribution of the fluctuations in the transitions widths directly influences the magnitude of the elastic enhancement. Perhaps, this fact could give insight in the ongoing discussion about the validity of the Porter-Thomas distribution currently investigated using high resolution neutron resonance data [Koehler et al., 2010], [Weidenmüller, 2010].

Appendix A
Figures and Tables

$$I_{\text{abs}} = \left(\frac{\pi\hbar c}{E_{\text{res}}}\right)^2 \frac{2I_i + 1}{2I_0 + 1}\,\Gamma_0 \tag{A.1}$$

$$I_{\text{scat}} = I_{\text{abs}} \cdot \frac{\Gamma_0}{\Gamma_{\text{tot}}} = I_{\text{abs}} \cdot B_0 \tag{A.2}$$

E_{res} (keV)	J^Π	E_{127} (keV)	Γ_0 (eV)	B_0	I_{abs} (eVb)	I_{scat} (eVb)
2124.7(3)	$1/2^-$	2124.2(3)	0.120(9)	1	51(4)	51(4)
4444.9(5)	$5/2^-$	4442.8(5)	0.56(2)	1	163(6)	163(6)
5020.3(3)	$3/2^-$	5017.6(3)	1.68(6)	0.858(4)	256(9)	220(8)
7285.5(4)	$5/2^+$	7279.8(4)	1.00(7)	0.884(3)	109(8)	96(7)
8920.2(6)	$5/2^-$	8912.4(6)	4.15(20)	0.973(1)	301(15)	293(14)

Table A.1: Properties of resonances in ^{11}B used for the determination of the incident bremsstrahlung fluence in photon scattering experiments. E_{res} is the energy of the resonance, E_{127} is the ground state transition energy under 127°, J^Π are spin and parity of the resonance, Γ_0 is the ground state transition width taken from [Ajzenberg-Selove, 1990], B_0 is the ground state branching ratio taken from [Rusev et al., 2009], I_{abs} is the integrated absorption cross section and I_{scat} is the integrated cross section for elastic scattering.

	A (keV^{-3})	E_0 (keV)	σ (keV)
TLO + x1 (blue)	$1.18 \cdot 10^{-16}$	5400	250
TLO + x2 (red)	$1.88 \cdot 10^{-16}$	5400	250
TLO + x3 (green)	$2.34 \cdot 10^{-16}$	5500	500

Table A.2: Parameters of extra Gaussian resonances added to the $E1$ strength function for the simulation of ^{195}Pt(n,γ). The resulting strength functions are shown in figure (4.13).

quantity	value	comment
neutron separation energy S_n	10498 keV	[Farhan and Singh, 2009]
total level density model: CTM		
temperature T	850 keV	from [Koning et al., 2008]
average neutron resonance spacing D_0	121 eV	from [Mughabghab, 2006]
CTM back shift E_0	413 keV	calc. from T, D_0, $f(J)$
spin cut-off model: Koning		
discrete spin cut-off σ_d	2.145	from [Koning et al., 2008]
discrete spin cut-off energy E_d	2018 keV	from [Koning et al., 2008]
spin cut-off at S_n σ_{S_n}	4.382	from [Koning et al., 2008]
E1 strength function: TLO		
quadrupole deformation β	0.271	from [Raman et al., 2001]
triaxiality γ	27.1°	from [Andrejtscheff, 1994]
M1 strength function:		data for parametrisation
Grosse parametrisation		from [Heyde et al., 2010]

Table A.3: Input parameters for simulations of ^{77}Se(n,γ) and ^{78}Se(γ,γ).

quantity	value	comment
neutron separation energy S_n	7922 keV	[Xiaolong, 2007]
total level density model: CTM		
temperature T	553 keV	from [Koning et al., 2008]
average neutron resonance spacing D_0	19.2 eV	from [Mughabghab, 2006]
CTM back shift E_0	136 keV	calc. from T, D_0, $f(J)$
spin cut-off model: Koning		
discrete spin cut-off σ_d	3.03	from [Koning et al., 2008]
discrete spin cut-off energy E_d	1137 keV	from [Koning et al., 2008]
spin cut-off at S_n σ_{S_n}	6.65	from [Koning et al., 2008]
E1 strength function: TLO		
quadrupole deformation β	0.13	from [Raman et al., 2001]
triaxiality γ	31.9°	from [Andrejtscheff, 1994]
M1 strength function:		data for parametrisation
Grosse parametrisation		from [Heyde et al., 2010]

Table A.4: Input parameters for simulations of ^{195}Pt(n,γ) and ^{196}Pt(γ,γ).

			^{78}Se			^{196}Pt
ex. state	E (keV)	J^Π	$P_{1st,\gamma}$	E (keV)	J^Π	$P_{1st,\gamma}$
0	0	0^+	0.007	0.0	0^+	0.0055
1	613.72	2^+	0.073	355.68	2^+	0.0021
2	1308.64	2^+	0.048	688.693	2^+	0.0056
3	1498.60	0^+	0.002	876.86	4^+	0.0000
4	1502.82	4^+	0.000	1015.04	3^+	0.0000
5	1758.69	0^+	0.001	1135.31	0^+	0.0011
6	1853.93	3^+	0.000	1270.21	5^-	0.0000
7	1995.90	2^+	0.015	1293.31	4^+	0.0000
8	2190.65	4^+	0.000	1361.58	2^+	0.0018
9	2327.32	2^+	0.016	1373.60	7^-	0.0000
10	2335.21	0^+	0.018	1402.73	0^+	0.0007

Table A.5: Energies, spins and parities of the first excited states of ^{78}Se and ^{196}Pt [RIP, 2011]. $P_{1st,\gamma}$ are the transition probabilities for primary gammas emitted from the resonance excited in cold neutron capture to the respective excited state [PGA, 2011].

E_{res} keV	E_f keV	B
8920.20	0	0.973
	4444.89	0.027
7285.51	0	0.884
	4444.89	0.053
	5020.31	0.063
5020.31	0	0.858
	2124.69	0.142
4444.89	0	1
2124.69	0	1

Table A.6: Branching ratios of resonances in ^{11}B at E_{res} to possible final resonances at E_f taken from [Rusev et al., 2009].

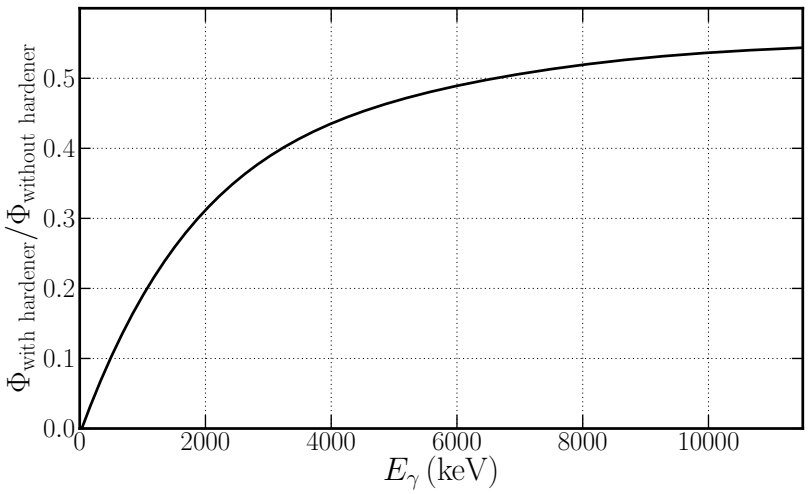

Figure A.1: Ratio of bremsstrahlung fluence at the target position with and without a 10 cm aluminium hardener in front of the collimator. The function was deduced with a GEANT4 simulation. The aluminium hardener absorbs more photons in the low energy region and thus hardens the spectrum.

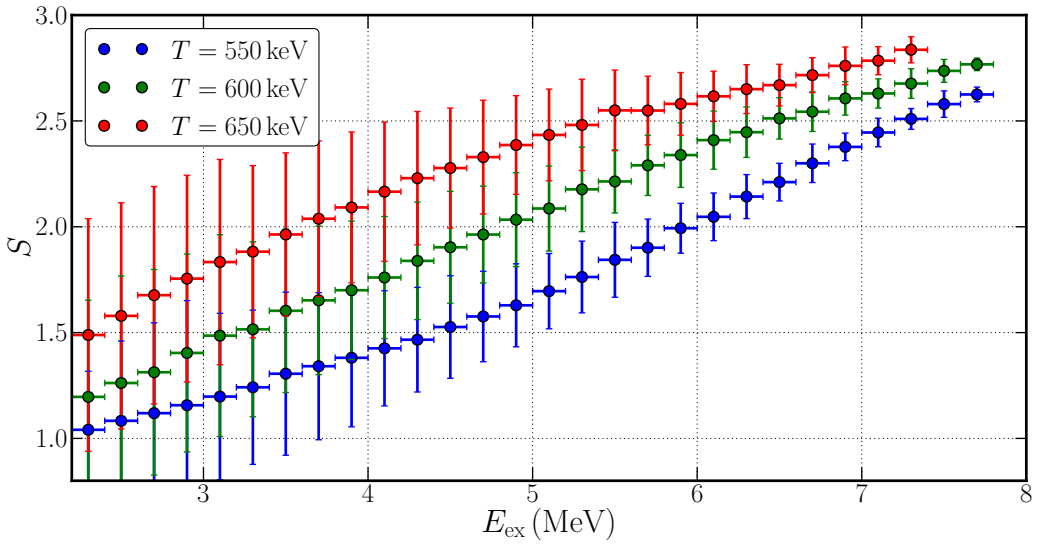

Figure A.2: Simulated statistical fluctuation factor for ^{196}Pt. For the simulations a CTM level density with different temperatures T, but a fixed mean resonance spacing at the threshold $D_0 = 19.2\,\text{eV}$ and an $E1$ TLO strength function were used.

(a) Isometric projection

(b) Projection along the x-axis

(c) Projection along the y-axis

(d) Projection along the z-axis

Figure A.3: Triaxial shape of ^{78}Se (left) and ^{196}Pt (right). The deformation parameters β and γ are given in tables (A.3) and (A.4). The resulting ratios of the x, y and z semi axis are $0.99 : 0.87 : 1.16$ for ^{78}Se and $1.00 : 0.93 : 1.07$ for ^{196}Pt. The ellipsoids are scaled with $A^{-1/3}$.

E_γ (MeV)	^{78}Se $\langle\sigma_{\gamma,\mathrm{abs}}\rangle$ (mb)	^{196}Pt $\langle\sigma_{\gamma,\mathrm{abs}}\rangle$ (mb)
4.1	3(4)	
4.3	2(4)	
4.5	4(4)	
4.7	3(4)	
4.9	3(4)	
5.1	5(4)	
5.3	3(3)	
5.5	5(3)	
5.7	5(3)	
5.9	4(3)	
6.1	6(3)	19(6)
6.3	6(3)	16(6)
6.5	5(3)	15(5)
6.7	9(3)	17(6)
6.9	6.3(27)	18(6)
7.1	7.5(27)	22(7)
7.3	10.2(28)	24(8)
7.5	10.9(26)	26(8)
7.7	13.9(28)	26(8)
7.9	16.2(28)	21(7)
8.1	18.8(29)	6.1(20)
8.3	17.7(26)	5.2(16)
8.5	19.9(28)	
8.7	18.1(24)	
8.9	18.5(24)	
9.1	16.7(21)	
9.3	19.5(23)	
9.5	18.6(21)	
9.7	20.8(23)	
9.9	20.5(22)	
10.1	16.3(17)	
10.3	16.3(17)	
10.5	10.3(11)	
10.7	4.5(5)	

Table A.7: Calculated average photoabsorption cross sections of ^{78}Se and ^{196}Pt.

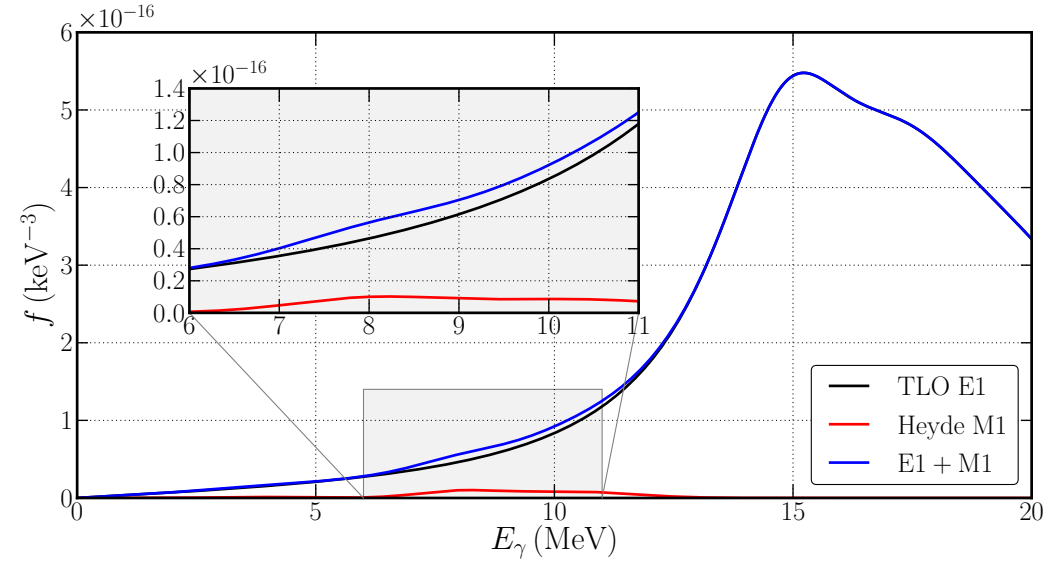

(a) ^{78}Se

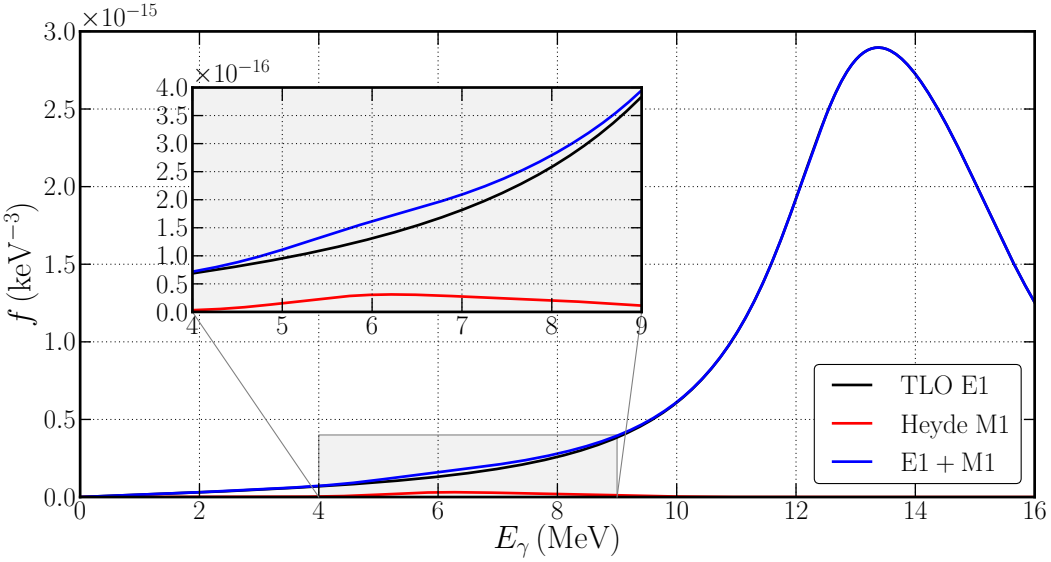

(b) ^{196}Pt

Figure A.4: $E1$ (black), $M1$ (red) and $E1+M1$ (blue) strength functions in comparison for ^{78}Se and ^{196}Pt. The used input parameters for the TLO and Grosse parametrisation are given in tables (A.3) and (A.4).

experiment	kinetic electron energy	average current	measuring time
^{78}Se(γ,γ)	11.5 MeV	0.5 mA	144.5 h
^{196}Pt(γ,γ)	9.5 MeV	0.7 mA	89.5 h

Table A.8: Parameters of the photon scattering experiments

List of Figures

2.1 Scheme of neutron capture 9
2.2 Energy scheme of neutron capture 10
2.3 Measured ^{77}Se(n,γ) spectrum 11
2.4 Porter-Thomas distribution 12
2.5 Rebinned ^{77}Se(n,γ) spectrum 13
2.6 Scheme of photon scattering 14
2.7 Uncorrected measured ^{78}Se(γ,γ) spectrum 15
2.8 Total level density for ^{78}Se 22
2.9 The spin distribution factor σ^2 for ^{78}Se 24
2.10 Comparison of TLO and $\sigma_{\gamma n}$ for ^{78}Se and ^{196}Pt 27
2.11 $M1$ strength functions 28
2.12 Simulation algorithm for the statistical fluctuation factor 31
2.13 Energy dependence of the statistical fluctuation factor S for ^{78}Se . . . 32
2.14 The statistical fluctuation factor S as a function of R 32

3.1 Floor plan of the research reactor at IKI Budapest 34
3.2 PGAA setup in Budapest 34
3.3 Floor plan of the Bremsstrahlung facility at ELBE 35
3.4 Nuclear physics cave at ELBE 36

4.1 Average spectral distribution of primary gamma rays 39
4.2 Influence of level density and strength function on $\nu(E_\gamma)$ 40
4.3 Simulation scheme 41
4.4 Measured and response corrected Urea-d(n,γ) spectra 43
4.5 Corrected ^{77}Se(n,γ) spectrum 44
4.6 Simulated ^{77}Se(n,γ) spectra 46
4.7 Simulated ^{77}Se(n,γ) spectra with different temperatures T 47
4.8 Comparison of experimental and simulated ^{77}Se(n,γ) spectra 48
4.9 Input level densities and strength functions for ^{77}Se(n,γ) simulation . 49
4.10 Corrected ^{195}Pt(n,γ) spectrum 50
4.11 Simulated ^{195}Pt(n,γ) spectra with different T 51
4.12 Simulations of ^{195}Pt(n,γ) with a modified $E1$ strength function 53
4.13 Input level densities and strength functions for ^{195}Pt(n,γ) simulation . 54
4.14 Spectral bremsstrahlung fluence for ^{78}Se(γ,γ) 56
4.15 Simulation and subtraction of the atomic background for ^{78}Se(γ,γ) . . 57
4.16 Simulated deexcitation spectra for ^{78}Se 59
4.17 Simulated statistical fluctuation factor for ^{78}Se 59
4.18 Simulated ground state branching ratios for ^{78}Se 60
4.19 Steps in the correction for inelastic transitions for ^{78}Se(γ,γ) 61
4.20 Calculated average photoabsorption cross section for ^{78}Se(γ,γ) 64

4.21 Spectral bremsstrahlung fluence for ^{196}Pt(γ,γ) 66
4.22 Simulated deexcitation spectra for ^{196}Pt 67
4.23 Ground state branching ratios and statistical fluctuation factor for ^{196}Pt 67
4.24 Steps in the correction for inelastic transitions for ^{196}Pt(γ,γ) 68
4.25 Calculated average photoabsorption cross section for ^{196}Pt(γ,γ) . . . 69

5.1 Average photoabsorption cross section for ^{78}Se 72
5.2 Average photoabsorption cross section for ^{196}Pt 73

A.1 Simulated hardener function IV
A.2 Simulated statistical fluctuation factor for ^{196}Pt IV
A.3 Shape of ^{78}Se and ^{196}Pt V
A.4 $E1$ and $M1$ strength functions VII

List of Tables

2.1 Characteristics of $E1$, $M1$ and $E2$ gamma ray transitions 19
2.2 Symbols for gamma-ray strength functions 25
2.3 Parameters used for the M1 strength function parametrization 28

4.1 Spectral bremsstrahlung fluence for ^{78}Se(γ,γ) 56
4.2 Uncertainties that enter in the uncertainty of $I_{\mathrm{abs,T}}$ for ^{78}Se(γ,γ) . . . 63
4.3 Spectral bremsstrahlung fluence for ^{196}Pt(γ,γ) 65
4.4 Uncertainties that enter in the uncertainty of $I_{\mathrm{abs,T}}$ for ^{196}Pt(γ,γ) . . 69

A.1 Properties of resonances in ^{11}B I
A.2 Parameters of Gaussian resonances added to the TLO $E1$ strength function I
A.3 Input parameters for simulations of ^{77}Se(n,γ) and ^{78}Se(γ,γ) II
A.4 Input parameters for simulations of ^{195}Pt(n,γ) and ^{196}Pt(γ,γ) II
A.5 Energies, spins and parities of the first excited states of ^{78}Se and ^{196}Pt III
A.6 Branching ratios of resonances in ^{11}B III
A.7 Calculated average photoabsorption cross sections VI
A.8 Parameters of the photon scattering experiments VII

Declaration / Erklärung

Hiermit versichere ich, dass ich die vorliegende Arbeit ohne unzulässige Hilfe Dritter und ohne Benutzung anderer als der angegebenen Hilfsmittel angefertigt habe. Die aus fremden Quellen direkt oder indirekt übernommenen Gedanken sind als solche kenntlich gemacht. Die Arbeit wurde bisher weder im Inland noch im Ausland in gleicher oder ähnlicher Form einer anderen Prüfungsbehörde vorgelegt.

Georg Schramm
Dresden, 31.03.2011

Acknowledgement

No thesis is ever product of one person's effort. Without the help of many colleagues this work would have never become reality. Therefore, I am grateful for the outstanding encouragement, guidance and support of my supervisor Andreas Wagner, my advisors Arnd Junghans, Ronald Schwengner, Eckart Grosse, my professors Thomas Cowan and Kai Zuber and my colleagues Ralph Massarczyk, Evert Birgersson, Toni Kögler, Roland Hannaske, Roland Beyer, Michael Fauth, Daniel Bemmerer, Konrad Schmidt and Michael Anders. Moreover I would like to thank Tamas Belgya and his group for the great support of our experiments in Budapest and the ELBE team for the support of our photon scattering experiments at HZDR. In addition, I would like to show my gratitude to the whole Institute of Radiation Physics at HZDR, for the great working atmosphere and scientific freedom provided to me.

This thesis and my graduation would not have been possible without the guidance, patience and support of my beloved parents and my brother. Furthermore, as everyone knows, science is not all in life. Therefore, I would like to thank explicitly all my marvellous friends. Without the wonderful time you shared with me after work during the legendary and untroubled last year, I would not have had the power, motivation and endurance to write this thesis. Last but not least, I would like to thank all people who reviewed this work. My apologies if I have inadvertently omitted anyone to whom acknowledgement is due.

Bibliography

[EU, 2007] (2007). Communication from the commission to the european council and the european parliament - An energy policy for europe. `http://eur-lex.europa.eu/LexUriServ/site/en/com/2007/com2007_0001en01.pdf`. (7th March 2011).

[PGA, 2011] (2011). Prompt Gamma-ray Neutron Activation Analysis Library. `http://www-nds.iaea.org/pgaa/pgaa7/index.html`. (26th January 2011).

[RIP, 2011] (2011). Reference Input Parameter Library (RIPL-3). `http://www-nds.iaea.org/RIPL-3/`. (26th January 2011).

[W1, 2011] (2011). Website of the Budapest Institute of Isotopes. `http://www.iki.kfki.hu/nuclear/instruments/pgaa_en.shtml`. (12th January 2011).

[W2, 2011] (2011). Website of the Budapest Institute of Isotopes. `http://www.iki.kfki.hu/nuclear/research/chopper_en.shtml`. (12th January 2011).

[Abderrahim et al., 2001] Abderrahim, H. et al. (2001). MYRRHA: A multipurpose accelerator driven system for research & development. *Nuclear Instruments and Methods in Physics Research Section A: Accelerators, Spectrometers, Detectors and Associated Equipment*, 463:487–494.

[Ajzenberg-Selove, 1990] Ajzenberg-Selove, F. (1990). Energy levels of light nuclei A=11-12. *Nuclear Physics A*, 506:1–158.

[Andrejtscheff, 1994] Andrejtscheff, W. (1994). Evidence for strong ground-state shape asymmetry in even germanium and selenium isotopes. *Physics Letters B*, 329:1–4.

[Axel, 1962] Axel, P. (1962). Electric Dipole Ground-State Transition Width Strength Function and 7-MeV Photon Interactions. *Physical Review*, 126:671–683.

[Axel, 1968] Axel, P. (1968). Simply nuclear excitations distributed among closely spaced levels. In *Proceedings of the International Symposium on Nuclear Structure*.

[Axel et al., 1970] Axel, P. et al. (1970). Intermediate Structure in the Photon Interaction Cross Section of Sn and Zr. *Physical Review C*, 2:689–711.

[Bartholomew et al., 1973] Bartholomew, G. et al. (1973). Gamma ray strength functions. *Advances in Nuclear Physics*, 7.

[Becvar, 1998] Becvar, F. (1998). Simulation of cascades in complex nuclei with emphasis on assessment of uncertainties of cascade-related quantities. *Nuclear Instruments and Methods in Physics Research Section A: Accelerators, Spectrometers, Detectors and Associated Equipment*, 417.

[Becvar et al., 2007] Becvar, F. et al. (2007). The two-step gamma casacade method as a tool for studying photon strength functions of intermediate-weight and heavy nuclei. *Nuclear Instruments and Methods in Physics Research Section B: Beam Interactions with Materials and Atoms*, 261.

[Berman et al., 1987] Berman, B. et al. (1987). Absolute photoneutron cross sections for Zr, I, Pr, Au, and Pb. *Physical Review C*, 36:1286–1292.

[Brink, 1955] Brink, D. (1955). *Some reactions with neutrons.* PhD thesis, University of Oxford.

[Carlos et al., 1976] Carlos, P. et al. (1976). A study of the photoneutron contribution to the giant dipole resonance of nuclei in the $64 \leq A \leq 86$ mass region. *Nuclear Physics A*, 258:365–387.

[Egidy and Bucurescu, 2009] Egidy, T. and Bucurescu, D. (2009). Experimental energy-dependent nuclear spin distribution. *Physical Review C*, 80:054310.

[Endres et al., 2010] Endres, J. et al. (2010). Isospin Character of the Pygmy Dipole Resonance in ^{124}Sn. *Physical Review Letters*, 105:212503.

[Ericson, 1960] Ericson, T. (1960). The Statistical Model and Nuclear Level Densities. *Advances in Nuclear Physics*, 9:425–511.

[Farhan and Singh, 2009] Farhan, A. and Singh, B. (2009). Nuclear Data Sheets for $A = 78$. *Nuclear Data Sheets*, 110:1917 – 2080.

[Gilbert and Cameron, 1965] Gilbert, A. and Cameron, A. (1965). A composite nuclear-level density formula with shell corrections. *Canadian Journal of Physics*, 43:1446–1496.

[Goldhaber and Teller, 1948] Goldhaber, M. and Teller, E. (1948). On Nuclear Dipole Vibrations. *Phyiscal Review*, 74:1046 – 1049.

[Goryachev and Zalesnyi, 1978] Goryachev, A. and Zalesnyi, G. (1978). The Giant Dipole Resonance and the Shape of the Transition Nuclei Ir and Pt. *Yadernaya Fizika*, 27:1479.

[Grossjean and Feldmeier, 1985] Grossjean, M. and Feldmeier, H. (1985). Level Density of a Fermi Gas with Pairing Interactions. *Nuclear Physics A*, 444:113–132.

[Guhr et al., 1998] Guhr, T. et al. (1998). Random-matrix theories in quantum physics:common concepts. *Physics Reports*, 299:189–425.

[Guttormsen et al., 2003] Guttormsen, M. et al. (2003). Free energy and criticality in the nucleon pair breaking process. *Physical Review C*, 68:034311.

[Heyde et al., 2010] Heyde, K. et al. (2010). Magnetic dipole excitations in nuclei: Elementary modes of nucleonic motion. *Review of Modern Physics*, 82:2365–2419.

[Huizenga and Moretto, 1972] Huizenga, J. and Moretto, L. (1972). Nuclear Level Densities. *Annual Review of Nuclear Science*, 22:427–464.

[Ignatyuk et al., 1975] Ignatyuk, A. et al. (1975). Statistical Properties of Excited Atomic Nuclei. *Soviet Journal of Nuclear Physics*, 21:255.

[Junghans et al., 2008] Junghans, A. et al. (2008). Photon data shed new light upon the GDR spreading width in heavy nuclei. *Physics Letters B*, 670.

[Kneissl et al., 1996] Kneissl, U. et al. (1996). Investigation of Nuclear Structure by Resonance Fluorescence Scattering. *Progress in Particle and Nuclear Physics*, 37:349–433.

[Koehler et al., 2010] Koehler, P. et al. (2010). Anomalous Fluctuations of s-Wave Reduced Neutron Widths of ^{192,194}Pt Resonances. *Physical Review Letters*, 105:072502.

[Koning et al., 2008] Koning, A., Hilaire, S., and Goriely, S. (2008). Global and local level density models. *Nuclear Physics A*, 810:13–76.

[Kopecky et al., 1993] Kopecky, J. et al. (1993). Radiative strength in the compound nucleus ^{157}Gd. *Physical Review C*, 47:312–322.

[Lynn, 1968] Lynn, J. (1968). *The Theory of Neutron Resonance Reactions*. Clarendon Press.

[Massarczyk, 2011] Massarczyk, R. (2011). Bestimmung der elektromagnetischen Dipolstärkeverteilung in mittelschweren Atomkernen mittels Kernresonanzfluoreszenz. Master's thesis, TU Dresden.

[Mughabghab, 2006] Mughabghab, S. (2006). *Atlas of neutron resonances*, volume 5. Elsevier.

[Porter and Thomas, 1956] Porter, C. and Thomas, R. (1956). Fluctuations of Nuclear Reaction Widths. *Physical Review*, 104:483–491.

[Raman et al., 2001] Raman, S. et al. (2001). Transition probability from the ground to the first-excited 2+ state of even–even nuclides. *Atomic Data and Nuclear Data Tables*, 78:1–128.

[Rusev, 2007] Rusev, G. (2007). *Dipole-strength distribution below the giant dipole resonance in ^{92}Mo, ^{98}Mo and ^{100}Mo*. PhD thesis, TU Dresden.

[Rusev et al., 2009] Rusev, G. et al. (2009). Multipole mixing ratios of transitions in ^{11}B. *Physical Review C*, 79:047601.

[Schmidt and Jurado, 2011] Schmidt, K.-H. and Jurado, B. (2011). Thermodynamics of nuclei in thermal contact. *Physical Review C*, 83:014607.

[Schwengner et al., 2005] Schwengner, R. et al. (2005). The photon-scattering facility at the superconducting electron accelerator ELBE. *Nuclear Instruments and Methods in Physics Research Section A: Accelerators, Spectrometers, Detectors and Associated Equipment*, 555:211–219.

[Schwengner et al., 2007] Schwengner, R. et al. (2007). Dipole response of ^{88}Sr up to the neutron-separation energy. *Physical Review C*, 76:034321.

[Seltzer and Berger, 1986] Seltzer, S. and Berger, M. (1986). Bremsstrahlungs energy spectra from electrons with kinetic energy 1keV-10GeV incident on screened nuclei and orbital electrons of neutral atoms with Z=1-100. *Atomic Data and Nuclear Data Tables*, 35:345–418.

[Steinwedel et al., 1950] Steinwedel, H. et al. (1950). Nuclear Dipole Vibrations. *Physical Review*, 79:1019.

[Szentmiklósi et al., 2010] Szentmiklósi, L. et al. (2010). Upgrade of the prompt gamma activation analysis and the neutron-induced prompt gamma spectroscopy facilities at the Budapest research reactor. *Journal of Radioanalytical and Nuclear Chemistry*, 286:501–505.

[Tonchev et al., 2005] Tonchev, A. et al. (2005). The high intensity γ-ray source (HIγS) and recent results. *Nuclear Instruments and Methods in Physics Research Section B: Beam Interactions with Materials and Atoms*, 241:170–175.

[Voinov et al., 2009] Voinov, A. et al. (2009). Nuclear excitations at constant temperature. *Physical Review C*, 79:031301.

[Weidenmüller, 2010] Weidenmüller, H. (2010). Distribution of Partial Neutron Widths for Nuclei Close to a Maximum of the Neutron Strength Function. *Physical Review Letters*, 105:232501.

[Xiaolong, 2007] Xiaolong, H. (2007). Nuclear Data Sheets for A = 196. *Nuclear Data Sheets*, 108:1093–1286.